A Unified Convection Scheme (UNICON). Part II: Simulation

SUNGSU PARK

Climate and Global Dynamics Division, National Center for Atmospheric Research, Boulder, Colorado

ABSTRACT

A unified convection scheme (UNICON) is implemented into the Community Atmosphere Model, version 5 (CAM5), and tested in single-column and global simulations forced by observed sea surface temperature. Compared to CAM5, UNICON substantially improves the single-column simulations of stratocumulus-to-cumulus transition and shallow and deep convection cases. The global performance of UNICON is similar to CAM5 with a relative spatiotemporal root-mean-square error (RMSE) of 0.777 (0.755 in CAM5) against the earlier version of the model (CCSM3.5). The notable improvements in the UNICON-simulated climatologies over CAM5 are seasonal precipitation patterns (i.e., monsoon) over the western Pacific and South Asia, reduced biases of cloud radiative forcing in the tropical deep convection regions, aerosol optical depth in the tropical and subtropical regions, and cumulus fraction and in-cumulus condensate. One notable degradation is that UNICON simulates warmer near-surface air temperature over the United States during summer.

In addition to the climatology, UNICON significantly improves the simulation of the diurnal cycle of precipitation and the Madden–Julian oscillation (MJO). The surface precipitation simulated by UNICON is a maximum in the late afternoon (early afternoon in CAM5) over the summer continents and in the early morning (predawn in CAM5) over the ocean with a fairly realistic amplitude of the diurnal cycle. Sensitivity simulations indicate that the key for successful MJO simulation in UNICON is a seamless parameterization of the updraft plume dilution rate as convection evolves from shallow to deep convection. The mesoscale perturbation of the vertical velocity and the thermodynamic scalars of convective updrafts is an additional requirement for simulating the observed diurnal cycle of precipitation.

1. Introduction

In the accompanying paper (Park 2014, hereafter Part I), the author developed a unified convection scheme (UNICON). UNICON is a process-based, dynamic plume model that does not rely on any equilibrium assumptions such as convective available potential energy (CAPE) or convective inhibition (CIN) closures. It consists of diagnostic multiple convective updrafts rising from the surface, diagnostic multiple convective downdrafts generated from convective updrafts in any layers below the cumulus top, and prognostic subgrid cold pool and associated mesoscale organized flow within the planetary boundary layer (PBL). The cold pool and mesoscale organized flow are forced by convective downdrafts and evaporation of convective precipitation, while damped by surface flux and

entrainment at the PBL top and feedbacks to the convective updrafts.

UNICON simulates all dry–moist, forced–free, and shallow–deep convection within a single framework in a seamless, consistent, and unified way. There is no difference in the treatment of dry and moist convection except for the evaporative enhancement of the mixing rate in a saturated cumulus updraft. Explicit dynamic treatment of the convective downdrafts allows UNICON to simulate both the forced and free convection in a consistent way, without a separate penetrative entrainment closure at the cumulus top. Because of the prognostic treatment of subgrid cold pool and mesoscale organized flow, and its feedback on convective updrafts, UNICON carries convective plume memory across the model time steps and simulates both the shallow and deep convection in a seamless and unified way. Designed to simulate relative (i.e., with respect to the grid-mean flow) subgrid vertical transport by nonlocal asymmetric turbulent eddies, not the observed convection, UNICON in principle can be used for any size of general circulation model (GCM) horizontal grid as a scale-adaptive scheme, when implemented

Corresponding author address: Sungsu Park, Climate and Global Dynamics Division, National Center for Atmospheric Research, P.O. Box 3000, Boulder, CO 80307.
E-mail: sungsup@ucar.edu

with an exclusive subgrid vertical transport scheme by local symmetric turbulent eddies (e.g., conventional PBL scheme without a nonlocal transport term).

If a new parameterization scheme has correct physics and numerics with appropriate parameter values, it should be able to simulate all the relevant phenomena when implemented into a good compatible base framework. The main goal of this paper is to check whether UNICON has the capability to simulate most of the convection-related phenomena [e.g., monsoon, cloud radiative forcing, stratocumulus-to-cumulus transition, diurnal cycle of precipitation, and MJO (Madden and Julian 1971)] when implemented into the National Center for Atmospheric Research (NCAR) CAM5 (Park et al. 2014), identify the sources of the biases against observations, and find a path forward for future improvement.

The structure of this paper is as follows. Section 2 provides a brief description of the configuration of simulations and model parameters. Section 3 shows various single-column simulations. Section 4 provides a discussion on the UNICON-simulated global climatologies compared with CAM5 and observations. Sections 5 and 6 show the simulations of the diurnal cycle of precipitation at the surface and the MJO, respectively—both of which have been long-standing issues in the modeling community. Section 7 provides various sensitivity simulations to the model parameters, which will provide insights into the key physical mechanisms controlling the diurnal cycle of precipitation and the MJO, and into the sources of the biases in the UNICON simulations. A summary and conclusion will be given in section 8.

2. Simulation configuration and parameter values

We use CAM5 as a base framework to test UNICON, which replaces the CAM5 shallow and deep convection schemes. From now on, CAM5 with UNICON will be referred to as UNICON, while CAM5 with the default shallow and deep convection schemes will be referred to as CAM5. The notation of the math symbols and the equation numbers used in this paper will follow Part I.

Differences exist in the operating regimes between UNICON and CAM5 shallow and deep convection schemes. The CAM5 shallow convection scheme (Park and Bretherton 2009) launches a single ensemble-mean convective updraft from the PBL top if the convective updraft fractional area at the PBL top diagnosed by turbulent kinetic energy (TKE) and CIN is larger than 1.1×10^{-5}. Here, CIN is computed from the PBL top to the level of free convection (LFC) for an undiluted plume. Thus, when the PBL is very dry or capped by a strong inversion, CIN becomes large, so that the CAM5 shallow convection scheme is inactive. The CAM5 deep convection scheme (Zhang and McFarlane 1995; Neale et al. 2008; Richter and Rasch 2008) launches a single ensemble-mean convective updraft from the level of maximum moist static energy z_* if the diluted CAPE computed from z_* to the level of neutral buoyancy (LNB) is larger than $70 \, \mathrm{J \, kg^{-1}}$, assuming a constant entrainment rate of $1 \times 10^{-3} \, \mathrm{m^{-1}}$. By construction, the CAPE constraint inhibits convective activity from stable to shallow convection regimes where CAPE $< 70 \, \mathrm{J \, kg^{-1}}$ because the cumulus top is low. Both the CAM5 shallow and deep convection schemes have limitations in simulating dry and forced convection. On the other hand, similar to the CAM5 moist turbulence scheme (Bretherton and Park 2009), UNICON operates in all regimes without any on-and-off switches. Even in the stable PBL, a set of multiple updraft plumes rises from the surface, but strong environmental stratification inhibits further rising of the negatively buoyant convective updrafts.

To ensure that cloud microphysics operates on consistent stratus droplet mass and number concentration, we performed aerosol activation at the beginning of stratiform microphysics rather than in the middle, both in CAM5 and UNICON simulations. We also adjusted three tuning parameters in UNICON simulation to obtain reasonable global annual-mean aerosol optical depth (AOD) and radiation balance at the top of the atmosphere: the aerosol scavenging factor was increased to 1 for the wet removal of cloudborne aerosols within cumulus (from 0.4 in CAM5) and interstitial aerosols within cumulus and stratus (from 0.1 in CAM5); the evaporative enhancement factor a_{21} was increased to 40 in the moist turbulence scheme (from 30 in CAM5); and the critical relative humidity of low-level cloud fraction ($\mathrm{RH_{cri,low}}$) was decreased to 0.85 in the cloud macrophysics scheme (from 0.8875 in CAM5).

In this paper, we made two simplifying approximations to the cold pool formulation [Eqs. (61)–(64)]: except for those sinking exclusively down into the cold pool, all the other convective downdrafts at the PBL top fall uniformly over the entire grid (i.e., $\check{M}^j_{U,h} = 0$) and the conservative scalars of the convective updrafts at the PBL top are roughly similar to the mean bulk properties of the non–cold pool area (i.e., $\hat{\phi}^j_h \approx \phi_U$). Two test simulations—one with $\check{M}^j_{G,h} = 0$ instead of $\check{M}^j_{U,h} = 0$, and the other without the second approximation (with additional tuning of several model parameters within plausible ranges)—however, produced similar results to the default simulation (not shown), so that the results and the conclusion drawn in this paper are valid regardless of these approximations.

Table 1 shows the values of the UNICON model parameters, which are grouped into system, dynamics of individual convective updrafts and downdrafts, cold

pool and mesoscale organized flow within the PBL, and cloud macrophysics and microphysics. Parameter values are chosen based on observational studies or laboratory experiments (e.g., $\hat{w}_{max}$, a_1, C_d, R_o), large-eddy simulation (LES) analysis (e.g., k_w, c_m), a default CAM5 setting (e.g., b, r_c, $\hat{q}_{c,crit}$, c_{at}, $k_{e,R}$, $k_{e,S}$, $\hat{r}_l$, $\hat{r}_i$), the constraint required to impose physical consistency (e.g., $\hat{A}_{max}$, c, λ), or extensive trial-and-error simulations. The model parameter values listed in Table 1 are consistently used both for single-column and global simulations. It should be noted that except for one sensitivity experiment of global simulations (i.e., S.1 in Table 2), all the simulations used in this paper use a single updraft plume (i.e., $\hat{n}_s = 1$ in Table 1). Owing partly to the implementation of various new physics, observational studies directly relevant to constraining the UNICON model parameters are highly limited. For example, we have no measurements on the mixing rate between the cold pool (or convective downdraft) and the ambient air, although some studies provide information on the radius of saturated updraft plumes (Plank 1969; Neggers et al. 2003). Further studies are necessary to constrain the model parameters.

The conventional approach to test a new parameterization is to use a single-column configuration that has model physics identical to the global configuration but with specified grid-mean advective forcing and surface fluxes (or surface temperature). Because feedback of the parameterized physical processes on grid-mean advective forcing is shut off, single-column simulation is a powerful tool for evaluating the realism of the responses of parameterized subgrid physical processes to one-way grid-mean forcing in an isolated way, if comparable observations or LESs exist. We evaluate UNICON with various single-column test cases in section 3.

Two types of global simulations—an Atmospheric Model Intercomparison Project (AMIP) simulation forced by the observed interannual sea surface temperature (SST) and sea ice fraction with an annual cycle for 27 years from January 1979 to December 2005 and a standalone simulation forced by the observed climatological SST and sea ice fraction with an annual cycle for 10 years—are performed at a horizontal resolution of 1.9° latitude × 2.5° longitude for both CAM5 and UNICON. (Except for the sensitivity simulations in Table 2 and Fig. 23, we use the AMIP simulations for our analysis.) The detailed configuration of the AMIP and stand-alone simulations are described in Park et al. (2014).

3. Single-column simulations

Single-column simulations are performed for five different cases spanning a wide range of regimes (dry convective PBL, stratocumulus-topped PBL over the ocean, stratocumulus-to-cumulus transition over the ocean, shallow convection over the ocean, deep convection over land) in two different vertical and temporal resolutions (the operational L30 with $\Delta t = 1200\,s$ and the experimental L80 with $\Delta t = 300\,s$, where L denotes the number of vertical layers and Δt is the model integration time step). To compute the grid-mean vertical advection from the specified grid-mean subsidence rate, we use a downstream Eulerian difference for temperature and horizontal wind and a semi-Lagrangian method for water substances and the other tracers. The simulations are compared with observation for the deep convection case and with the LES for the other cases. The LES used in this paper are those used in Park and Bretherton (2009) and Bretherton and Park (2009). The LES for the stratocumulus-to-cumulus transition case was generated by Dr. Peter Blossey at the University of Washington using the System for Atmospheric Modeling (SAM; Khairoutdinov and Randall 2003). As will be shown, UNICON produces similar or substantially improved results than CAM5. The skill score defined as the ratio of the RMSE of the UNICON-simulated time series of $\tilde{\theta}_c(z)$ and $\tilde{q}_t(z)$ against the LES (or the observation) to the RMSE of CAM5 are 0.95, 1.09, 0.36, 0.63 and 0.54, respectively, from the dry convective PBL to the deep convection cases. Here, θ_c and q_t are condensate potential temperature and total specific humidity, respectively, with the tilde denoting an environmental mean. One of the main goals of this section is to provide the reader with a direct view of how UNICON is operating at the process level, which is difficult to portray in a global simulation that contains complex interaction and feedback among various physics and dynamic processes.

a. Dry convective PBL

This is an idealized dry convection case constructed by Park and Bretherton (2009). It is forced by a constant sensible heat flux, SHF = $300\,W\,m^{-2}$ at surface pressure $P_s = 1000\,hPa$ starting from a stable initial profile of grid-mean potential temperature $\bar{\theta}(z)$ that linearly increases with height at the rate of $\Gamma_{\bar{\theta}} = 3\,K\,km^{-1}$ from 288 K at the surface. Simulation is run for 8 h by turning off the radiation, grid-mean subsidence, and horizontal advection. No moisture exists throughout the simulation.

Figure 1 shows various aspects of the UNICON simulation compared with the CAM5 and the LES (Figs. 1a–d) with the detailed diagnostics of the UNICON simulation (Figs. 1e–l) at the L30 resolution. Figure 1a shows the time evolution of the PBL-top heights z_h diagnosed by the PBL scheme in CAM5 and UNICON simulations and the level of minimum buoyancy flux z_h

TABLE 1. Model parameters used in UNICON with equation numbers from Part I.

Parameter	Physical meaning	Equation No.	Default value	Possible range	Unit
System					
$\hat{n}_s$	Number of updraft segments at the surface	—	1	$1 \le \hat{n}_s$	—
$\hat{A}_{max}$	Maximum updraft fractional area allowed	47	0.1	$0 < \hat{A}_{max} \ll 1$	—
$\hat{w}_{max}$	Maximum updraft vertical velocity allowed	47	20	$10 < \hat{w}_{max}$	$m\,s^{-1}$
$\breve{w}_{min}$	Minimum downdraft vertical velocity allowed	51	0.1	$0 < \breve{w}_{min}$	$m\,s^{-1}$
Updraft dynamics					
k_w	Anisotropic factor of nonorganized turbulence at the surface	21	0.35	$0 < k_w < 0.82$	—
R_a	e-folding radius at which $a(R_a) = 0.58$	29	200	$0 \le R_a$	m
b	Entrainment drag coefficient	27, 28	2	$1 \le b$	—
c	Detrainment thrust coefficient	27, 28	0	$0 \le c \le 1$	—
a_1	Dry mixing coefficient	31	0.2	$0.1 < a_1 < 0.3$	—
a_2	Moist mixing coefficient with $\hat{q}_l + \hat{q}_i$ in Eq. (32) in units of $g\,kg^{-1}$	31	1	$0 \le a_2$	—
p	A power of the mass PDF for updraft buoyancy sorting	35	2	$0 < p$	—
r_c	Critical distance $l_c(t) = r_c \hat{z}_{top}(t - \Delta t)$	B2	0.15	$0 < r_c < 1$	—
c_m	Adjustment factor of the plume u and v to the environmental u and v	41	0.9	$0 < c_m < 1$	—
Downdraft dynamics					
$\breve{\epsilon}, \breve{\delta}$	Entrainment and detrainment rates	11	0	$0 < \breve{\epsilon}, \breve{\delta}$	Pa^{-1}
a	Buoyancy coefficient	29	0.67	$0.33 < a < 1$	—
λ	A parameter used for downdraft buoyancy sorting	42	0.5	$0 \le \lambda \le 1$	—
Cold pool and mesoscale organized flow within the PBL					
ϵ_*, δ_*	Entrainment and detrainment rates between the cold pool and the ambient air ($\epsilon_c = \epsilon_* a_D$, $\delta_c = \delta_* a_D$)	61–64	3.47×10^{-5}	$0 \le \epsilon_*, \delta_*$	s^{-1}
C_d	Surface exchange (or drag) coefficient	63, 64	1.5×10^{-3}	$1 \times 10^{-3} \le C_d \le 1.5 \times 10^{-3}$	—
$\delta\theta_{v,D}^{cri}$	Minimum critical buoyancy of a cold pool	70, 71	-0.05	$\delta\theta_{v,D}^{cri} < 0$	K
c_Ω	Fractional area of the upflow branch of subgrid mesoscale organized flow is $a_{cz} = c_\Omega \hat{A}_s(\Omega)$	73, 74	3	$1 \le c_\Omega \le \hat{A}_s^{-1}\|_{\Omega=0}$	—
k_*	Fraction of the cold pool APE converted into the mesoscale KE within the PBL	74	0.05	$0 < k_* < 1$	—
Cloud macrophysics					
$\hat{A}_s\|_{\Omega=0}$	Updraft fractional area at the surface at $\Omega = 0$	75	0.04(ocn)/ 0.03(lnd)	$0 \le \hat{A}_s\|_{\Omega=0} \le \hat{A}_{max}$	—
$R_o\|_{\Omega=0}$	Intercept radius of updraft plume at the surface at $\Omega = 0$	76	100	$R_o\|_{\Omega=0} \le R_o\|_{\Omega=1}$	m
$R_o\|_{\Omega=1}$	Intercept radius of updraft plume at the surface at $\Omega = 1$	76	2000(ocn)/ 4000(lnd)	$R_o\|_{\Omega=1} < \sqrt{(G\hat{A}_{max})/\pi}$	m
$\sigma_R\|_{\Omega=0}$	Standard deviation of updraft plume radius at the surface at $\Omega = 0$	77	25	$0 \le \sigma_R\|_{\Omega=0}$	m
$\sigma_R\|_{\Omega=1}$	Standard deviation of updraft plume radius at the surface at $\Omega = 1$	77	25	$\sigma_R\|_{\Omega=0} \le \sigma_R\|_{\Omega=1}$	m
γ	The order of polynomial $R_o(\Omega)$ and $\sigma_R(\Omega)$	76, 77	1	$0 < \gamma$	—
β	A overlapping parameter between $\ddot{a}$ (or $\breve{a}$) and a_U	68, 69	1	$0 \le \beta \le 1$	—

TABLE 1. (*Continued*)

Parameter	Physical meaning	Equation No.	Default value	Possible range	Unit
Cloud Microphysics					
$\hat{q}_{c,crit}$	Maximum in-cumulus condensate that updraft plume can hold	38	6×10^{-4}	$5 \times 10^{-4} < \hat{q}_{c,crit} < 1 \times 10^{-3}$	$kg\,kg^{-1}$
c_{at}	Autoconversion efficiency of cumulus condensate	38	5×10^{-4}	$5 \times 10^{-4} < c_{at} < 5 \times 10^{-3}$	Pa^{-1}
$k_{e,R}, k_{e,S}$	Evaporation efficiency of convective rain and snow	51, 81	2×10^{-5}	$5 \times 10^{-6} < k_{e,R}, k_{e,S} < 2 \times 10^{-5}$	$m\,(kg\,s)^{-0.5}$
η	Maximum fraction of convective precipitation that can be evaporated within an individual convective downdraft	51	0.15	$0 \leq \eta \leq 1$	—
c_ξ	Wet scavenging coefficient of tracer within the updraft plume	39	0.3	$0 \leq c_\xi \leq 1$	—
$\hat{r}_l$	Effective radius of cumulus liquid droplets	40	10	$5 < \hat{r}_l < 20$	μm
$\hat{r}_i$	Effective radius of cumulus ice crystals	40	50	$25 < \hat{r}_i < 70$	μm

from the LES. Both CAM5 and UNICON well reproduce the LES-simulated, gradual deepening of z_h. Since z_h is defined as the top model interface of the surface-based convective regime in the CAM5 PBL scheme (Bretherton and Park 2009), the simulated z_h increases in a discrete way between the model interfaces. UNICON tends to simulate faster PBL deepening than CAM5. The top height of the convective updraft simulated by UNICON at which the updraft vertical velocity is zero ($\hat{z}_{TOP}$ in Fig. 1a) is located at slightly above z_h.

The vertical profiles of θ, buoyancy flux [$F_B \equiv (g/\overline{\theta})\overline{w'\theta'}$], and turbulent kinetic energy [TKE $\equiv (1/2)(\overline{u'^2} + \overline{v'^2} + \overline{w'^2})$] at the instantaneous time step indicated by the red vertical line in Fig. 1a are shown in Figs. 1b–d, respectively. The local and nonlocal fluxes in the UNICON simulation in Fig. 1c are the fluxes simulated by the CAM5 PBL scheme and UNICON, respectively. Since the CAM5 PBL scheme is a downgradient diffusion model without a nonlocal transport term (Bretherton and Park 2009), $\tilde{\theta}(z)$ simulated by CAM5 shows an unstable stratification in the entire PBL, except near the PBL top, in order to match the simulated $F_B(z)$ that decreases almost linearly with height to $F_B(z_h) \approx -0.2F_B(0)$. Note that because this is a dry convection case, none of the shallow and deep convection schemes are active in the CAM5 simulation. With the additional nonlocal buoyancy flux that increases up to $z = 1135\,m$ but decreases above, however, UNICON simulates colder (warmer) $\tilde{\theta}(z)$ than CAM5 in the lower (upper) PBL (also see Fig. 1l), correcting the CAM5's bias of the unstable stratification in the upper PBL. Since the entrainment rate in the CAM5 PBL scheme is inversely proportional to the inversion strength at the PBL top (Bretherton and Park 2009), warming in the upper PBL

induces faster deepening of z_h in the UNICON simulation than in CAM5, as shown in Fig. 1a. It is interesting to note that the sum of UNICON-simulated local and nonlocal buoyancy fluxes is almost identical to the CAM5-simulated buoyancy flux that is solely from the local transport. Similar partitioning can be seen in the TKE profile (Fig. 1d): the local TKE simulated by the PBL scheme in the UNICON simulation is slightly smaller than CAM5, but if the kinetic energy of the convective updraft plume is added [nonlocal TKE = $(1/2)\hat{a}\hat{w}^2$], the resulting total TKE becomes quite similar to that of CAM5.

The updraft buoyancy reaches to the maximum of $0.64\,K$ at $z = 128\,m$ and decreases afterward with a sign reversal above the LNB that is located at z_h for this case [Figs. 1e,k and note that $\tilde{\theta}$ in Fig. 1k is $\tilde{\theta}^{bot}(k)$ not $\tilde{\theta}^{top}(k-1)$ as shown in Fig. 4 of Part I]. Since the updraft plume is dry, all the mixtures between the convective updraft and the environment below the LNB are positively buoyant and are entrained into the convective updraft (Fig. 1j where $\chi_c = \chi_{d,min} = \chi_{d,max} = 1$ and $\hat{\delta} = 0$), while the mixtures at the LNB are either detrained ($\chi_{d,max} \leq \chi \leq 1$) or converted into the mixing downdraft ($\chi_{d,min} = 0 \leq \chi \leq \chi_{d,max}$). Figure 1e also shows the mass flux–weighted θ of the convective downdraft (blue; $\breve{\theta}$) and the mass flux–weighted θ of the mixing environmental air [green; θ_r from Eq. (60) and corresponding M_r from Eq. (59) is shown in Fig. 1f]. In this dry convection case, θ_r is not used in computing the updraft plume dynamics, since the mesoscale organized flow does not exist [$\Omega = 0$; Eq. (72)]. However, if the mesoscale organized flow is developed within the PBL (e.g., deep convection case in section 3e), $\theta_r(t)$ will be used as part of the mixing environmental scalar for the convective updraft above the PBL at the next time step [Eq. (78)].
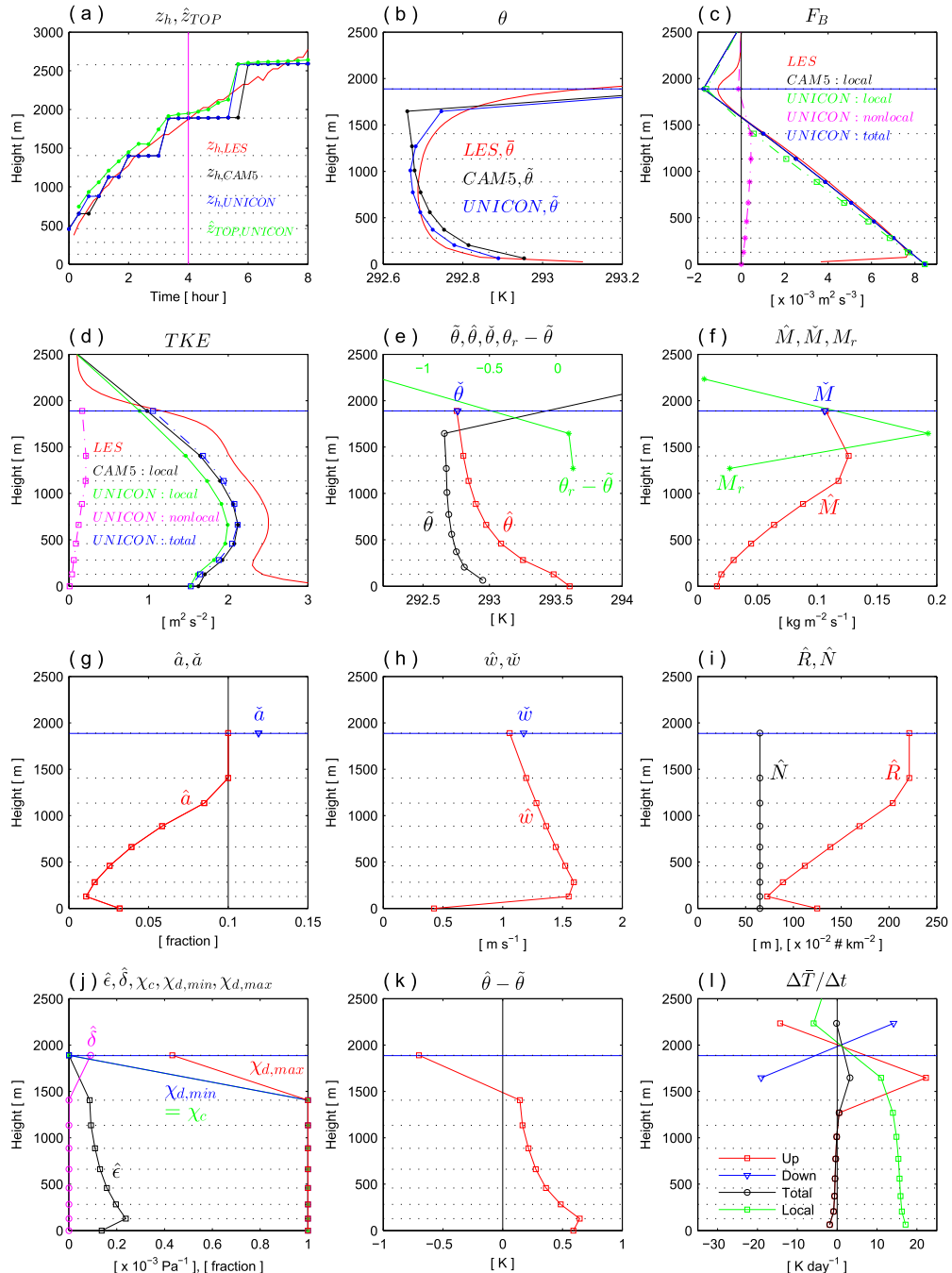
FIG. 1. A single-column simulation of an idealized dry convection case. (a) Time series of the PBL-top height z_h and the updraft-top height $\hat{z}_{TOP}$ (where $\hat{w} = 0$). (b)–(l) The vertical profiles at the instantaneous time step of $t = 4$ h for potential temperature θ; buoyancy flux $F_B = (g/\overline{\theta})\overline{w'\theta'}$; turbulent kinetic energy (TKE); mass flux M; fractional area a; vertical velocity w; updraft plume radius $\hat{R}$ and updraft number density $\hat{N}$; fractional entrainment and detrainment rates of the updraft ($\hat{\epsilon}, \hat{\delta}$) [see Eqs. (33) and (34)], critical mixing fraction χ_c [Eq. (B2)], and $\chi_{d,\min}$ and $\chi_{d,\max}$ (see Fig. 4 in Part I); and grid-mean temperature tendencies by convective updraft [Up: the sum of the first and third terms on the rhs of Eq. (17)], convective downdraft [Down: the sum of the second and fourth terms on the rhs of Eq. (17)], total convective processes (Total = Up + Down), and the PBL scheme (Local). For any variable ψ, we use $\hat{\psi}, \check{\psi}, \psi_r, \tilde{\psi},$ and $\overline{\psi}$ to denote the updraft, downdraft, detrained air, environment, and the grid mean, respectively. In Figs. 1–6, the scale of $\psi_r - \tilde{\psi}_r$ from the UNICON simulation is shown on the top horizontal axis. The horizontal blue solid and black dotted lines are z_h from the UNICON simulation and the model interfaces, respectively. In (c),(d), local and nonlocal denote those from the PBL and convection schemes, respectively, with nonlocal TKE = $(1/2)\hat{a}\hat{w}^2$.

The updraft fractional area $\hat{a}$ decreases in the lowest model layer, increases afterward up to $z = 1420$ m, and then remains a constant further above with a specified upper maximum value of $\hat{A}_{\max} = 0.1$ (Fig. 1g), indicating that the area-constrained downdraft is generated [Eq. (47)]. The vertical gradient of the updraft vertical velocity $\hat{w}$ changes its sign at the top interface of the second lowest model layer (Fig. 1h), from which the magnitude of entrainment drag becomes larger than the positive buoyancy forcing [Eq. (27)]. The updraft mass flux, $\hat{M} = \rho \hat{a} \hat{w}$, increases with height up to $z = 1420$ m but decreases afterward (Fig. 1f). The vertical profile of the updraft plume radius $\hat{R} = \sqrt{\hat{a}/(\pi\hat{N})}$ follows the shape of $\hat{a}$, since only one set of convective updraft plumes exists throughout the entire PBL with a height-independent number density, $\hat{N} = 0.65$ km^{-2} (Fig. 1i). Note that the mixing rate of convective updraft plume [$\hat{\epsilon}_o(z) = \hat{\epsilon}(z)$ below z_h while $\hat{\epsilon}_o(z) = \hat{\delta}(z)$ at z_h, Fig. 1j] is inversely proportional to $\hat{R}(z)$ [Eq. (31)]. In this dry convection case, a convective downdraft exists only at the base interface of the updraft top layer or at the LNB (Figs. 1e–h), which is a sum of the mixing and top downdrafts.

Overall, local symmetric turbulent eddies simulated by the CAM5 PBL scheme cool the layer just above z_h but warm the entire PBL with a stronger (weaker) warming in the lower (upper) PBL, and so the PBL is destabilized. On the other hand, nonlocal asymmetric turbulent eddies simulated by UNICON cool the lower PBL below $z = 1135$ m but warm the upper PBL and stabilize the PBL. In the two layers just below and above z_h, individual convective updrafts and downdrafts induce strong warming and cooling tendencies, but compensation occurs between the two, resulting in much weaker net heating tendency.

b. Stratocumulus-topped PBL

This is the case constructed from the field experiment of nocturnal stratocumulus-topped PBL over the subtropical eastern Pacific Ocean: the Second Dynamics and Chemistry of Marine Stratocumulus Experiment (DYCOMS2; Stevens et al. 2005). It is forced by constant latent heat flux, LHF $= 115$ W m^{-2} and SHF $= 15$ W m^{-2} at SST $= 292.5$ K and $P_s = 1017.8$ hPa starting from the initial profile consisting of the well-mixed layer up to a height of 800 m capped by a strong inversion and vertically uniform geostrophic horizontal wind. Simulation is run for 5 h with a longwave (LW) radiative heating profile that is specified as a function of grid-mean liquid water content (LWC), a time-invariant grid-mean subsidence rate that increases linearly with height up to 800 hPa, and the horizontal advection of heat and moisture. Stratiform precipitation and sedimentation are turned off. This case differs from the previous dry convection case in that the main TKE sources are the buoyancy production at the PBL top driven by the cloud-top LW radiative cooling and the condensation heating as well as the buoyancy flux at the surface.

Figure 2 shows the vertical profiles of several thermodynamic variables averaged over the last hour of the simulation. Similar to LES, both CAM5 and UNICON simulate nearly well-mixed $\tilde{\theta}_c$, $\tilde{q}_t$, $\tilde{U}$, and $\tilde{V}$ within the PBL (Figs. 2a–c), with a maximum LWC and stratus fraction in the layer just below z_h (Fig. 2d). Since the strength of the inversion layer (i.e., CIN) relative to the TKE within the PBL is substantially strong, the shallow convection scheme in the CAM5 simulation is deactivated (Park and Bretherton 2009; Park et al. 2014), and all subgrid vertical transport is from the local moist PBL scheme, as shown in Fig. 2e. On the other hand, UNICON performs additional subgrid nonlocal vertical transport and helps to sustain stratocumulus deck by transporting moisture from the lower PBL to the upper PBL (Figs. 2e,j) and also by detraining convective condensate ($q_{l,r} - \tilde{q}_l > 0$ and $M_r > 0$ in Figs. 2d and 2f). Similar to the previous dry convection case, the sum of UNICON-simulated local and nonlocal moisture fluxes is quite similar to the CAM5-simulated local moisture flux (Fig. 2e).

The vertical profiles of the individual updraft and downdraft properties and the mixing characteristics shown in Figs. 2f–h are similar to those of the previous dry convection case, except that $\hat{a}$ does not reach to $\hat{A}_{\max}$ and $\hat{w}$ increases with height above $z = 470$ m. Similar to the dry convection case, the local turbulent eddies destabilize the PBL (Fig. 2i). Both the local and nonlocal turbulent eddies transport moisture from the lower PBL to the upper PBL (Fig. 2j) with more transport by the former. Since the CAM5 PBL scheme performs a downgradient vertical diffusion of individual $\overline{q}_v$, $\overline{q}_l$, and $\overline{q}_i$ instead of $\overline{q}_t$ (Park et al. 2014), the local turbulent eddies decrease $\overline{q}_l$ in the upper PBL and increase $\overline{q}_l$ in the lower PBL (Fig. 2k). The transported $\overline{q}_l$ in the lower PBL is evaporated by the subsequent cloud macrophysics scheme, so that the typical vertical profile of $\overline{q}_l$ shown in Fig. 2d is restored at the next time step (Park et al. 2014). Finally, we note that owing to the separate treatment of the aerosol activation and the downgradient vertical diffusion of $\overline{n}_l$ after the PBL and convection schemes in the process-splitting CAM5 (Park et al. 2014), the input $\overline{q}_l$ and $\overline{n}_l$ given to the convection scheme are not necessarily self-consistent with each other. Thus, despite the current UNICON assumption of a fixed radius of cumulus liquid droplet of 10 μm, the $\overline{n}_l$ tendency shown in Fig. 2l is not congruent with the $\overline{q}_l$ tendency shown in Fig. 2k.
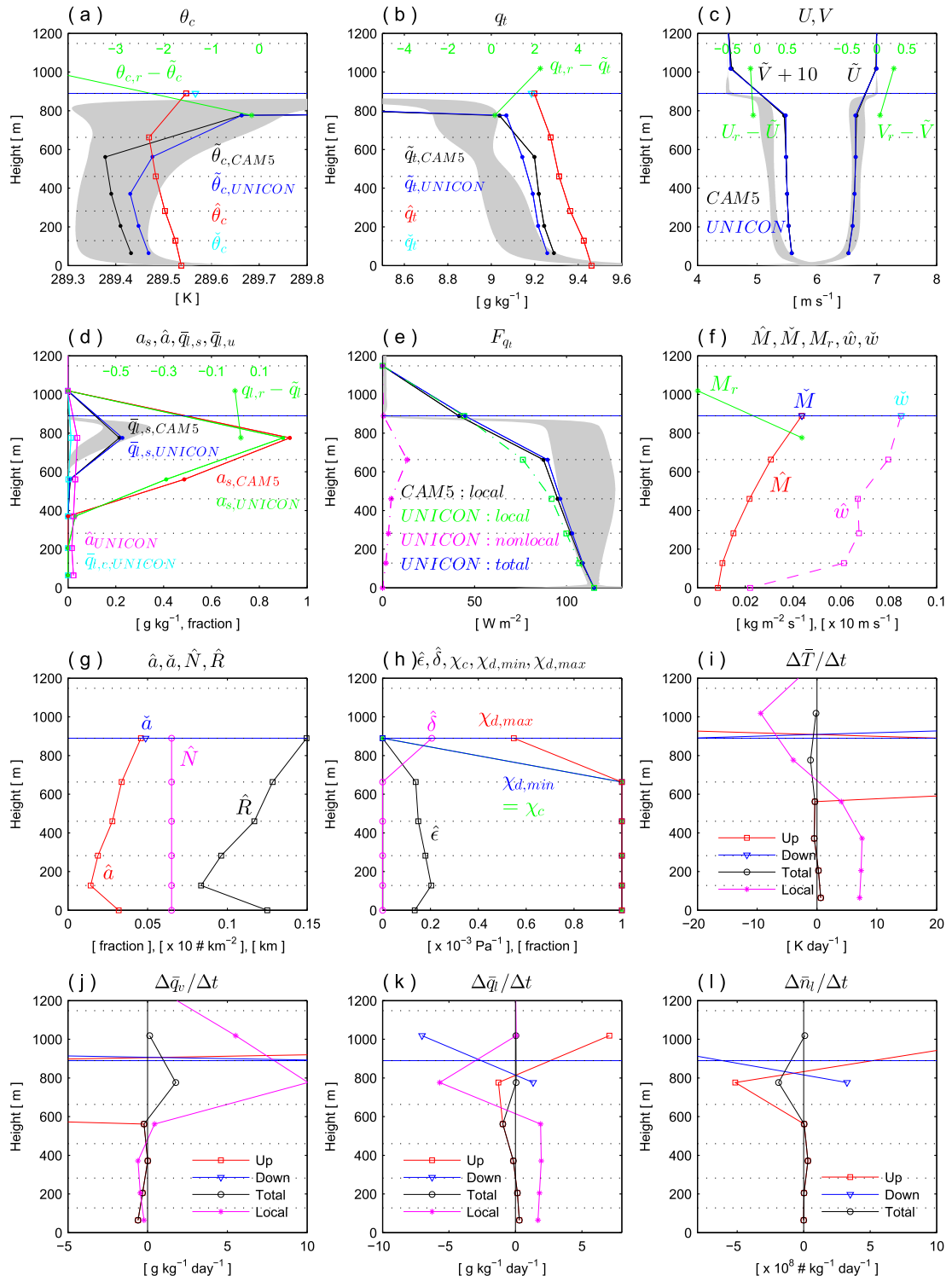
FIG. 2. A single-column simulation of the DYCOMS2 nocturnal stratocumulus-topped PBL. Time-mean (averaged over the last hour) vertical profiles with the same notation as Fig. 1, but with the addition of (c) environmental horizontal winds $\tilde{U}$, $\tilde{V}$; (d) stratus fraction a_s, grid-mean LWC by stratus $\overline{q}_{l,s}$ ($= a_s \hat{q}_{l,s}$, where $\hat{q}_{l,s}$ is in-stratus LWC), and grid-mean LWC by cumulus $\overline{q}_{l,c}$ ($= \hat{a}\hat{q}_l$, where $\hat{q}_l$ is in-cumulus LWC); (e) subgrid vertical moisture flux $F_{q_t} = \rho L_v \overline{w'q_t'}$, where ρ is the air density and L_v is the latent of vaporization; and the grid-mean tendencies of (j) water vapor and (k),(l) mass and number concentration of cloud liquid droplets, respectively. In (a)–(e), the gray shading denotes the results from various LES models.

c. Stratocumulus-to-cumulus transition

This case is designed to simulate the Lagrangian stratocumulus-to-cumulus transition over the subtropical eastern Pacific Ocean during summer (Sandu and Stevens 2011). The initial profile characterizes a well-mixed marine stratocumulus deck with an inversion layer between 910 and 915 hPa across which $\overline{\theta}_c$ ($\overline{q}_t$) increases (decreases) rapidly with height. Simulation is run for 3 days with a gradually increasing SST from 293.75 to 299.17 K at P_s = 1016.8 hPa and a time-invariant grid-mean subsidence rate that increases linearly with height from the surface to 800 hPa and is then fixed up to 700 hPa. There is no horizontal advection of heat and moisture, and the initial horizontal wind is geostrophic. The number concentration of cloud liquid droplets within stratocumulus is specified as $\hat{n}_l = 100 \text{ cm}^{-3}$. This case can be understood as a transition from the stratocumulus-topped PBL discussed in the previous section to the shallow convection case in the next section.

During the nighttime on the first day of the simulation (day 0.35–0.8), z_h frequently deepens up to z_{inv}, indicating that PBL is well mixed or coupled (Fig. 3a). This is largely due to strong LW cooling at the PBL top driven by stratocumulus that enhances TKE by reducing the vertical stratification of $\overline{\theta}_v(z)$ and also serving as the source of the positive buoyancy production just below z_h (Bretherton and Park 2009). During the daytime (days 0–0.35), however, stratocumulus becomes thin (Fig. 3c) and the PBL is decoupled (i.e., the thickness of the decoupled layer, $\Delta z_{\text{dec}} \equiv z_{\text{inv}} - z_h$, increases; Park et al. 2004). This is due to in-cloud SW warming that enhances the mean vertical stratification, dissipates the stratocumulus by direct SW radiative heating, and so weakens TKE within the PBL. As the air parcel is advected downstream over warmer SST, both z_{inv} and z_h deepen, but with a more rapid deepening of z_{inv}, Δz_{dec} also increases and the PBL is more decoupled. Note that the downstream deepening rate of z_{inv} is stronger during the nighttime than during the daytime.

Two notable differences in the simulated z_{inv} and z_h between CAM5 and UNICON are that CAM5 simulates shallower z_{inv} than UNICON particularly during the last half of the simulation and CAM5 simulates more steady z_h than UNICON after PBL is decoupled (i.e., after day 1). The former is due to the absence of the well-mixed stratocumulus and the associated TKE in the decoupled layer between z_h and z_{inv} in the CAM5 simulation (Figs. 3b–f,i) and the resulting decrease of the entrainment rate at z_{inv}. The latter is associated with the use of CIN-based updraft mass flux closure at z_h in the CAM5 shallow convection scheme. Although UNICON does

not use the CIN closure, explicit dynamic treatment of the downdraft plume as well as the updraft plume allows UNICON to mimic the stabilizing effect of the CIN closure, since if CIN becomes large at lower z_h, more convective updrafts are likely to be converted into the downdrafts at near z_h (i.e., top downdraft), which sink below z_h and deepen z_h. The same simulation with multiple updraft plumes produces more steady z_h and $\hat{z}_{\text{TOP}}$ than the single-plume simulation (not shown). It is clear that UNICON simulates more realistic z_{inv}, cloud fraction, and liquid water path (LWP) than CAM5. The rapid fluctuation of cloud fraction and LWP as z_{inv} deepens from one model interface to another model interface is the result of the discrete merging of the warm and dry layer just above z_{inv} into the decoupled layer.

Figures 3d–l show the vertical profiles of various thermodynamic variables averaged over 2 h during the time interval indicated by two vertical lines in Figs. 3a–c. The most distinct aspect of this stratocumulus-to-cumulus transition case compared to the previous dry convection and stratocumulus-topped PBLs is the decoupling of PBL induced by warm SST. The vertical profiles simulated by LES are characterized by a surface-based well-mixed layer up to $z \approx 700$ m, a stably stratified layer between $700 < z < 1200$ m in which TKE is a local minimum and $\overline{\theta}_c$ ($\overline{q}_t$) increases (decreases) with height, and an elevated mixed layer between $1200 < z < 1700$ m with a stratocumulus deck at the top of the elevated mixed layer. These LES-simulated, overall decoupling structures are well simulated by UNICON. Some convective updrafts during the averaging period are not strong enough to overcome the buoyancy barrier centered at $z \approx 900$ m, so that all $\hat{N}$, $\hat{M}$, and $\hat{a}$ decrease with height across this buoyancy barrier (in Fig. 3h, time-mean $\hat{R}$ is plotted only below this buoyancy barrier). Similar to LES, TKE is a minimum within the buoyancy barrier with two TKE maxima outside of this buoyancy barrier: one within the surface-based mixed layer driven by the buoyancy flux at the surface and the other at the top of the elevated mixed layer driven by the cloud-top LW radiative cooling and the condensation heating within the stratocumulus.

The budget analysis reveals some interesting contrasts in terms of how the local and nonlocal turbulent eddies maintain the stratocumulus deck at the top of the elevated mixed layer at $z \approx 1600$ m. The local turbulent eddies deplete $\overline{q}_l$ through a downgradient diffusion but sustain high relative humidity by bringing up the cold and moist airs from below. On the other hand, the nonlocal turbulent eddies sustain $\overline{q}_l$ through convective detrainment (Figs. 3f,l), but the penetrative entrainment (or compensating subsidence) induced by convective updraft at the cumulus top reduces the grid-mean
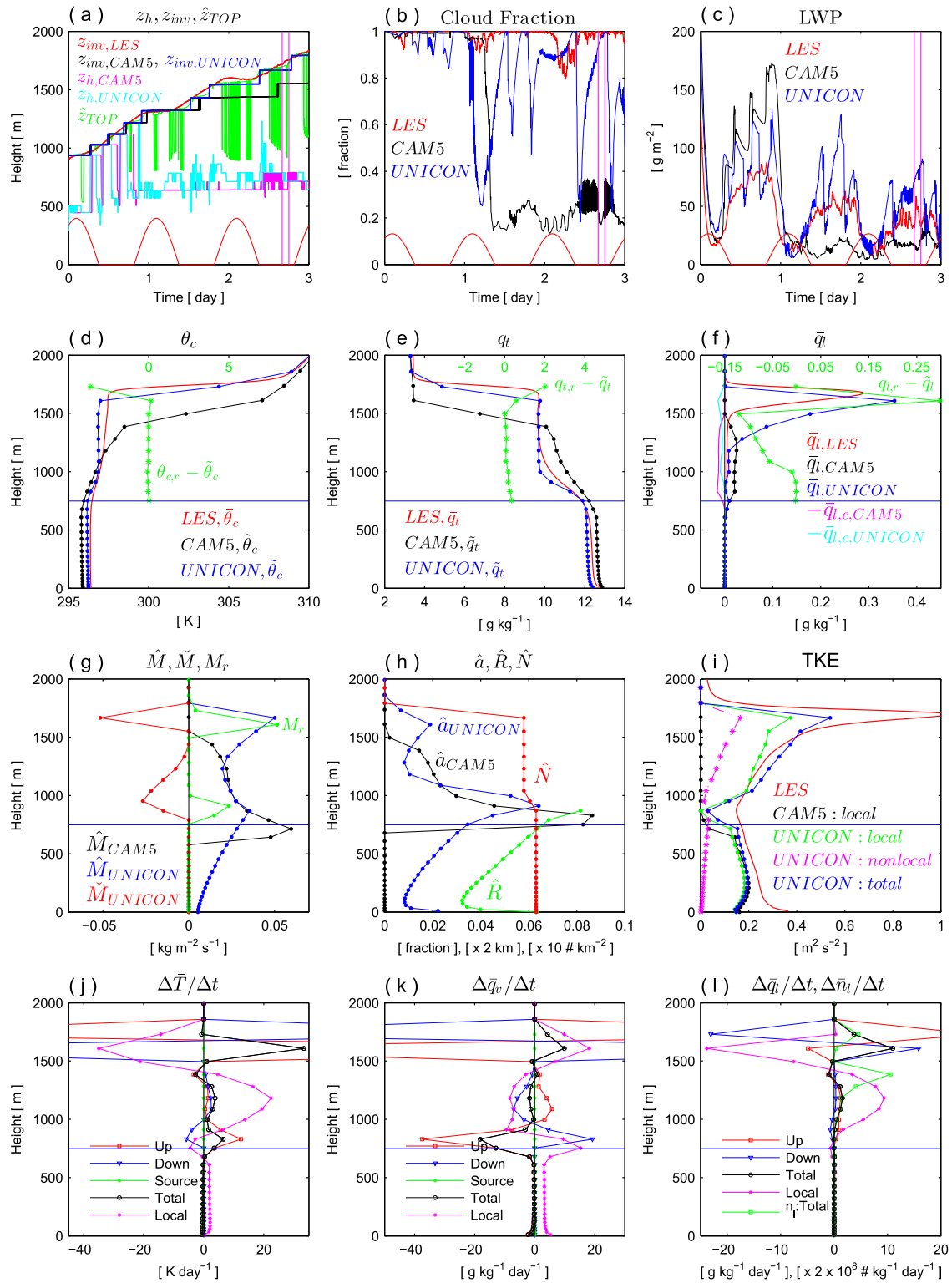
FIG. 3. A single-column simulation of the stratocumulus-to-cumulus transition case. Time series of (a) the PBL-top height z_h, the inversion-base height z_{inv} at which the vertical gradient of $\bar{\theta}_v$ is the largest, and the updraft-top height $\hat{z}_{TOP}$; (b) total cloud fraction; and (c) LWP, with a scaled downward shortwave radiative flux at the top of the atmosphere denoted by the red curve at the bottom of each panel. Also shown are time-mean [averaged over the time interval indicated in (a)–(c)] vertical profiles with notation as in Figs. 1 and 2, but with the addition of (f) grid-mean LWC $\bar{q}_l$ ($=\bar{q}_{l,s} + \bar{q}_{l,c}$) and (j),(k) grid-mean tendency by the source within the environment [Source: the last term on the rhs of Eq. (17)]. (l) For $\bar{n}_l$, only total convective tendency is shown.

relative humidity (Figs. 3j,k) and the stratocumulus fraction. Overall, UNICON is much better than CAM5 in reproducing the LES-simulated stratocumulus-to-cumulus transition.

d. Shallow convection over the ocean

In this section, we show the single-column simulation of a shallow convection case over the ocean, the Barbados Oceanography and Meteorology Experiment (BOMEX; Holland and Rasmusson 1973) described by Siebesma et al. (2003). The BOMEX case is forced by constant LHF = $153 \, \mathrm{W \, m^{-2}}$ and SHF = $9.5 \, \mathrm{W \, m^{-2}}$ at SST = $300.4 \, \mathrm{K}$ and $P_s = 1015 \, \mathrm{hPa}$. Starting from the given initial profile, simulation is run for 6 h by turning off both SW and LW radiations, but with the specified grid-mean forcings of cold and dry horizontal advection, subsidence, and geostrophic wind, following Park and Bretherton (2009).

Figure 4 shows the vertical profiles of various thermodynamic variables averaged over the last 3 h from CAM5, UNICON, and LES. The LES profiles of convective updraft plumes (red solid lines in Figs. 4d–f) are obtained by averaging the core cloudy updraft pixels defined as the area of positive buoyancy, cloud water, and vertical velocity. For reference, we also plotted the average profiles of the cloudy updraft pixels (red dotted lines in Figs. 4d–f), which contain negatively buoyant, detrained cumulus plumes as well as positively buoyant cumulus plumes. For comparison with CAM5 and UNICON, we should use the core cloudy updraft pixels, particularly in the region below LNB, since the detrained convective updraft is not a part of the convective updraft plume simulated by CAM5 and UNICON. Because of conditional sampling, the cumulus updraft properties simulated by LES are defined only above the cloud base. Because the updraft plume is launched from the PBL top, the convective updraft properties simulated by CAM5 are not defined within the PBL. In contrast, UNICON launches updraft plumes from the surface and simulates both the dry and moist convection in a unified way, so that convective updraft properties are defined from the surface to the cumulus top. We also show two sensitivity simulations from UNICON with the intercept radius of the updraft plume at the surface at the nonorganized state, $R_o|_{\Omega=0} = 50 \, \mathrm{m}$ [Eqs. (23) and (76)], and the e-folding radius of the updraft buoyancy coefficient, $R_a = 0 \, \mathrm{m}$ [which is equivalent to assuming a constant buoyancy coefficient; $a(\hat{R}) = 1/3$ in Eq. (29)] with $\hat{A}_s|_{\Omega=0} = 0.05$ (see Table 1).

UNICON simulates better $\tilde{\theta}_c(z)$ and $\tilde{q}_t(z)$ than CAM5, particularly in the upper cumulus layer and the penetrative entrainment zone above $z = 1000 \, \mathrm{m}$. Compared to LES, CAM5 simulates warmer and drier air in

the layers $1000 < z < 1630 \, \mathrm{m}$, and colder and moister air farther above, implying that the parameterized penetrative entrainment mixing is too strong in the CAM5 shallow convection scheme (Park and Bretherton 2009; Park et al. 2014). Because of the dynamic treatment of convective downdrafts, UNICON does not need a separate penetrative entrainment closure but substantially improves the simulation. The improved simulation of the convective updraft properties is also encouraging: UNICON simulates better fractional area $\hat{a}(z)$, vertical velocity $\hat{w}(z)$, and the mass flux $\hat{M}(z)$ of convective updraft plumes than CAM5.

Within the PBL, the mixing characteristics between the convective updraft and the environmental air are similar to the previous cases of dry convective and stratocumulus-topped PBL (Fig. 4i). The mixing characteristics in the cumulus layer, however, are quite different from those within the PBL: $\hat{\epsilon}(z)$ has a parabolic shape with a maximum value at around $z_m = (z_h + z_{\mathrm{LNB}})/2$, but $\hat{\delta}(z) > \hat{\epsilon}(z)$ increases rapidly above z_m, with most of the detrained mixtures being converted into the mixing downdraft. It is interesting to note that even in this shallow convection case without convective precipitation, UNICON simulates nonnegligible downdraft mass flux ($\check{M}$ in Fig. 4g), which is the sum of the top downdraft near the cumulus top and the mixing downdrafts in the other cumulus layers. Without being forced by the evaporation of convective precipitation, however, the mixing downdrafts generated from the mixing between saturated convective updraft and the mean environmental air (see Fig. 4b in Part I) can move down only a short distance from their origination levels and are detrained into the conditionally unstable cumulus layer without penetrating into the PBL (M_r in Fig. 4g). While treated in the same way within UNICON, $\check{M}$ shown in Fig. 4g should be distinguished from the conventional convective downdraft mass flux in the precipitating deep convection system, which, after being generated, is forced by evaporation of convective precipitation and moves a long distance downward, penetrating into the PBL, and generating a cold pool and mesoscale organized flow within the PBL.

In UNICON, the mixing between the convective updraft and environmental air is controlled by the updraft plume radius $\hat{R}(z, t)$ [Eq. (31)], whose vertical and time evolution are internally computed, once the values at the nonorganized and maximally organized states are specified at the surface [Eqs. (23), (30), (76), and (77)]. The updraft plume radius also controls the vertical evolution of the vertical velocity and the fractional area of convective updraft plume by modulating the buoyancy coefficient [Eq. (29)]. In the lower PBL, $\hat{R}$ decreases with height but increases afterward, reaches to
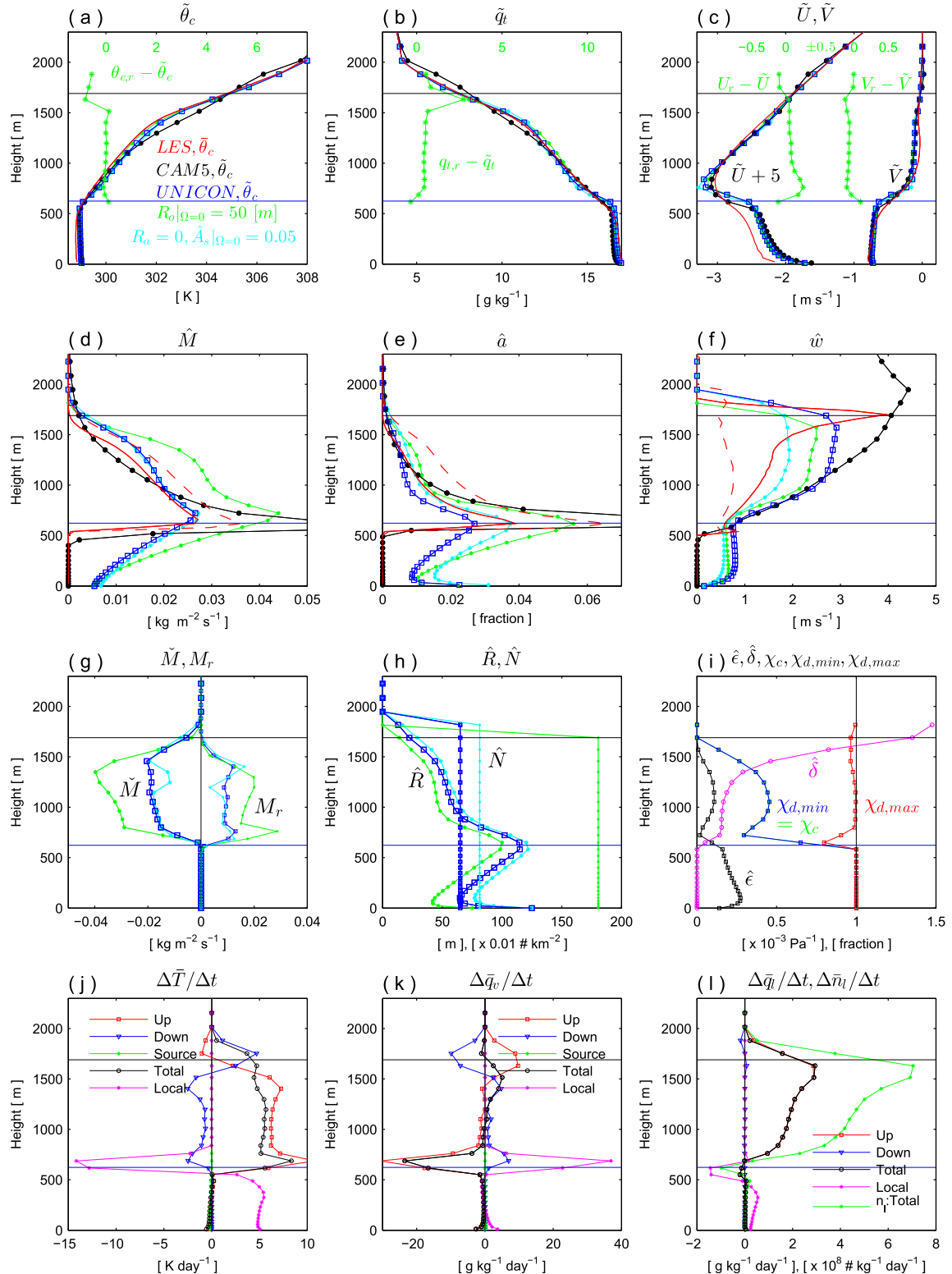
FIG. 4. A single-column simulation of the BOMEX shallow convection case. Time-mean (averaged over the last 3 h) vertical profiles with notation as in Fig. 3, but (a)–(h) with the addition of two sensitivity simulations from UNICON with a common legend in (a). In (a)–(c), $\psi_r - \tilde{\psi}$ ($\psi = \theta_c, q_t, U, V$) is from the default UNICON simulation. In (d)–(f), the red solid (red dotted) line denotes the average for core cloudy updrafts (cloudy updrafts) from LES. In each panel, the black horizontal line denotes the LNB of convective updraft.

the maximum at just above the PBL top, and gradually decreases farther above. Even in this shallow convection case, $\hat{R}$ shows a rich variation with height, in contrast to the implicit assumption used in the existing convection schemes (Arakawa and Schubert 1974; Tiedtke 1989; Kain and Fritsch 1990).

Shallow moist convection warms the cumulus layer, transports water vapor from the lower to the upper cumulus layer, and detrains convective condensates at any height within the cumulus layer (Figs. 4g,j–l). Most of these tendencies are associated with the convective updrafts, but convective downdraft also plays an important role in the layers just above z_h and near LNB. Note that in the layer just above z_h, convective updraft offsets the tendencies of $\overline{T}$ and $\overline{q}_v$ induced by the PBL scheme.

Although better than CAM5, one notable bias in the UNICON simulation is stronger $\hat{w}$ in the cumulus layer [Fig. 4f, where very large $\hat{w}$ in the stable penetrative entrainment zone above $z = 1500$ m in the LES is an artifact of the conditional sampling of the rare core cloudy updrafts, since cloudy updrafts do not show large $\hat{w}$ there], which, in turn, results in smaller $\hat{a}$ than the LES (Fig. 4e). A sensitivity simulation with a smaller updraft plume radius ($R_o|_{\Omega=0} = 50$ m instead of the default 100 m) reduces the bias of $\hat{w}$ but degrades $\hat{M}$, with a lower cumulus-top height as expected. Another sensitivity simulation with $R_a = 0$ and $\hat{A}_s|_{\Omega=0} = 0.05$, however, substantially reduces the biases of $\hat{w}(z)$ and $\hat{a}(z)$ without degrading $\hat{M}(z)$. As will be shown later (S.7 in Table 2), this choice of model parameters also improves the global simulation, although it warms the global climate system.

e. Deep convection over land

This case is from the intensive observation of deep convection over the southern Great Plains in the United States (36.6°N, 97.5°W) during the Atmospheric Radiation Measurement Program in summer 1997 (ARM97; Stokes and Schwartz 1994). A single-column model is run for 29 days (18 June–17 July 1997) with an interactive land model, internally computed radiation, and the specified vertical profiles of time-varying horizontal advective forcings of temperature and moisture and the grid-mean subsidence rate from Zhang et al. (2001).

Figure 5 shows the simulated time series of surface precipitation rate and the anomalous vertical profiles of $\overline{T}$ and $\overline{q}_v$ with respect to the observation. While some discrepancies exist, both CAM5 and UNICON well capture the observed main precipitation events (Fig. 5a). UNICON simulates a few unrealistic precipitation maxima (e.g., around days 6, 9, and 17.5), which, however, tend to be suppressed if different numerical

methods (e.g., centered Eulerian difference) are used for the vertical advection of grid-mean scalars (not shown). In addition to the conventional grid-mean horizontal advection of temperature and moisture, UNICON requires the horizontal advection of the cold pool properties as input conditions [which is simply set to zero for this test simulation in Eqs. (61)–(64)], particularly in order to simulate propagating deep convection. As well as the numerics, the absence of this information is also likely to be responsible for the several unreasonable precipitation maxima. Most of the strong convective precipitation simulated by UNICON is associated with the cold pool ($\Omega > 0$) and the associated positive perturbations of the updraft vertical velocity ($\Delta w_\Omega > 0$), temperature ($\Delta\theta_{c,\Omega} > 0$), moisture ($\Delta q_{t,\Omega} > 0$), and the updraft plume radius at the surface $\hat{R}_{\text{sfc}}$ (Fig. 5b). In contrast to $\Delta\theta_{c,\Omega}$, $\Delta q_{t,\Omega}$ can be either positive or negative with a stronger (weaker) convective precipitation when $\Delta q_{t,\Omega}$ is positive (negative). CAM5 simulates large cold and dry biases against the observation (Figs. 5c,d), which, however, are substantially reduced in the UNICON simulation (Figs. 5e,f).

Figure 6 shows the vertical profiles of various thermodynamic variables at the instantaneous time step indicated by the black vertical line in Fig. 5. A set of convective updraft plumes rises from the surface with $\hat{w} = 0.91$ m s^{-1}, $\hat{M} = 0.022$ kg m^{-2} s^{-1}, $\hat{a} = 2.2\%$, $\hat{R} = 518$ m, $\hat{N} = 0.026$ km^{-2}, and the perturbations of thermodynamic scalars with respect to the environmental mean, $\delta\hat{\theta}_c \equiv \hat{\theta}_c - \tilde{\theta}_c = 1.8$ K, $\delta\hat{q}_t = 0.012$ g kg^{-1}, $\delta\hat{u} = -0.43$ m s^{-1}, and $\delta\hat{\theta}_v = 1.8$ K. A portion of these perturbations is due to the subgrid cold pool ($\Omega = 0.1$) and the associated subgrid mesoscale organized flow (Fig. 5b). Within the PBL, vertical evolution of the updraft properties is similar to the previous cases. At $z = 773.7$ hPa, the updraft plume contains enough condensate to generate negatively buoyant mixtures by the evaporative cooling during the mixing (Figs. 6b,f). As a result, only a portion of the mixtures are entrained ($0 < \chi < \chi_c$, where $\chi_c = 0.45$), and the remaining mixtures are either detrained into the environment ($\chi_{d,\max} < \chi < 1$, where $\chi_{d,\max} = 0.90$) or converted into the mixing downdraft ($\chi_{d,\min} < \chi < \chi_{d,\max}$, where $\chi_{d,\min} = \chi_c = 0.45$). Since $\chi_c < 0.5$, $\hat{M}$ decreases with height, but $\hat{w}$ increases rapidly owing to the decrease of entrainment drag, resulting in the decrease of $\hat{a}$ and $\hat{R}$ with height. The LNB is located at $z_{\text{LNB}} = 287.7$ hPa where $\delta\hat{\theta}_v = -0.24$ K and $\hat{w} = 3.4$ m s^{-1}, and the updraft top height is $\hat{z}_{\text{TOP}} = 11.65$ km slightly above the LNB. Since the updraft plume at the top is negatively buoyant, it sinks from the top (i.e., top downdraft). At the LNB, $\chi_{d,\min} = \chi_c = 0.19$ and $\chi_{d,\max} = 1$, so that all of the nonentrained mixtures are converted into the mixing
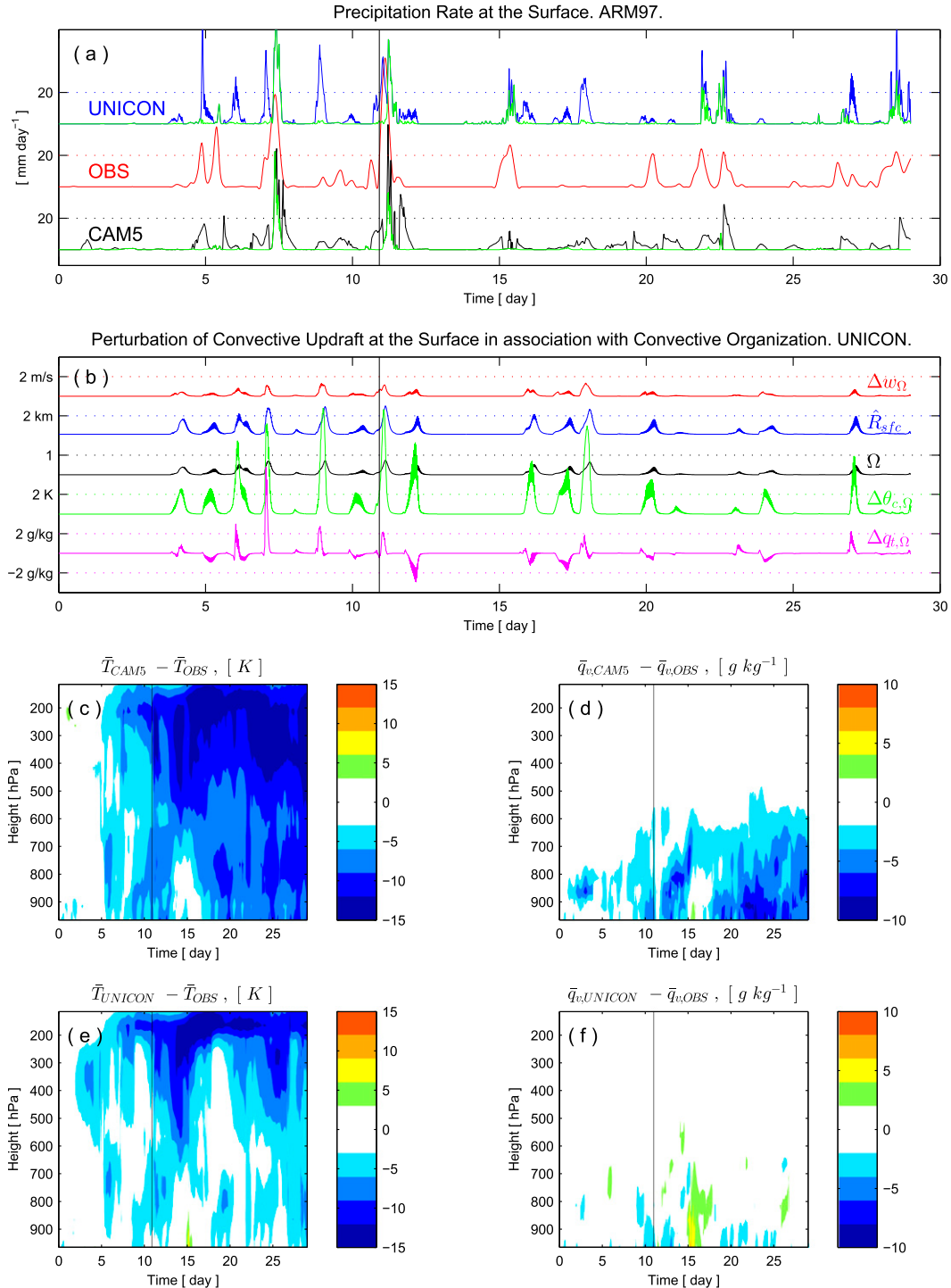
FIG. 5. A single-column simulation of the ARM97 deep convection case over land. Time series of (a) total precipitation rate at the surface with the green line denoting stratiform precipitation rate from UNICON and CAM5 simulations and (b) mesoscale convective organization Ω [Eq. (72)]; mesoscale perturbations of θ_c, q_t, and w in the upflow region of mesoscale organized flow within the PBL ($\Delta\theta_{c,\Omega}, \Delta q_{t,\Omega}, \Delta w_\Omega$) [Eqs. (73) and (74)]; and updraft plume radius at the surface $\hat{R}_{sfc}$ [Eqs. (23), (76), and (77)] simulated by UNICON. Time–height plots of the simulated biases of grid-mean temperature and water vapor against the observation from (c),(d) CAM5 and (e),(f) UNICON, with the biases less than ± 3 K and ± 2 g kg^{-1} denoted by white. A vertical line in each plot denotes the time step at which the vertical profile will be shown in Fig. 6.
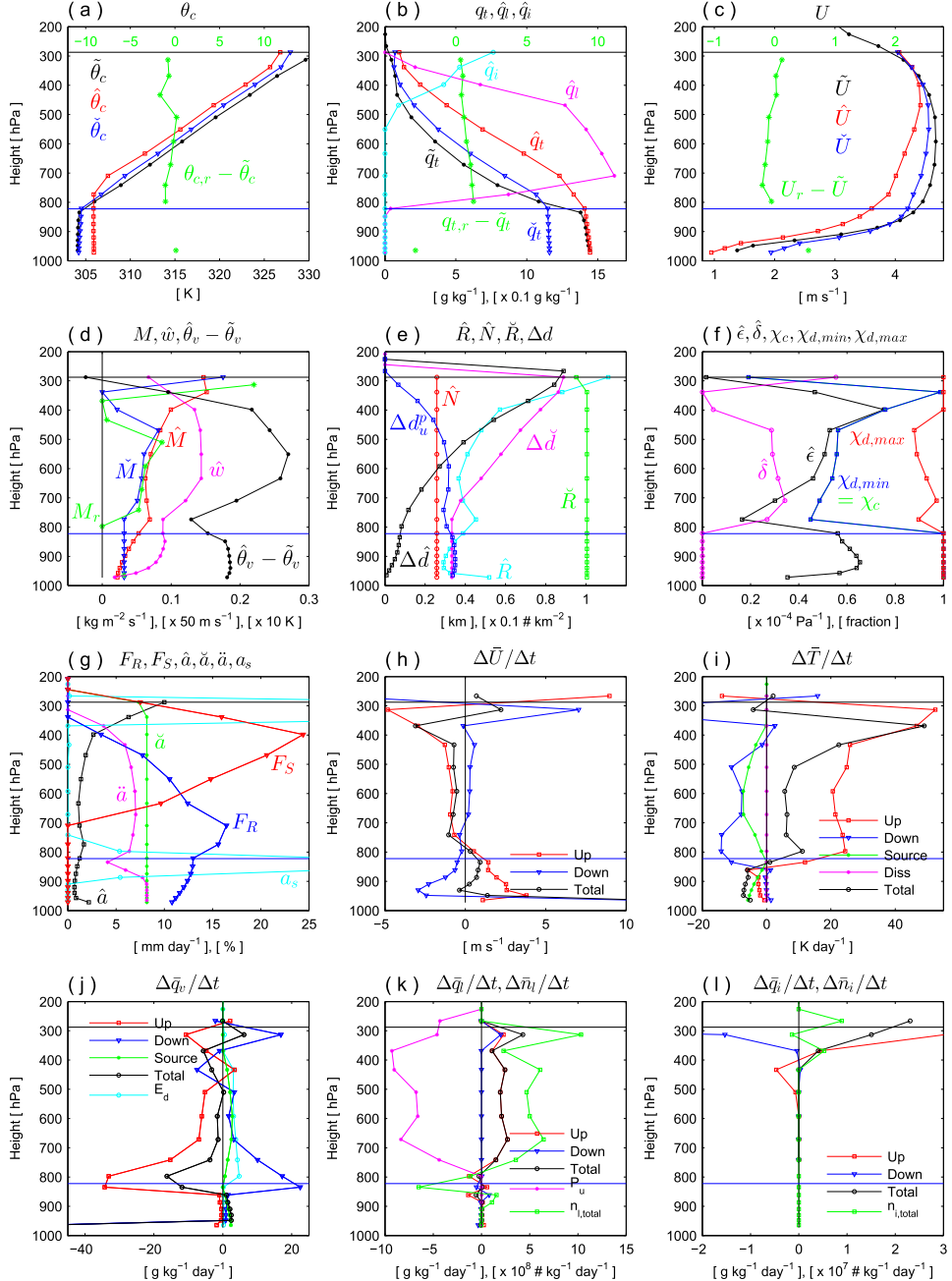
FIG. 6. A single-column simulation of the ARM97 deep convection. Vertical profiles at the instantaneous time step indicated in Fig. 5 with notation as in the previous figures, but with the addition of (b) in-cumulus LWC and IWC $\hat{q}_l$, $\hat{q}_i$; (e) radius of convective precipitation $\check{R}$, $\Delta\hat{d}\equiv\sqrt{[\hat{x}(z)-\hat{x}(0)]^2+[\hat{y}(z)-\hat{y}(0)]^2}$, $\Delta\check{d}\equiv\sqrt{[\check{x}(z)-\hat{x}(0)]^2+[\check{y}(z)-\hat{y}(0)]^2}$, and $\Delta d_u^p\equiv\sqrt{[\check{x}(z)-\hat{x}(z)]^2+[\check{y}(z)-\hat{y}(z)]^2}$, where $[\hat{x}(z),\hat{y}(z)]$ and $[\check{x}(z),\check{y}(z)]$ are the centers of updraft plume and convective precipitation at each level, respectively; (g) grid-mean fluxes of convective rain F_R and snow F_S, convective precipitation area $\check{a}$, and evaporation area of convective precipitation $\ddot{a}$; (i) dissipation heating of mean kinetic energy [Diss; Eq. (88)]; (j) grid-mean evaporation rate of convective precipitation within convective downdrafts $E_d=g\sum_j\check{M}^j(\check{S}_{q_v}^{e,R,j}+\check{S}_{q_v}^{e,S,j})$; and (k) grid-mean production rate of convective precipitation $P_u=g\sum_i\hat{M}^i(\hat{S}_{q_l}^{\mathrm{pr},i}+\hat{S}_{q_i}^{\mathrm{pr},i})$. In each panel, the black horizontal line denotes the LNB.

downdraft (we note that at some other time steps, $\chi_c < \chi_{d,\min}$ rather than $\chi_c = \chi_{d,\min}$ as shown in Fig. 4 of Part I). Both the top and mixing downdrafts contribute to the downdraft flux at the base interface of the updraft-top layer. The mixing downdrafts are also generated in the layers between $z = 773.7$ hPa and the LNB (Fig. 6f), which are cooled by the evaporation of convective rain and snow, sink, and are eventually detrained into their neutral buoyancy layers. In contrast to the previous four cases, some convective downdrafts can sink all the way down to the surface through the cold pool [$\check{M}_D$ in Eqs. (61)–(64) and Fig. 6d].

UNICON has the following convective microphysical processes: production of convective precipitation within the updraft [P_u in Fig. 6k; Eqs. (17) and (38)], evaporation of convective precipitation and snow melting within the environment [source in Figs. 6i,j; Eqs. (17) and (79)], and evaporation of convective precipitation within the downdraft [E_d in Fig. 6j; Eqs. (17) and (51)]. The resulting grid-mean convective rain (F_R) and snow fluxes (F_S) are shown in Fig. 6g, along with the updraft fractional area, convective precipitation area [$\check{a}$; Eq. (85)], evaporation area [$\ddot{a}$; Eq. (80)], and the distance between the centers of the convective updraft plume $(\hat{x}, \hat{y})$ and the convective precipitation area $(\check{x}, \check{y})$ in each layer [$\Delta d_u^p \equiv \sqrt{(\check{x} - \hat{x})^2 + (\check{y} - \hat{y})^2}$ in Fig. 6e where $(\check{x}, \check{y})$ is from Eq. (86)], which are the main variables used for computing convective microphysics within UNICON. At LNB, all convective precipitation is snow because $\hat{T} < 233$ K, but the fraction of rain gradually increases as $\hat{T}$ increases. At $z = 709.7$ hPa, all snow is melted into rain because $\tilde{T} \geq 273.15$ K [Eq. (87)]. At LNB, $\check{a} = 7.35\%$ and $\check{R} = 952.2$ m, while at the layer midpoint just below the LNB, $\hat{a} = 8.15\%$ and $\hat{R} = 996.5$ m with $\Delta d_u^p = 47.8$ m. Under this configuration, $\check{a}$ is near–fully overlapped with the underlying precipitating $\hat{a}$, and so $\check{a}$ and $\check{R}$ slightly increase to $\check{a} = 8.19\%$ and $\check{R} = 1005.3$ m at the next interface below. In all the layers farther below, $\hat{a}$ is completely overlapped with the larger $\check{a}$ (see $\hat{R}$, $\check{R}$, and Δd_u^p), and a constant $\check{a} = 8.19\%$ is maintained all the way down to the surface, implying that convective precipitation is not completely evaporated within $\ddot{a}$ and the downdraft in each layer. Note that except within the PBL, the amount of evaporated convective precipitation within the downdraft (E_d in Fig. 6j) is comparable to or larger than the evaporated amount within the environment (source in Fig. 6j).

The budget analysis is shown in Figs. 6h–l. To the first order, in the layers above z_h, convective updraft warms and dries the atmospheric column through the compensating subsidence, while convective downdraft plays the opposite role through the compensating upwelling. With larger impact by convective updraft, the atmospheric column becomes warm and dry by compensating vertical motions. Convective detrainment also contributes to the budget. The strongest detrainment occurs in the layer just below the LNB (M_r in Fig. 6d), which contributes to generating or dissipating ice stratus, depending on whether the detrained convective ice condensate is larger or smaller than the preexisting stratus ice condensate. Substantial detrainment also occurs in the midtroposphere between $z = 468.4$ and $z = 773.7$ hPa (Figs. 6d,f). In these layers, stratus does not exist, so that $\overline{q}_l$ and $\overline{n}_l$ increase by convective detrainment. UNICON assumes that convective detrainment occurs randomly without a preferred spot in each layer. As a result, some of the detrained cumulus liquid condensate is deposited in the preexisting stratus, while some is detrained into the clear portion, which will be evaporated in the subsequent cloud macrophysics scheme (Park et al. 2014). Below z_h, convection cools and moistens the PBL through the evaporation of convective precipitation within the environment and the export of heat by convective updraft out of the PBL. Dissipation heating of the mean kinetic energy is negligibly small in this case [Fig. 6i; Eq. (88)]. In the lowest model layer, convective downdraft strongly enhances $\overline{U}$ and decreases $\overline{q}_v$, because $\check{U}$ (or U_r) $> \tilde{U}$ and $\check{q}_v$ (or $q_{v,r}$) $< \tilde{q}_v$ in the lowest model layer (Figs. 5b,c,h,j).

4. Global climatologies

a. Global annual-mean statistics

Figure 7 shows a Taylor diagram (Taylor 2001) summarizing various statistics for global simulations compared with observations. The observation and reanalysis data that will be used for evaluating the simulations in this paper are the Global Precipitation Climatology Project (GPCP; Adler et al. 2003), Climate Prediction Center (CPC) the Merged Analysis of Precipitation (CMAP; Xie and Arkin 1996), the Tropical Rainfall Measuring Mission (TRMM) Multisatellite Precipitation Analysis (TMPA; Huffman et al. 2007), the Clouds and Earth's Radiant Energy Systems Energy Balanced and Filled (CERES EBAF; Loeb et al. 2009), the Earth Radiation Budget Experiment (ERBE; Harrison et al. 1990), the International Satellite Cloud Climatology Project (ISCCP; Rossow and Schiffer 1991), the *CloudSat* Experiment (CLOUDSAT; Stephens et al. 2002), the Extended Edited Cloud Report Archive (EECRA; Hahn and Warren 1999), the European Remote Sensing Satellite Scatterometer (ERS; Bentamy et al. 1999), the Willmott–Matsuura surface air temperature (Willmott; Willmott and Matsuura 1995), the National Aeronautics and Space Administration (NASA) Water Vapor Project (NVAP; Randel et al. 1996), liquid water path from
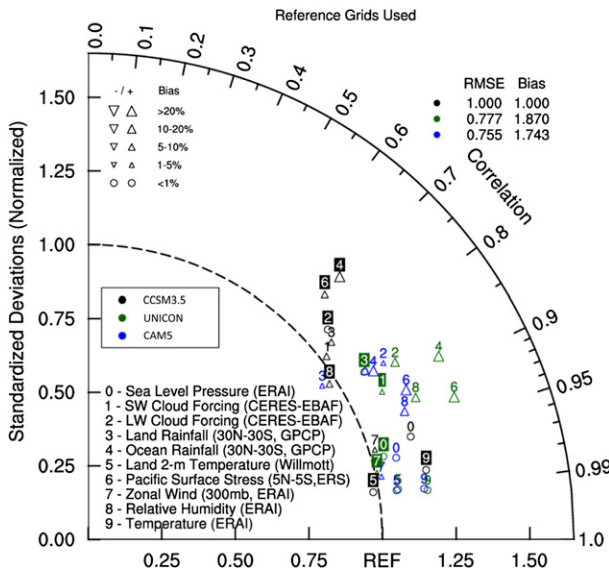
FIG. 7. A space–time Taylor diagram showing the global performance of UNICON (green) and CAM5 (blue) relative to CCSM3.5 (black) against the observations measured by the correlation and standardized deviation of 10 semi-independent climate variables. For each variable, we compute correlation with the observation using all the monthly-mean values over all the available grid points and standardized deviation as the ratio of the simulated spatiotemporal standard deviation to the observed standard deviation. Standardized deviation larger (smaller) than 1 indicates that the simulation has larger (smaller) spatiotemporal variability than the observations, including the annual cycle. Any variable with a correlation of 1 and a standardized deviation of 1 indicates a perfect simulation of that variable. The RMSE = 0.777 (0.755) of UNICON (CAM5) is the average of relative RMSE of a simulated individual variable against the observation with respect to the RMSE of CCSM3.5 {i.e., RMSE(UNICON) = $(1/10)\sum_{i=0}^{9}[\mathrm{RMSE}_i(\mathrm{UNICON})/\mathrm{RMSE}_i(\mathrm{CCSM3.5})]$, where i is a variable index indicated on the lower-left portion of the figure}. The Bias = 1.870 (1.743) of UNICON (CAM5) is the average of relative mean of an individual variable with respect to CCSM3.5 {i.e., Bias(UNICON) = $(1/10)\sum_{i=0}^{9}[\mathrm{mean}_i(\mathrm{UNICON})/\mathrm{mean}_i(\mathrm{CCSM3.5})]$, where mean_i is a time–space average value of the ith variable}. For this diagram, we chose Pacific surface stress (variable 6) along a narrow strip over the equatorial Pacific (5°N–5°S) and zonal wind (variable 7) at the 300-hPa level.

the University of Wisconsin Climatology (UWisc; O'Dell et al. 2008), and the National Centers for Environmental Prediction (NCEP)–NCAR reanalysis (NCEP–NCAR; Kalnay et al. 1996), the 40-yr European Centre for Medium-Range Weather Forecasts (ECMWF) Re-Analysis (ERA-40; Uppala et al. 2005), the Interim ECMWF Re-Analysis (ERA-Interim; Simmons et al. 2007), and the Japanese 25-yr Reanalysis Project (JRA-25; Onogi et al. 2007).

The global performance of UNICON is similar to CAM5 with a relative (with respect to CCSM3.5) spatiotemporal RMSE of 0.777 (0.755 for CAM5). Overall,

UNICON simulates better correlations than CAM5, with the largest improvement in shortwave cloud radiative forcing (SWCF), ocean rainfall, and Pacific surface stress. However, UNICON amplifies the spatiotemporal variabilities of ocean rainfall and Pacific surface stress, which offsets the improved correlations, resulting in similar RMSE to CAM5. We note that the Pacific surface stress used in our Taylor diagram is defined along a narrow strip of the equatorial Pacific (5°N–5°S) as a proxy for ENSO forcing, which has limitations in representing global performance. In fact, UNICON simulates better surface wind stress than CAM5 if the analysis domain is extended to the globe (Fig. 11).

Table 2 lists global annual-mean values of important moist variables (see the rows of OBSERVATION, CAM5: AMIP, and UNICON:AMIP). The net downwelling radiation at the top of the atmosphere (RESTOA) simulated by UNICON is near zero, maintaining the global radiation balance. In these uncoupled simulations, both CAM5 and UNICON simulate larger column-integrated water vapor path (WVP) and total precipitation rate at the surface (PRECT) than the observations. Compared with CAM5, UNICON simulates weaker SWCF and longwave cloud radiative forcing (LWCF) in association with smaller total cloud fraction [CLDTOT; particularly, low-level cloud fraction (CLDLOW) rather than high-level cloud fraction (CLDHGH)], LWP, and ice water path (IWP). However, larger PRECT, latent heat flux (LHF), and sensible heat flux (SHF) are simulated, implying a stronger hydrological cycle with UNICON. It is interesting to note that larger PRECT simulated by UNICON is associated with larger stratiform precipitation (PRECL) but smaller convective precipitation (PRECC) than CAM5, implying that stronger convective activity in CAM5 weakens the global hydrological cycle (and so decreases PRECL and PRECT) by stabilizing the atmospheric column. The AOD simulated by UNICON is slightly smaller than CAM5. UNICON simulates more realistic upward longwave radiative flux at the top of the atmosphere (238.0 W m^{-2}) than CAM5 (233.8 W m^{-2}, and the observation from CERES EBAF is 239.6 W m^{-2}) (not shown).

b. Precipitation rate at the surface

Figure 8 shows PRECT from CAM5, CMAP satellite-derived observational estimates, and UNICON during December–February (DJF) and June–August (JJA). The global-mean PRECT simulated by UNICON (3.02 mm day^{-1} in DJF and 3.09 mm day^{-1} in JJA) is slightly larger than CAM5 (2.98 mm day^{-1} in DJF and 3.06 mm day^{-1} in JJA) that already precipitates about 10% more than the observations. Stephens et al. (2012)

TABLE 2. Sensitivity simulations to various model parameters in UNICON. See sections 4a and 7 for details.

S	Type	Taylor score RMSE/bias	RESTOA ($W\,m^{-2}$)	WVP (mm)	LWP/IWP ($g\,m^{-2}$)	CLDTOT (%)	CLDLOW/HGH (%)	SWCF/LWCF ($W\,m^{-2}$)	PRECT ($mm\,day^{-1}$)	PRECC/L ($mm\,day^{-1}$)	LHF/SHF ($W\,m^{-2}$)	AOD
	Observation	—	0	24.25–24.95	79.0–87.0	55.9–66.8	40.0/40.3	−47.1–54.2/ 26.5–30.4	2.67–2.69	—	82.4–87.9/ 15.8–19.4	0.146
	CAM5:AMIP	0.755/1.743	−1.2	25.69	53.4/18.7	65.8	45.6/38.8	−54.6/25.4	2.992	2.12/0.87	87.5/18.1	0.136
	UNICON:AMIP	0.777/1.870	0.4	25.91	49.4/16.6	62.5	39.5/38.8	−49.1/23.3	3.021	1.95/1.07	88.3/18.6	0.132
	CAM5	0.824/1.816	0.3	25.69	53.4/18.9	65.7	45.5/38.9	−54.9/25.5	2.969	2.11/0.86	86.8/18.1	0.137
	UNICON	0.849/2.038	1.9	25.89	49.1/16.6	62.4	39.3/38.8	−49.3/23.3	3.002	1.95/1.06	87.7/18.4	0.133
1	$\hat{n}_s = 5$	0.853/1.827	4.2	25.90	46.5/17.5	61.7	36.8/39.5	−47.4/23.8	2.972	1.97/1.00	86.9/18.1	0.131
2	$\hat{A}_{max} = 0.2$	0.846/2.043	2.3	25.93	48.6/17.1	62.7	39.5/39.1	−49.3/23.6	2.999	1.97/1.03	87.7/18.3	0.132
3	$\hat{w}_{min} = 0.5$	0.881/1.962	1.9	25.54	50.6/16.1	62.1	39.1/38.2	−49.4/23.0	3.010	1.88/1.13	88.0/18.3	0.129
4	$k_w = 0.7$	0.847/1.960	6.4	25.96	43.5/17.1	60.5	34.9/39.3	−45.1/23.7	2.966	2.00/0.96	86.7/17.8	0.128
5	$R_a = \infty$	0.847/2.124	1.1	25.75	48.3/14.2	62.0	39.6/38.1	−48.8/22.5	3.033	1.94/1.09	88.7/18.6	0.138
6	$R_a = 0$	0.836/1.931	3.3	25.92	48.3/17.2	62.0	38.2/38.9	−48.0/23.4	2.977	1.91/1.06	87.0/18.6	0.132
7	$R_a = 0$, $\hat{A}_s^{ocn}\|_{\Omega=0} = 0.05$	0.840/1.856	5.1	25.87	46.2/17.2	60.9	36.0/39.0	−46.1/23.3	2.966	1.95/1.02	86.7/18.3	0.129
8	$b = 1$	0.849/2.168	4.1	25.72	44.2/16.1	60.7	37.3/38.4	−45.9/22.6	3.024	2.06/0.97	88.4/18.2	0.134
9	$a_2 = 0$	0.865/1.741	4.3	26.08	45.8/16.8	63.0	38.3/40.0	−48.4/24.7	2.947	1.93/1.01	86.2/18.1	0.132
10	$p = 1$	0.843/1.897	3.5	26.17	46.8/16.7	62.1	38.4/39.1	−48.1/23.7	2.984	1.97/1.02	87.2/18.3	0.132
11	$r_c = 0.3$	0.849/2.051	1.7	25.81	48.7/16.3	62.3	39.7/38.7	−49.1/23.1	3.011	1.97/1.04	88.0/18.5	0.135
12	$c_m = 0.1$	0.858/2.250	1.4	25.82	49.3/16.3	62.3	39.6/38.4	−49.3/23.2	3.005	1.97/1.03	87.8/18.7	0.133
13	$\hat{\epsilon}, \hat{\delta} = 5 \times 10^{-4}$	0.862/2.047	2.0	26.21	49.4/19.4	63.2	39.6/40.3	−50.3/24.5	2.977	1.93/1.05	87.0/18.3	0.136
14	$C_d = 1 \times 10^{-3}$	0.838/2.016	2.9	25.91	47.8/16.8	62.1	38.4/39.0	−48.5/23.5	2.991	1.96/1.03	87.5/18.4	0.132
15	$\delta\theta_{v,D}^{cri} = -0.1$	0.844/2.180	0.7	25.89	52.2/16.5	62.3	39.6/38.4	−50.1/23.0	3.013	1.87/1.15	88.1/18.7	0.130
16	$c_\Omega = 5$	0.869/2.261	−1.0	25.74	52.3/15.9	63.9	43.1/38.1	−51.8/22.9	3.052	1.94/1.12	89.2/18.4	0.132
17	$k_* = 0.07$	0.827/1.830	3.4	25.91	47.3/16.7	61.8	37.7/39.0	−48.0/23.5	2.984	1.96/1.02	87.3/18.3	0.131
18	$\hat{A}_s^{ocn}\|_{\Omega=0} = 0.08$	0.831/1.873	6.2	25.63	44.9/16.6	60.2	35.0/38.9	−44.8/23.1	2.991	2.02/0.97	87.4/17.6	0.124
19	$\hat{A}_s^{lnd}\|_{\Omega=0} = 0.06$	0.867/1.999	2.1	25.88	49.0/16.3	61.9	39.0/38.3	−48.7/23.1	3.003	1.94/1.06	87.8/18.6	0.133
20	$R_o\|_{\Omega=0} = 200$	0.869/2.122	2.0	25.92	47.4/16.8	62.8	40.0/38.9	−49.1/23.4	3.014	1.99/1.02	88.1/18.3	0.134
21	$R_o\|_{\Omega=1} = 1000(ocn)/ 2000(lnd)$	0.833/2.020	0.7	25.72	52.8/16.3	61.5	38.9/37.9	−49.5/22.3	3.014	1.86/1.15	88.1/18.9	0.129
22	$\sigma_R\|_{\Omega=0} = \sigma_R\|_{\Omega=1} = 100$	0.846/2.060	2.1	25.92	47.4/16.8	62.8	39.8/39.0	−49.1/23.5	3.008	1.98/1.03	87.9/18.4	0.133
23	$\gamma = 1.5$	0.841/1.955	0.9	25.76	52.8/16.3	61.9	39.0/38.2	−49.6/22.7	3.000	1.86/1.14	87.7/18.9	0.131
24	$\hat{q}_{c,crit} = 7 \times 10^{-4}$	0.856/2.051	−0.3	26.17	54.0/17.5	63.9	41.0/39.3	−52.4/24.2	2.997	1.88/1.12	87.7/18.3	0.136
25	$c_{at} = 1 \times 10^{-3}$	0.855/2.019	4.1	25.49	44.4/16.1	61.5	38.3/38.6	−46.4/22.8	3.006	2.02/0.98	87.9/18.6	0.129
26	$k_{e,R} = k_{e,S} = 1 \times 10^{-5}$	0.875/2.257	−1.0	25.39	54.0/15.1	62.2	41.1/36.9	−50.8/21.9	3.079	1.84/1.24	90.0/18.1	0.131
27	$\eta = 0.5$	0.966/2.425	−2.6	27.50	60.0/16.9	64.3	42.1/39.0	−55.2/24.1	3.002	1.73/1.27	87.8/18.4	0.139
28	$\hat{r}_i = 5$	0.841/2.024	−0.3	25.81	55.6/16.5	62.3	39.2/38.7	−51.5/23.4	2.998	1.95/1.05	87.7/18.4	0.132
29	$\hat{r}_i = 25$	0.906/2.129	1.2	26.56	51.8/29.1	65.3	40.2/42.4	−54.8/28.0	2.912	1.83/1.08	85.1/17.8	0.138
30	$\lambda = 0$	0.880/2.126	9.5	26.08	40.6/17.5	57.9	32.3/39.6	−41.0/22.6	2.930	1.88/1.05	85.7/18.2	0.140

TABLE 2. (Continued)

S	Type	Taylor score RMSE/bias	RESTOA (W m^{-2})	WVP (mm)	LWP/IWP (g m^{-2})	CLDTOT (%)	CLDLOW/ HGH (%)	SWCF/LWCF (W m^{-2})	PRECT (mm day^{-1})	PRECC/L (mm day^{-1})	LHF/SHF (W m^{-2})	AOD
31	$\lambda = 1$	0.853/2.127	0.5	25.76	49.6/16.8	62.9	40.7/38.5	−50.7/23.5	3.017	1.98/1.04	88.2/18.5	0.132
32	$\beta = 0$	0.906/2.784	−7.1	25.19	62.4/12.8	64.0	46.8/34.5	−55.5/20.6	3.170	1.49/1.68	92.6/18.6	0.123
33	$k_{e,R} = k_{s,S} = 0$	0.995/2.765	−7.3	24.18	61.5/10.2	62.4	46.5/31.6	−54.5/19.5	3.226	1.27/1.96	94.3/18.0	0.119
34	$k_{e,R,dn} = k_{s,S,dn} = 0$	0.947/2.015	−0.2	24.52	50.8/14.8	62.2	40.5/37.1	−49.7/22.0	3.061	1.93/1.14	89.5/18.5	0.128
35	$\tilde{M}_D$ without precipitation	0.850/2.048	1.8	25.90	49.2/16.6	62.5	39.4/38.8	−49.3/23.3	3.003	1.94/1.06	87.8/18.5	0.133
36	$\mathrm{Adv}(\Omega) = 0$	0.844/1.919	1.8	25.90	49.2/16.4	62.7	39.8/38.9	−49.6/23.5	2.989	1.90/1.09	87.4/18.6	0.135
37	$\Delta\phi_\Omega = \Delta w_\Omega = 0$	0.886/2.510	−6.6	25.35	61.6/14.9	67.4	50.4/36.4	−57.9/22.8	3.107	1.73/1.38	90.8/18.5	0.125
38	$R_o|_{\Omega=1} = R_o|_{\Omega=0}$	0.901/2.521	−3.8	24.95	63.4/12.6	60.1	41.3/33.3	−51.4/19.7	3.068	1.41/1.66	89.7/20.3	0.118
39	$\tilde{\phi}_u = \tilde{\phi}, \tilde{w}_u = 0$	0.844/2.085	2.1	26.01	48.9/16.6	62.5	39.1/39.0	−49.3/23.5	3.027	1.94/1.09	88.5/17.7	0.131
40	$\Omega = 0$	0.962/3.009	−11.2	24.98	70.4/10.6	64.6	49.3/31.9	−59.5/20.2	3.189	1.10/2.09	93.2/19.0	0.118
41	$\epsilon_* = -\delta_* = 0$	0.883/2.283	9.1	26.31	39.4/17.6	60.6	33.5/40.4	−43.4/24.8	2.920	1.97/0.95	85.4/17.8	0.132
42	$c_\xi = 0$	0.834/1.931	0.4	26.19	52.5/16.5	62.7	39.6/39.0	−50.4/24.0	2.954	1.90/1.06	86.4/18.0	0.180
43	$\hat{A}_s|_{\Omega=0} = 0$	1.229/4.141	−30.2	25.22	104.6/6.8	80.4	69.3/32.3	−85.1/25.6	3.208	0/3.21	93.8/18.2	0.119
44	$\mathrm{RH}_{cri,low} = 0.87$	0.841/1.970	3.5	25.88	46.9/16.6	61.8	38.1/38.8	−47.5/23.2	2.986	1.93/1.06	87.3/18.6	0.134

suggested the satellite estimates may be biased low, which would remove most of the discrepancy between the observation and the simulations. The differences in the mean PRECT are also projected on the RMSEs against observations (1.20 mm day^{-1} in DJF and 1.60 mm day^{-1} in JJA for UNICON; 1.21 mm day^{-1} in DJF and 1.49 mm day^{-1} in JJA for CAM5); however, UNICON simulates better global correlations (0.94 in DJF and 0.91 in JJA for UNICON; 0.92 in DJF and 0.89 in JJA for CAM5) and a more realistic regional pattern than CAM5. Particularly, the improvement in the monsoon-related precipitation pattern over the western equatorial Pacific and South Asia during JJA is encouraging. Other notable improvements are stronger precipitation south of the equator along the South Pacific convergence zone (SPCZ) in DJF, weaker precipitation over the southern Arabian Peninsula during JJA, no precipitation maxima over the eastern Rocky Mountains in the United States during JJA, and weaker double intertropical convergence zone (ITCZ) along the eastern equatorial Pacific Ocean during DJF (not shown, but similar improvement of the double ITCZ can be seen during March–May (MAM) and in the annual-mean plot). On the other hand, some degradations are weaker precipitation over the central United States during JJA, which seems to be related to a warmer near-surface air temperature (Fig. 12) and larger tropospheric moist static energy there (not shown), and stronger precipitation over India and South Asia in JJA, the eastern equatorial Pacific ITCZ during JJA, and western equatorial Atlantic, which are also related to the biases of SWCF/LWCF there (Fig. 10).

Figure 9 shows the decomposition of simulated PRECT into PRECC and PRECL where PRECT = PRECC + PRECL. In the model, PRECC is generated from cumulus parameterized by the convection schemes, while PRECL is generated from stratus parameterized by the grid-scale stratus macrophysics and microphysics schemes (Park et al. 2014). In the tropical (high latitude) regions, most of the precipitation is convective (stratiform) with a gradual transition between the two regions. In both simulations, global annual-mean PRECL is about half of PRECC at this horizontal resolution of 1.9° latitude $\times$ 2.5° longitude, but UNICON simulates a slightly smaller fraction of PRECC among PRECT ($\Lambda \equiv$ PRECC/PRECT $= 0.65$) than CAM5 ($\Lambda = 0.71$). This fraction decreases as the model horizontal grid becomes finer over both the globe and the tropics (not shown), implying that as the model horizontal grid becomes finer, the fraction of the observed convection system simulated by the subgrid convection scheme (grid-scale advection scheme) decreases (increases).
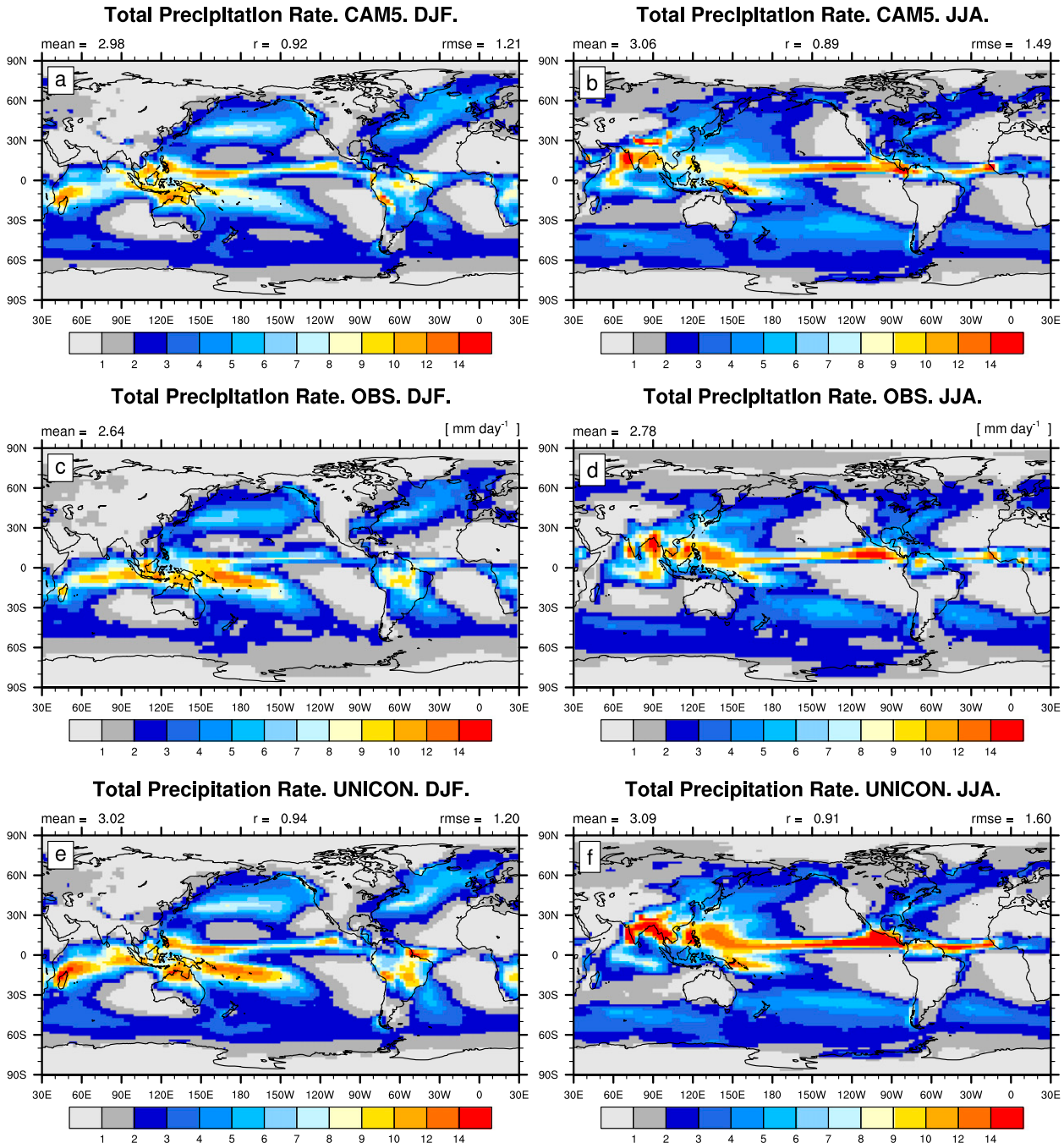
FIG. 8. Total (convective plus stratiform) precipitation rate at the surface (PRECT) during (a),(c),(e) DJF and (b),(d),(f) JJA from (a),(b) CAM5, (c),(d) CMAP observations during 1979–98, and (e),(f) UNICON. The global-mean value is shown at the top-left of each plot. The pattern correlation and RMSE between the simulation and the observation are shown at the top center and the top right of an individual simulation plot, respectively. Similar convention is applied to the following figures.

c. Cloud radiative forcing

Figure 10 shows the annual-mean biases of SWCF and LWCF against the CERES EBAF observation. Compared to CAM5, UNICON shows substantial improvement in simulating SWCF, in terms of RMSE (about 25% reduction from 16.1 to $12.1\,\mathrm{W\,m^{-2}}$), global-mean bias (from -7.5 to $-2.0\,\mathrm{W\,m^{-2}}$), and global pattern correlation (from 0.91 to 0.93). The largest improvement is in tropical deep convection regions, particularly over the far western Pacific and western Indian Oceans including eastern Africa, in which the biases of LWCF are

Convective Precipitation Rate. CAM5. ANN.

mean = 2.12   [mm day^{-1}]

Stratiform Precipitation Rate. CAM5. ANN.

mean = 0.87   [mm day^{-1}]

Convective Precipitation Rate. UNICON. ANN.

mean = 1.95   [mm day^{-1}]

Stratiform Precipitation Rate. UNICON. ANN.

mean = 1.07   [mm day^{-1}]
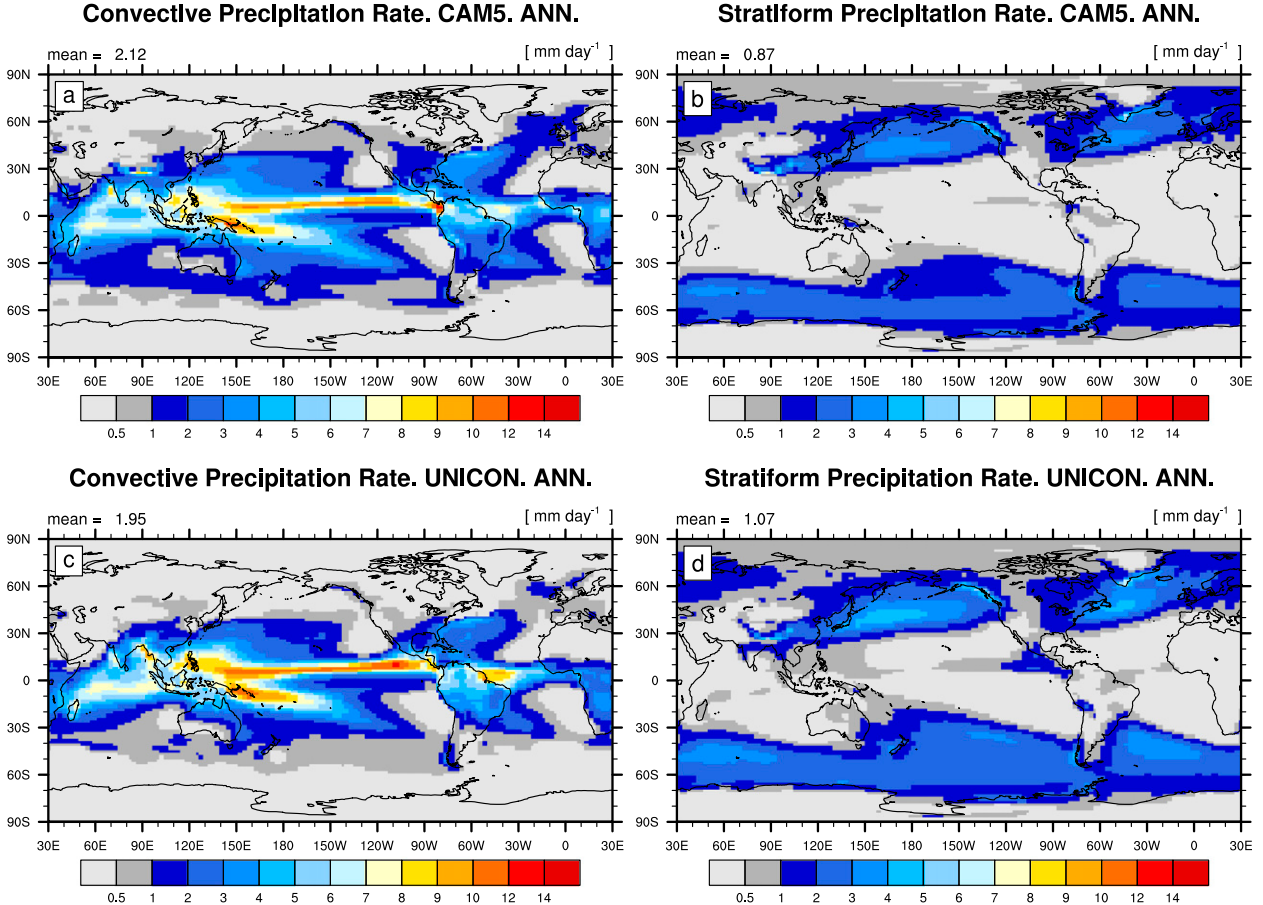
FIG. 9. Annual-mean (a),(c) convective (PRECC) and (b),(d) stratiform (PRECL) precipitation rates at the surface from (a),(b) CAM5 and (c),(d) UNICON.

also reduced. These improvements come in part from a smaller cumulus fraction (Fig. 15) and the treatment of the wet scavenging of in-cumulus aerosols by convective precipitation when cumulus updraft rises [Eq. (39)]. UNICON also improves the simulation of SWCF in the Southern Hemispheric circumpolar region along 60°S and the scatter relationship between SWCF and LWCF over the western Pacific warm pool region (not shown).

Over the eastern subtropical trade wind regimes, however, UNICON still tends to simulate more cloud in the upstream (i.e., negative bias of SWCF) but less cloud in the downstream [i.e., positive (negative) bias of SWCF (LWCF)], implying a rapid downstream transition from stratocumulus to cumulus. As will be discussed in sections 4i and 7, this feature can be improved by reducing the feedback strength of subgrid mesoscale organized flow onto the convective updrafts. Two additional biases that should be improved in the future in UNICON but that also exist in CAM5 are strong negative biases of SWCF over the far eastern equatorial Pacific and Atlantic extending along the SST cold tongue, which are insensitive to changes in UNICON model parameters, and negative (positive) biases of SWCF (LWCF) over the tropical land areas.

d. SLP and surface wind stress

Figure 11 shows the annual-mean biases of sea level pressure (SLP) and surface wind stress against the NCEP–NCAR reanalysis (for SLP) and the ERS observation (for surface wind stress). Both simulations produce a similar bias pattern in SLP with negative biases in the tropics and positive biases in the midlatitude and Arctic areas, with a slightly improved RMSE score in UNICON. For a long time, CAMs have suffered from the positive SLP bias over the North Pacific during summer, which has an important implication for the coupled atmosphere–ocean system since anomalously strong subtropical highs can enhance the formation of marine stratocumulus clouds (Park et al. 2004) and the positive feedback between stratocumulus and the underlying ocean (Park and Leovy 2004; Park et al. 2005, 2006), leading to negative SST biases in the
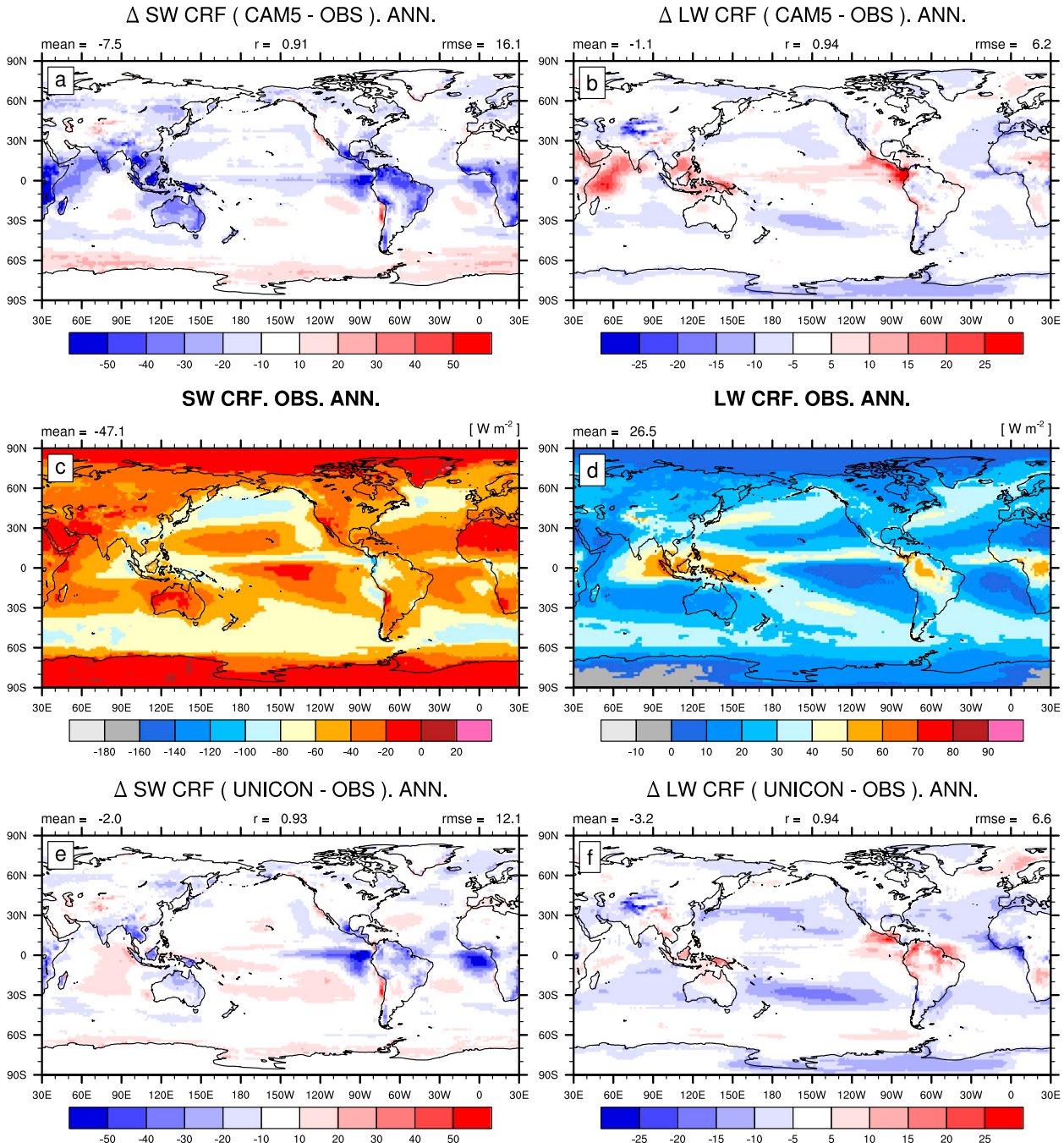
FIG. 10. Annual-mean (a),(c),(e) SWCF and (b),(d),(f) LWCF from (c),(d) the CERES EBAF observations during March 2000–February 2010 and the biases against observations from (a),(b) CAM5 and (e),(f) UNICON.

coupled system (Park et al. 2014). Unfortunately, these SLP biases over the North Pacific still persist in the UNICON simulation, although slightly better than in CAM5. Further research is necessary to reduce these SLP biases.

Overall, UNICON produces similar biases of surface wind stress to CAM5. The notable improvement in the UNICON simulation is the reduction of positive biases in the Southern Hemispheric circumpolar regions where UNICON simulates a weaker cross-latitudinal gradient of anomalous SLP. One notable degradation is the strong positive biases over the Arabian Sea and Bay of Bengal during JJA (not shown), in association with stronger precipitation over the nearby South Asia and
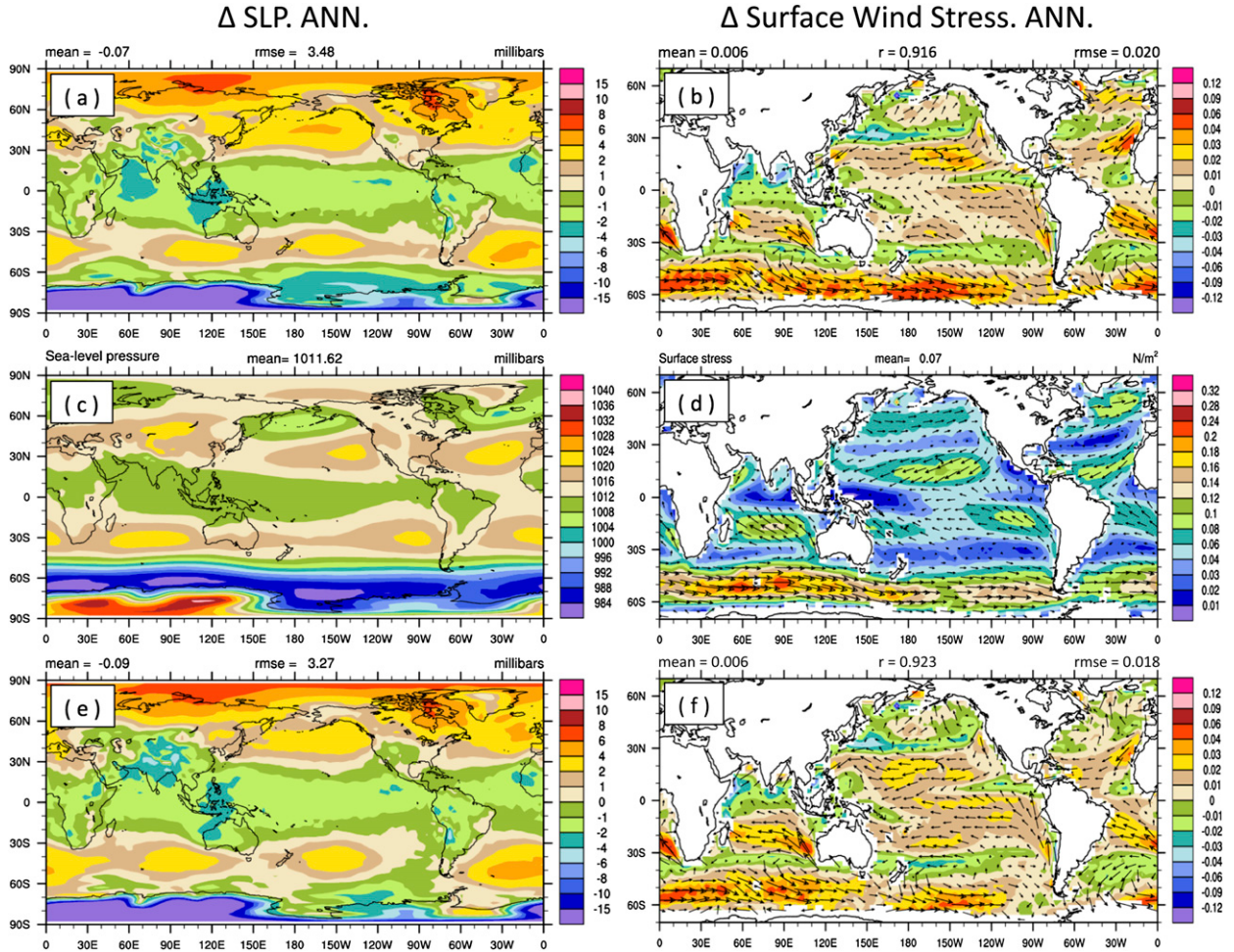
FIG. 11. Annual-mean (a),(c),(e) SLP and (b),(d),(f) surface wind stress from (c) the NCEP–NCAR reanalysis during 1979–98 and (d) the ERS scatterometer observation during 1992–2000 and the biases against observations from (a),(b) CAM5 and (e),(f) UNICON.

Indian continental area (Fig. 8f). We note that over the equatorial Pacific, UNICON simulates slightly stronger wind stress biases than CAM5, as reflected in the degraded RMSE in the Taylor diagram (the variable 6 in Fig. 7). However, UNICON simulates better surface wind stresses than CAM5 when the analysis domain is extended to the entire globe.

e. Near-surface air temperature over land

Figure 12 shows the biases of near-surface air temperature at a height of 2 m against the Willmott observation during DJF and JJA. During DJF, UNICON simulates similar biases of surface air temperature to CAM5. During JJA, however, UNICON simulates warmer surface air temperature than CAM5 and observations over the northern continents, with the largest biases over 8 K in the central United States, which seems to be associated with the negative biases of total precipitation rate (Fig. 8f) and the positive biases of water vapor specific

humidity and temperature in the troposphere (not shown). Sensitivity simulations indicate that these biases tend to be reduced as the simulated convection becomes more shallow with reduced production of convective precipitation (i.e., less convective organization), with the smallest positive biases (1–4 K) when UNICON is turned off. We speculate that advanced convective microphysics reflecting larger aerosol concentration over land is required to reduce these biases and some nonconvective processes also contribute to these biases. A sensitivity simulation without turbulent mountain stress (so that surface wind speed is enhanced) reduces the RMSE of the near-surface air temperature over 15% during JJA in both simulations (not shown). Improving the simulation of convection over summer continents and interactions with other components (despite the successful simulation of the diurnal cycle of precipitation as will be shown in section 5) is one of the future improvements necessary.
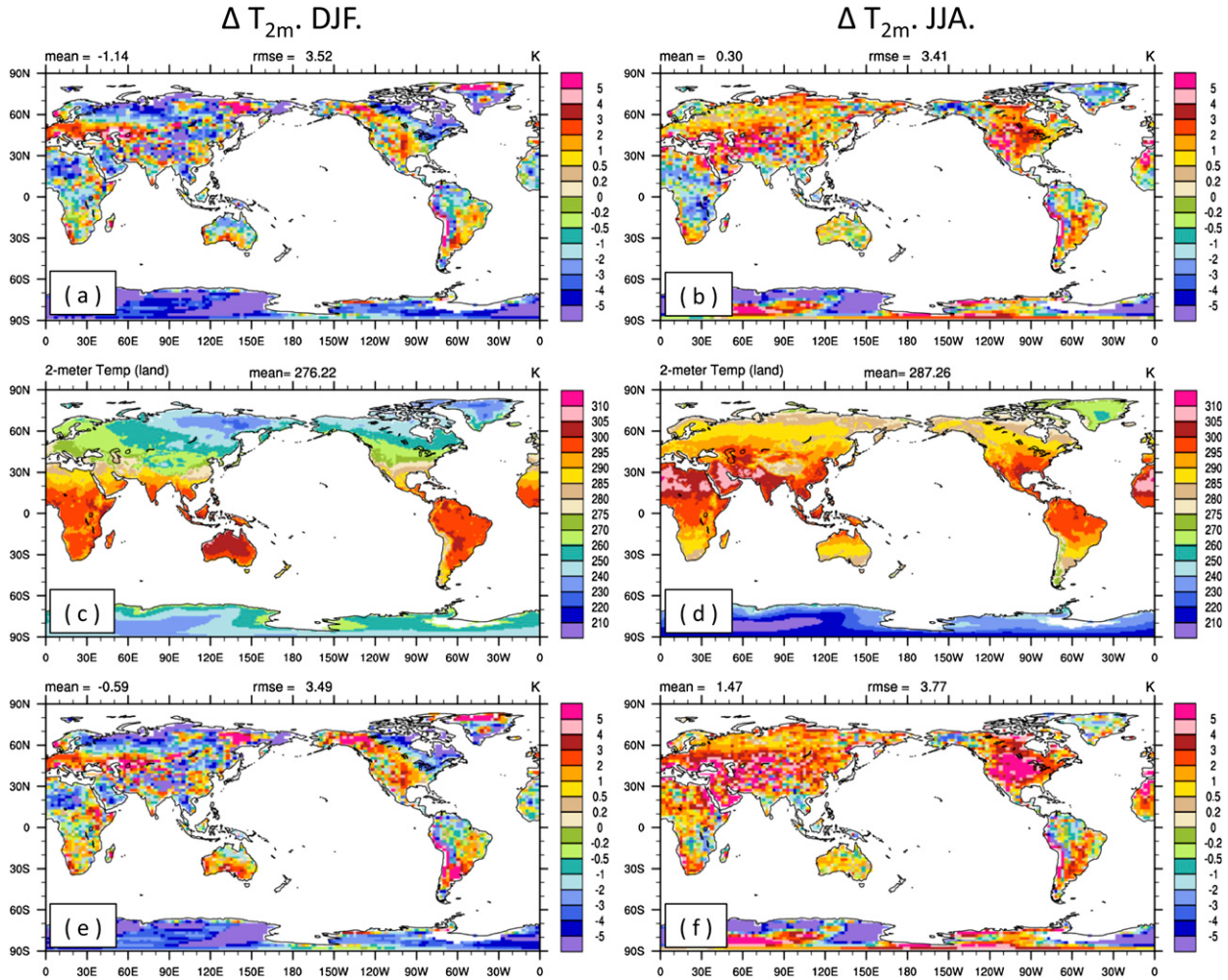
FIG. 12. Near-surface air temperature at a height of 2 m during (a),(c),(e) DJF and (b),(d),(f) JJA from (c),(d) the Willmott observation during 1950–99 and the biases against observations from (a),(b) CAM5 and (e),(f) UNICON.

f. Aerosol optical depth

Figure 13 shows the annual-mean AOD from CAM5, UNICON, and the multisatellites' composite observations (Kinne et al. 2006) and the differences between them. Global annual-mean AODs are similar (0.132 for UNICON and 0.136 for CAM5) but UNICON simulates better spatial correlation (0.84 for UNICON and 0.77 for CAM5) and RMSE (0.08 for UNICON and 0.09 for CAM5) than CAM5. These improvements are concentrated in the tropical and subtropical regions: ΔAOD between UNICON and CAM5 shown in Fig. 13d is almost opposite to the biases of CAM5-simulated AOD shown in Fig. 13b. Compared with CAM5, UNICON simulates more AOD in the tropical deep convection regions and less AOD in the shallow convection regions in the trade wind. In the model, spatial and temporal variations of AOD are controlled by various processes:

emission, subgrid vertical transport by PBL and convection schemes, grid-mean transport, wet and dry deposition, and conversion between various aerosol species. In terms of convective transport of aerosols, two notable differences exist between UNICON and CAM5: in contrast to CAM5 convection schemes, UNICON parameterizes the reduction of in-cumulus aerosol concentration by precipitation production within convective updraft [Eq. (39)], which reduces the aerosol concentration of detrained updraft air, and the cumulus fractional area simulated by UNICON is much smaller than CAM5 (Fig. 15). Since the parameterized wet deposition rate of environmental aerosols by convective precipitation is roughly proportional to the cumulus fractional area in both simulations (Park et al. 2014), the latter seems to be the dominant contribution to the enhanced AOD in the tropical deep convection regions in UNICON.
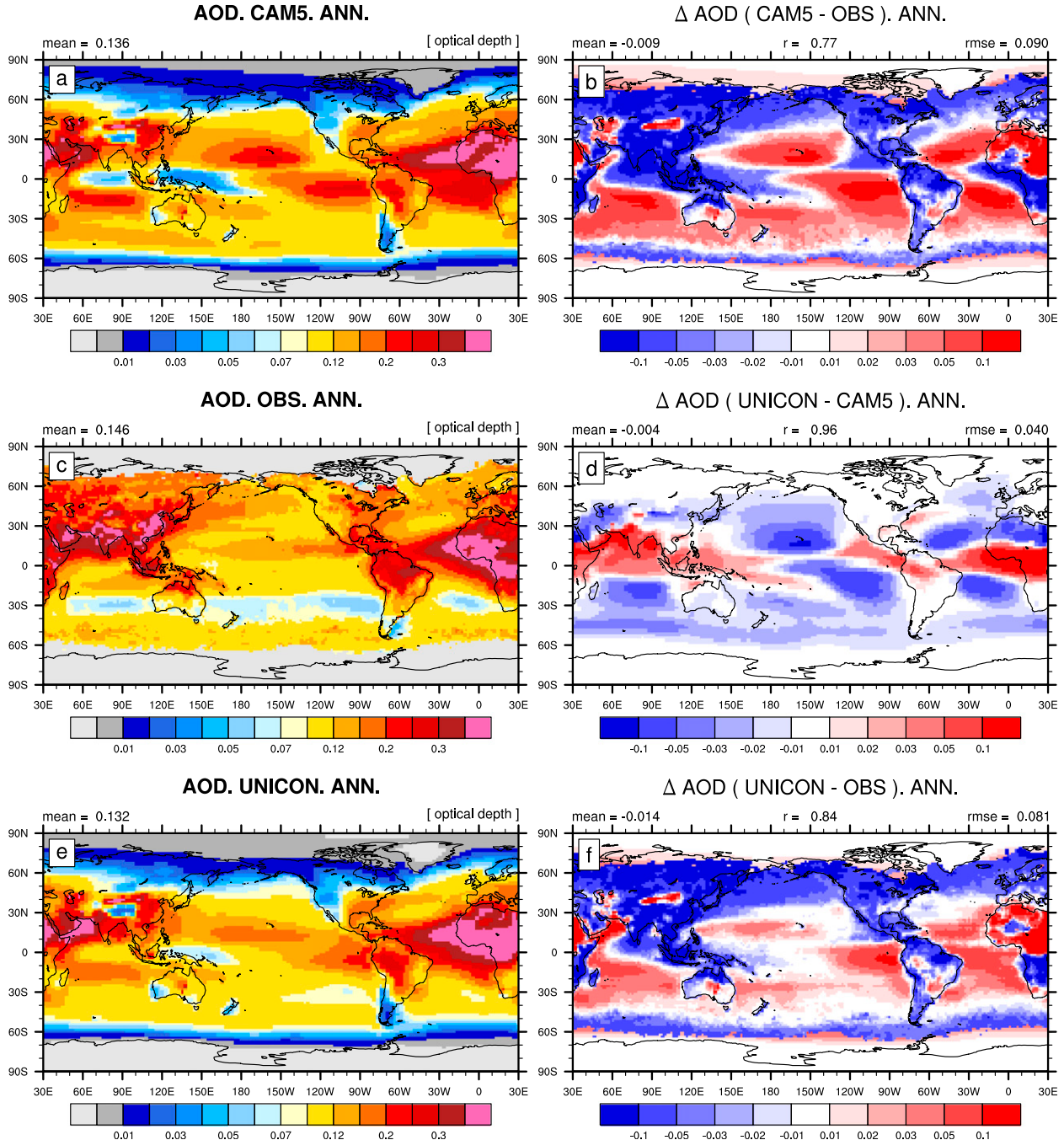
FIG. 13. (left) Annual-mean AOD from (a) CAM5, (c) the multisatellites composite observation, and (e) UNICON. (right) Biases against the observation from (b) CAM5 and (f) UNICON and (d) the difference between UNICON and CAM5.

While UNICON reduces the AOD biases in the tropical and subtropical regions, substantial biases still exist in the extratropical regions both in CAM5 and UNICON. For example, over the midlatitude western North Pacific, both simulations fail to capture the observed zonal band of maximum AOD of over 0.15. It is speculated that overproduction of stratiform precipitation and associated

wet deposition of aerosols are responsible for these negative biases. Future work is required to improve the simulation of global AOD.

g. Zonal-mean cross section

Figure 14 shows the biases of annual zonal-mean cross sections of relative humidity (ΔRH), water vapor specific
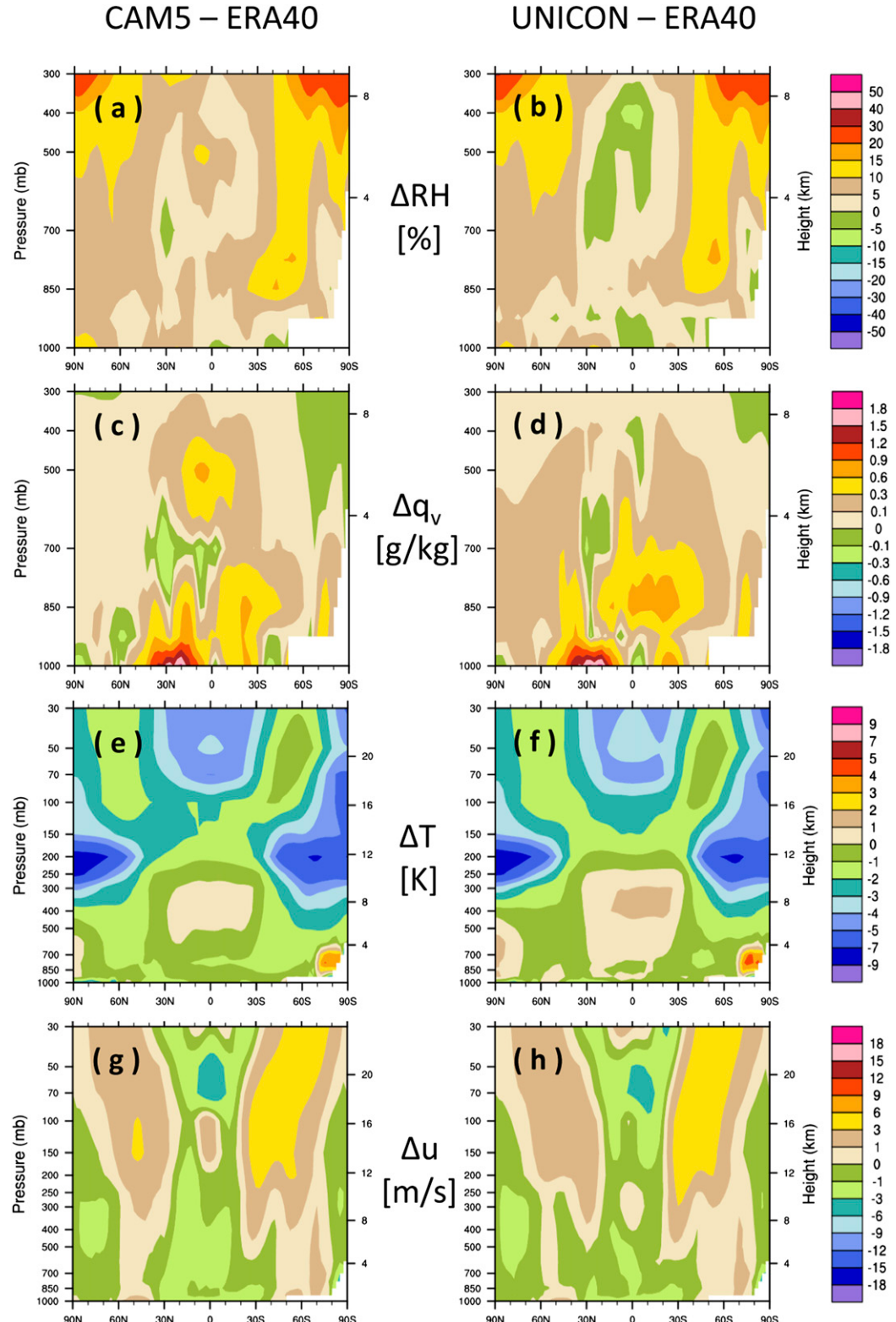
FIG. 14. The biases of annual zonal-mean cross sections of (a),(b) relative humidity (ΔRH), (c),(d) water vapor specific humidity Δq_v, (e),(f) temperature ΔT, and (g),(h) zonal wind Δu against the ERA-40 during 1980–2001 from (a),(c),(e),(g) CAM5 and (b),(d),(f),(h) UNICON.

humidity Δq_v, temperature ΔT, and zonal wind Δu against the ERA-40 from CAM5 and UNICON. Overall, UNICON shows slightly improved simulation: in the troposphere below 300 hPa, UNICON simulates larger cross-sectional areas with small biases of $|\Delta RH| < 5\%$, $|\Delta T| < 1$ K, or $|\Delta u| < 1$ m s^{-1} than CAM5. A couple of notable improvements in the UNICON simulation are the reduction of positive biases of RH and q_v in the tropical upper troposphere centered around 500 hPa and the reduction of zonal wind biases in the tropical troposphere. A degradation of note is the enhancement of positive q_v biases centered around 850 (hPa) in the tropical and Southern Hemispheric subtropical regions. Persisting biases both in CAM5 and UNICON are higher RH and cold biases in the polar upper troposphere extending down into the midtroposphere, too-high q_v within the PBL in the subtropical Northern Hemisphere that exists throughout the year, cold biases and weaker zonal wind in the tropical stratosphere, and anomalously warm air in the far Southern Hemispheric lower troposphere during JJA. These biases also exist in the comparisons against different reanalysis products (e.g., ERA-Interim and JRA-25).

The analysis of vertical profiles of moist static energy (MSE), q_v, and T showed that unlike UNICON, CAM5 has an unrealistic kink of MSE and q_v at around 500 hPa over most of the tropical sites (e.g., Diego Garcia and Truk–Yap–Marshall Islands) that is also projected into the zonal-mean cross section in Fig. 14c (not shown). We also note that over the Great Plains in the United States during JJA, both simulations produce positive biases of MSE, q_v, and T in the troposphere that extend down to surface (Fig. 12).

h. Cumulus fraction and in-cumulus condensate

Figure 15 shows annual–zonal mean cross sections of in-cumulus LWC, in-cumulus ice water content (IWC), grid-mean cumulus LWC, and grid-mean cumulus IWC from CAM5 and UNICON, with cumulus fraction overlaid as a black solid line from each simulation. The most distinct difference between the two simulations is that UNICON simulates smaller cumulus fraction (contour intervals of CAM5 and UNICON are 0.02 and 0.002, respectively) but larger in-cumulus condensate than CAM5. The UNICON-simulated annual zonal-mean cumulus fraction is less than 1.5% in the entire cross-sectional domain, while the CAM5-simulated cumulus fraction is larger than 10% in the tropical troposphere. In the subtropical and midlatitude regions, CAM5 simulates a maximum in-cumulus LWC/IWC of around 0.4 g kg^{-1} by the shallow convection scheme, but in the tropical regions, the maximum in-cumulus condensate simulated by the deep convection scheme is
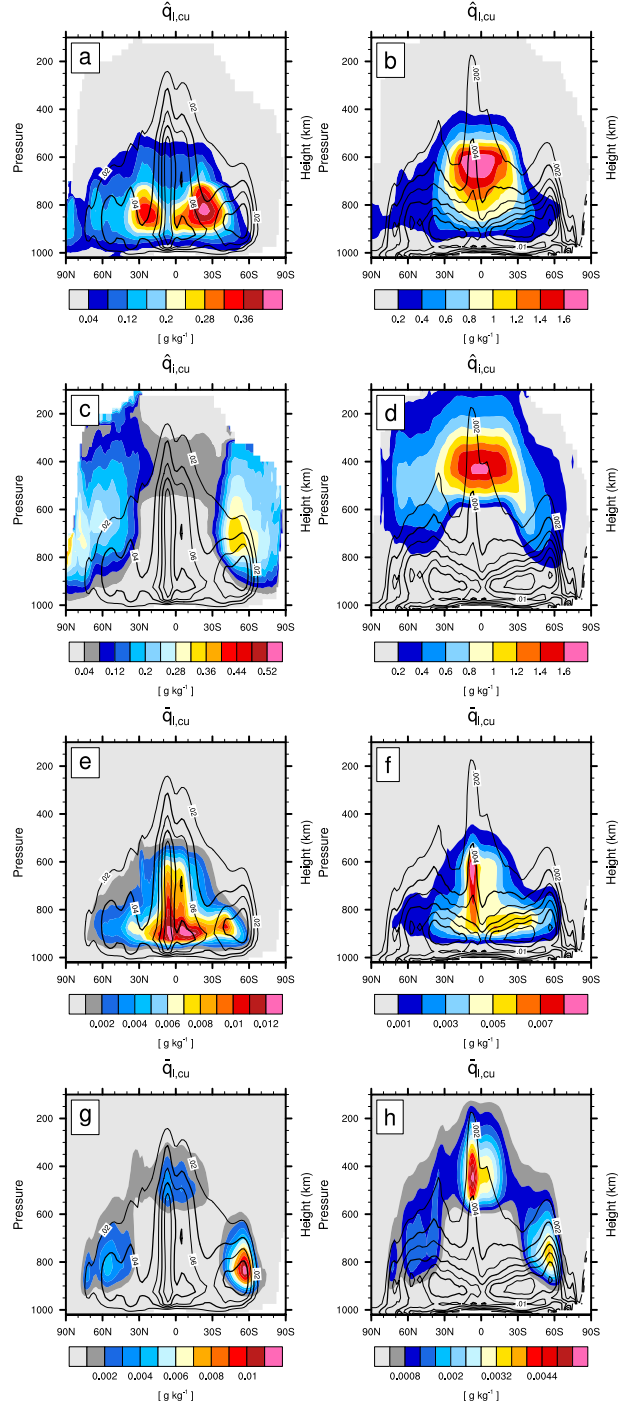

FIG. 15. Annual zonal-mean cross sections of (a),(b) in-cumulus LWC $\hat{q}_{l,cu}$, (c),(d) in-cumulus IWC $\hat{q}_{i,cu}$, (e),(f) grid-mean cumulus LWC $\bar{q}_{l,cu}$, and (g),(h) grid-mean cumulus IWC $\bar{q}_{i,cu}$ from (a),(c),(e),(g) CAM5 and (b),(d),(f),(h) UNICON. In each panel, convective updraft fractional area is denoted by a solid line with different intervals between CAM5 (contour interval is 0.02) and UNICON (contour interval is 0.002).

less than $0.1\,\mathrm{g\,kg^{-1}}$ in the middle and upper troposphere—about one order of magnitude smaller than the typically observed value (Prabha et al. 2011). On the other hand, UNICON simulates a maximum in-cumulus LWC/IWC of $1.7\,\mathrm{g\,kg^{-1}}$, which is more comparable to the observations than CAM5. The patterns of grid-mean cumulus condensate—a product of cumulus fraction and in-cumulus condensate—are similar between the two simulations; however, CAM5 simulates more than UNICON. UNICON tends to simulate deeper cumulus than CAM5 in the tropics (Figs. 15g,h).

In CAM5, deep cumulus fraction is a simple function of deep convective mass flux [i.e., $\hat{a} = 0.1\ln(1 + 500\hat{M})$; Park et al. 2014], which is not a physically based but an empirical formula (note that UNICON uses $\rho\hat{a} = \hat{M}/\hat{w}$, where ρ is the air density, and $\hat{a}$, $\hat{w}$, and $\hat{M}$ are the fractional area, vertical velocity, and the mass flux of the convective updraft plume, respectively), overestimating the real deep cumulus fraction due to the inclusion of stratus fraction generated from the detrained convective condensate in its empirical derivation. Two direct consequences of smaller cumulus fraction in UNICON are the decrease of radiative impact of cumulus and associated SWCF/LWCF (Fig. 10) and the decrease of wet deposition of aerosols by convective precipitation and the resulting increase of AOD in the tropical deep convection regions (Fig. 13d).

i. Stratocumulus-to-cumulus transition

Figure 16 shows cross sections of grid-mean potential temperature $\overline{\theta}$ and stratus properties (A_{st} is the stratus fraction and $\overline{q}_{l,\mathrm{st}}$ is the grid-mean stratus LWC) and the grid-mean subsidence rate $\overline{\omega}$ and cumulus properties (A_{cu} is the cumulus fraction and $\overline{q}_{l,\mathrm{cu}}$ is the grid-mean cumulus LWC) simulated by CAM5 and UNICON along 20°S from coastal Peru to the SPCZ during September–October (SON). Both CAM5 and UNICON successfully capture the observed transition from stratocumulus to cumulus: near the coast, a well-defined stratocumulus deck is located under the stably stratified free atmosphere with strong grid-mean subsidence; over the open ocean, stratocumulus gradually deepens in response to warmer SST and weaker subsidence, and shallow cumulus develops beneath the stratocumulus; and near the SPCZ, stratocumulus completely dissipates and deep cumulus develops.

Comparing with the observations, Xiao et al. (2014) noted too-rapid downstream dissipation of CAM5 stratocumulus deck in this region, which is improved in the UNICON simulation with the extension of the stratocumulus deck farther to the west (down to 109°W identified by $\overline{q}_{l,\mathrm{st}} = 0.01\,\mathrm{g\,kg^{-1}}$) with a deeper stratocumulus top (800 hPa) than CAM5 (down to 102°W with

a top at 850 hPa). As noted in Park et al. (2014), CAM5 can also simulate a more extended stratocumulus deck by reducing the penetrative entrainment efficiency in the shallow convection scheme. UNICON does not have a separate parameterization for the penetrative entrainment; however, the sum of individual convective updraft and downdraft processes directly simulates the penetrative entrainment effects. In UNICON, a further downstream extension of the stratocumulus deck can be simulated by suppressing subgrid mesoscale organized flow via reducing convective precipitation with an increase of the threshold in-cumulus condensate (S.24 in Table 2), reducing the evaporation efficiency of convective precipitation (S.26 in Table 2), or decreasing the mesoscale perturbations of the vertical velocity, thermodynamic scalars, and the radius of convective updraft plumes at the surface (e.g., S.15, 16, 21, and 23 in Table 2 and Figs. 24b,g).

j. Perturbations associated with subgrid mesoscale convective organization

Figure 17 shows the UNICON-simulated annual-mean convective organization Ω [Eq. (72)] and associated perturbations of vertical velocity [Δw_{Ω}; Eq. (74)] and thermodynamic scalars [$\Delta\phi_{\Omega}$ with $\phi = \theta_c, q_t, u, v$; Eq. (73)] in the upflow branch of the mesoscale organized flow within the PBL (see Fig. 5 in Part I), the updraft plume radius at the surface $\hat{R}_{\mathrm{sfc}}$ [Eq. (23)], and the cumulus-top height. UNICON also simulates similar perturbations of the mass and number concentration of individual aerosol species (not shown). When multiplied by $1 - \hat{A}_{\max} = 0.9$, Ω represents the fractional area of the subgrid cold pool within the PBL in each grid box.

The global annual-mean subgrid cold pool area at this horizontal resolution of 1.9° latitude × 2.5° longitude and the associated perturbation of the updraft vertical velocity at the surface are 6.3% and $0.13\,\mathrm{m\,s^{-1}}$, respectively. Spatial patterns of Ω, Δw_{Ω}, $\Delta\theta_{c,\Omega}$, $\hat{R}_{\mathrm{sfc}}$, and cumulus-top height are quite similar to the pattern of convective precipitation rate at the surface (Fig. 9c). This is an expected result since convective updrafts can grow deeply (so that more convective precipitation is generated) when subgrid flow becomes more organized ($\Omega > 0$), so convective updrafts have stronger vertical velocity ($\Delta w_{\Omega} > 0$) and a greater positive buoyancy perturbation ($\Delta\theta_{c,\Omega} > 0$) with less entrainment dilution ($\hat{R}_{\mathrm{sfc}}(\Omega) > \hat{R}_{\mathrm{sfc}}|_{\Omega=0}$). By construction, $\Delta\theta_{c,\Omega}$ is almost always positive; however, interestingly, $\Delta q_{t,\Omega}$ can be either positive or negative, implying that cold pools can have either smaller or larger q_t than the grid-mean value within the PBL. The global annual-mean $\hat{R}_{\mathrm{sfc}}$ and cumulus-top height are 298 m and 2.4 km, respectively. Maximum $\hat{R}_{\mathrm{sfc}}$ is simulated over the far north of South
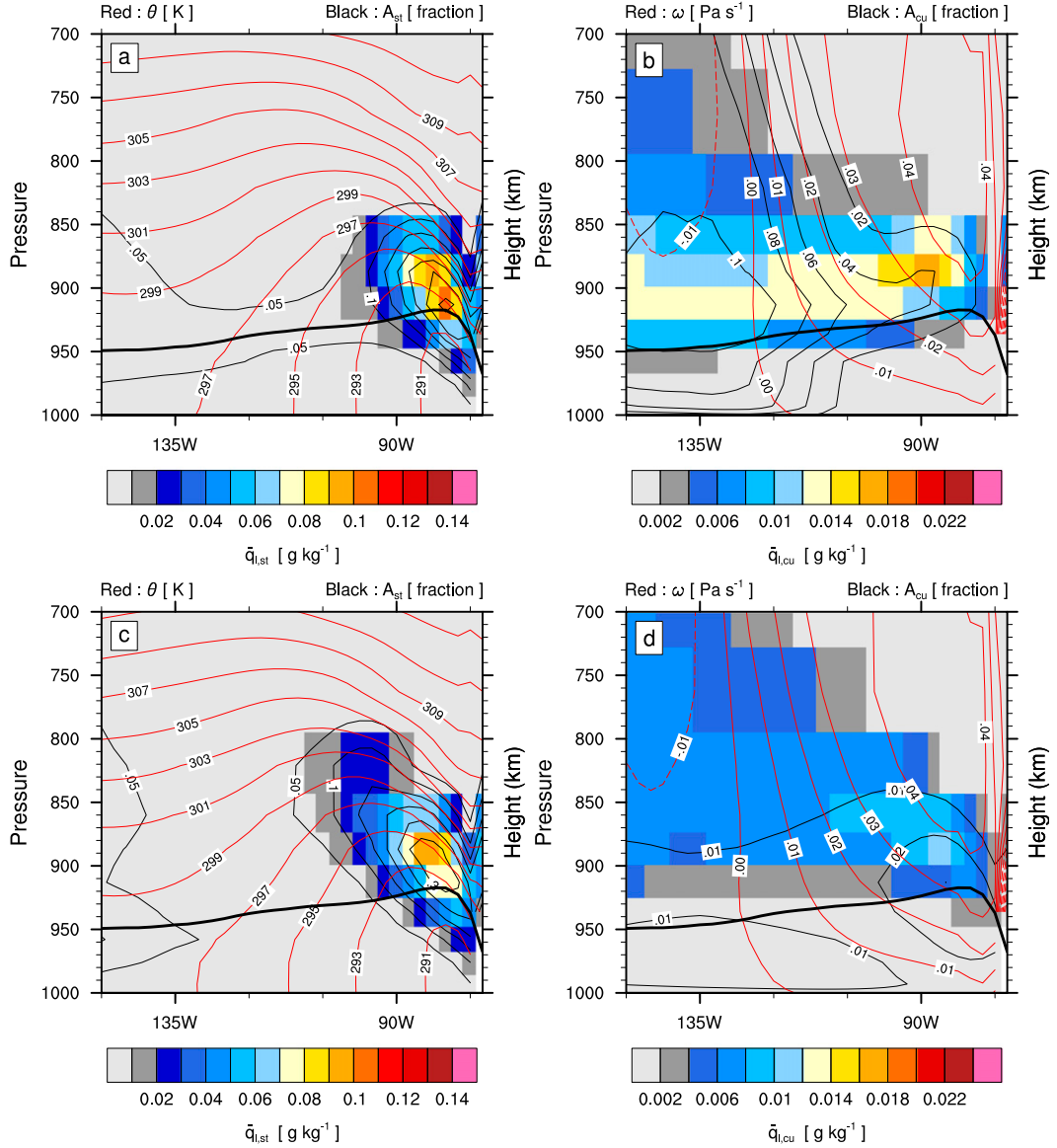
FIG. 16. Vertical cross sections of (a),(c) grid-mean potential temperature $\overline{\theta}$, stratus fraction A_{st}, and grid-mean stratus LWC $\overline{q}_{l,st}$ and (b),(d) grid-mean subsidence rate $\overline{\omega}$, cumulus fraction A_{cu}, and grid-mean cumulus LWC $\overline{q}_{l,cu}$ along 20°S during SON from (a),(b) CAM5 and (c),(d) UNICON. In each panel, a thick, solid black line denotes the simulated PBL height.

America and the Maritime Continents in the western Pacific warm pool region. Cumulus-top height is a minimum over the eastern subtropical ocean where SST is low and strong grid-mean subsidence exists (Fig. 16d) but gradually increases over the open ocean, reaching the maximum height of 7–8 km over the western ITCZ and SPCZ.

5. Diurnal cycle of precipitation

Figure 18 shows the diurnal cycle of surface precipitation from the TRMM satellite observations (3 hourly), CAM5 (1 hourly), and UNICON (1 hourly) during DJF and JJA. Fourier analysis is performed on surface precipitation to compute the amplitude, phase, and the percentage variance explained by various harmonic functions with different periods. In each figure, different colors denote the local hour with maximum surface precipitation fitted to the first harmonic with a period of 24 h (i.e., diurnal cycle), and darker shading denotes a larger amplitude of the diurnal cycle. Over most of the globe, the first harmonic explains more than 80% of the variance, while the variance explained by the second harmonic (semidiurnal cycle) is less than 20%
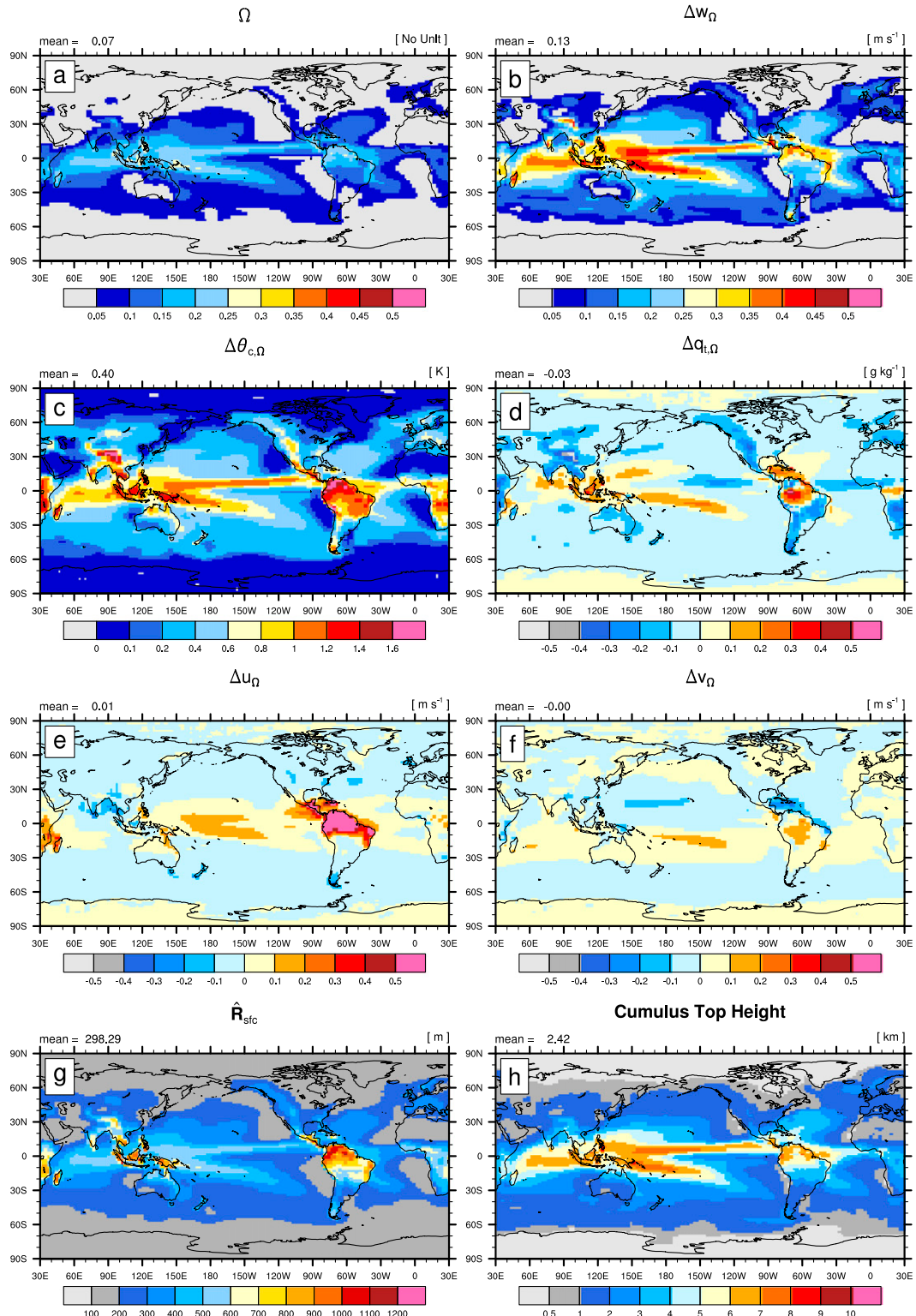
FIG. 17. Annual-mean statistics in association with subgrid cold pool and mesoscale organized flow simulated by UNICON: (a) convective organization Ω and organization-related perturbations of (b) vertical velocity Δw_Ω, (c) condensate potential temperature $\Delta\theta_{c,\Omega}$, (d) total specific humidity $\Delta q_{t,\Omega}$, (e) zonal wind Δu_Ω, (f) meridional wind Δv_Ω in the upflow branch of the mesoscale organized flow within the PBL, (g) updraft plume radius at the surface $\hat{R}_{sfc}$, and (h) cumulus-top height defined as the height where the updraft vertical velocity is zero (note that the default simulation shown in this paper uses a single updraft plume).
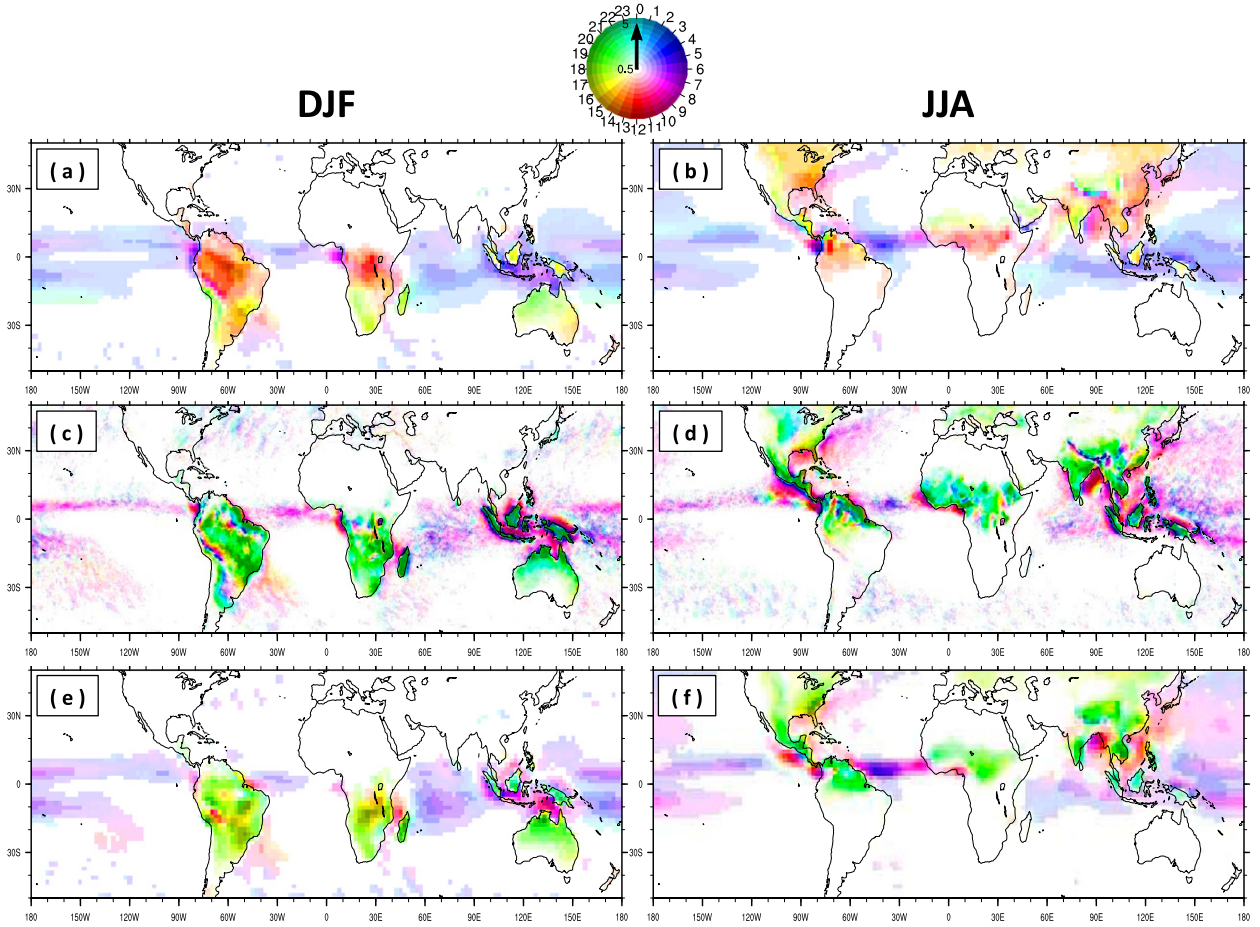
FIG. 18. The diurnal cycle of the total precipitation rate at the surface during (a),(c),(e) DJF and (b),(d),(f) JJA from (c),(d) the TRMM satellite observations during 2000–09, (a),(b) CAM5, and (e),(f) UNICON. The color scale denotes the local hour when the surface precipitation rate fitted to the first harmonic function is a maximum and the hue scale denotes the amplitude of the diurnal cycle.

(not shown). Hereafter, we will focus on the diurnal cycle.

Over the continents during summer, maximum surface precipitation is observed in the late afternoon (green color) except in the vicinity of large mountain areas such as the Himalayas and the Andes. CAM5 simulates the observed diurnal cycle well in some regions (e.g., southern Africa, northern Australia, and the Maritime Continent in the western equatorial Pacific during DJF), but in most of the other regions, CAM5 produces maximum surface precipitation too early. Compared to CAM5, UNICON significantly improves the simulation of the observed phase and amplitude of the diurnal cycle, both over land and ocean. As will be discussed in section 7, this success of UNICON is likely to be a result of its ability to simulate complex feedback processes among convective updrafts, convective downdrafts, and mesoscale organized flows and the interactions between subgrid and grid-scale processes. If any of these feedback chains is shut off, the UNICON-simulated

diurnal cycle of precipitation is substantially degraded (not shown).

A few features that need to be improved in UNICON are the lack of nocturnal maxima of surface precipitation over the central United States during JJA and the weaker amplitude of the diurnal cycle over the Maritime Continent in the western equatorial Pacific during JJA. Since UNICON is a diagnostic plume model with a diagnostic precipitation formulation (i.e., convective updraft plumes rise instantaneously from the surface all the way up to the cumulus top, and convective precipitation generated within cumulus instantaneously falls to the ground), the 1–2-h offset between the simulated and observed diurnal phase of surface precipitation is likely to be inevitable. However, we anticipate that some of the features mentioned above can be improved by raising convective plumes from the PBL top as well as from the surface (i.e., elevated convection) and increasing horizontal resolution.
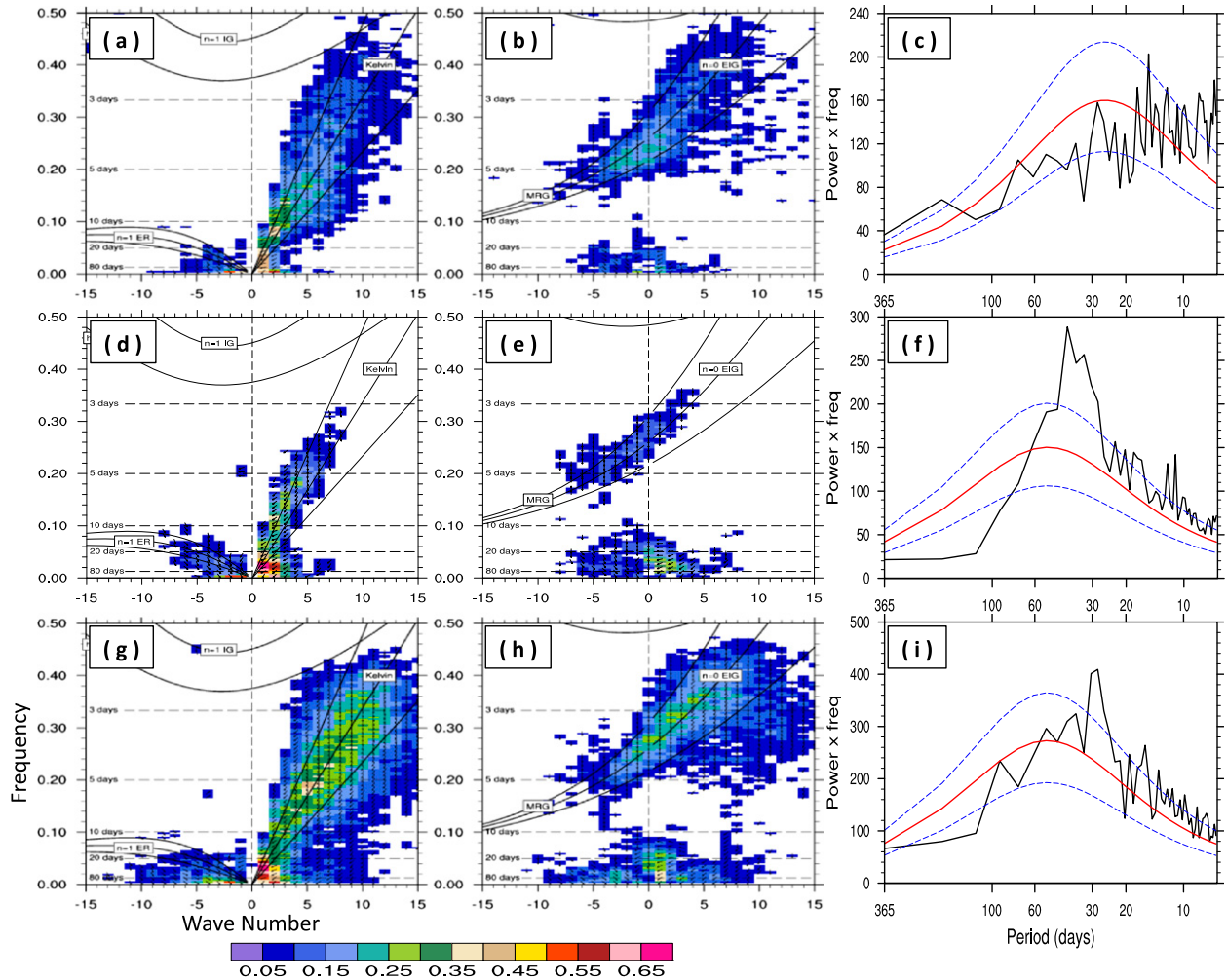
FIG. 19. The (a),(d),(g) symmetric and (b),(e),(h) asymmetric components of coherence squared in wavenumber–frequency space obtained from the cross-spectrum analysis of daily anomalies of OLR and zonal wind at 850 hPa (U850) in the latitude band between 15°S and 15°N during January 1979–December 2005 from (d)–(f) the AVHRR satellite observation and the NCEP–NCAR reanalysis, (a)–(c) CAM5, and (g)–(i) UNICON. The power spectrum of daily OLR anomalies averaged over the Indian Ocean (10°S–5°N, 75°–100°E) is in (c),(f),(i) with the null (red line), 5% (lower blue dotted), and 95% (upper blue dotted) red-noise significance levels.

6. Madden–Julian oscillation

This section compares the simulated and observed MJOs analyzed using the daily anomalies of outgoing longwave radiation (OLR), wind vectors at 850 and 200 hPa (U850, V850, U200, V200), and PRECT. The observed OLR, wind vectors, and PRECT are from the Advanced Very High Resolution Radiometer (AVHRR; Liebmann 1996), the NCEP–NCAR reanalysis, and the GPCP, respectively. The detailed information on the analysis methods used in this paper can be found at http://www.ncl.ucar.edu/Applications/mjoclivar.shtml. Figure 19 shows the symmetric and asymmetric components of the coherence squared between the daily anomalies of OLR and U850 and the

power spectrum of daily OLR anomalies over the Indian Ocean from CAM5, UNICON, and the observations. Observations show the strongest coherency in the MJO regime at a period of 30–80 days and a wavenumber smaller than 3 in both the symmetric and asymmetric components. CAM5 tends to mimic the observed MJO; however, the corresponding covariability is weaker. UNICON improves the simulations with stronger covariability than CAM5, as is also apparent in the power spectrum analysis of daily OLR anomalies over the Indian Ocean that shows significant power peaks above 95% red noise significance level at around 30 days—more similar to the observations than CAM5. The sensitivity simulation of S.6 (see Table 2) slightly shifts the period of the maximum power to a low-frequency

CAM5

OBS

UNICON
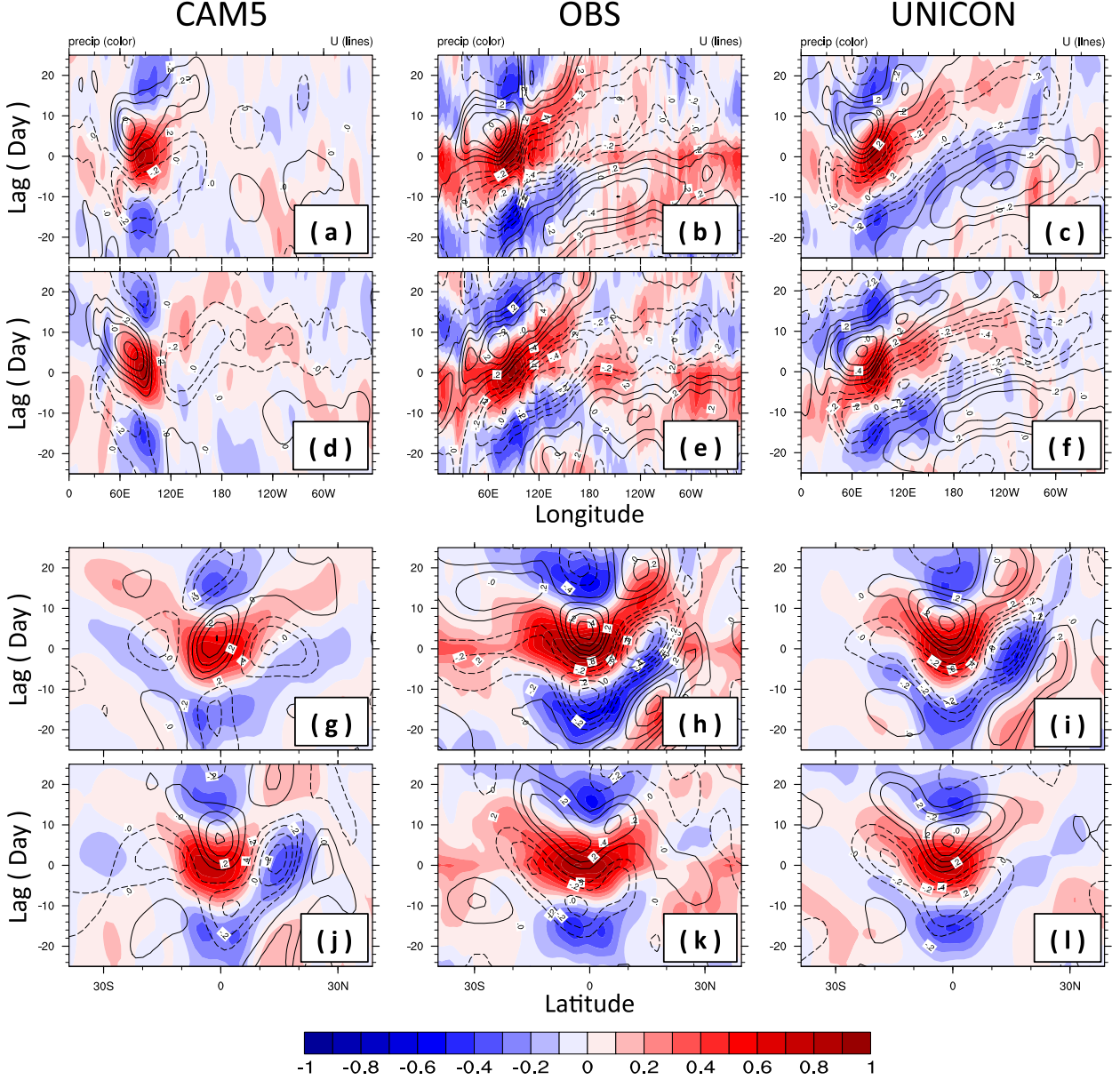
FIG. 20. The lead–lag correlations of 20–100-day bandpass-filtered, daily PRECT (color shading) and U850 (solid dashed line) correlated to the daily time series of bandpass-filtered PRECT at (0°, 90°E) as a function of (a)–(f) longitude and (g)–(l) latitude during (a)–(c),(g)–(i) May–October and (d)–(f),(j)–(l) November–April from (center) the GPCP PRECT and the NCEP–NCAR reanalysis of U850 during January 1996–December 2008, (left) CAM5, and (right) UNICON.

regime, simulating the significant power peaks at a period of 25–45 days, improving the default simulation (not shown).

The success of UNICON in simulating the MJO can also be seen in the lead–lag correlation analysis of 20–100-day bandpass-filtered, daily PRECT and U850 (Fig. 20), in which UNICON simulates the realistic eastward- and northward-propagating waves much better than CAM5, particularly in terms of the eastward propagation; the wavenumber–frequency spectra of daily anomalies of OLR and U850 (Fig. 21), in which the pronounced power simulated by CAM5 is located outside of the MJO period of 30–80 days, while UNICON correctly simulates the maximum power in the MJO period, although the power is somewhat stronger than the observation; and the multivariate EOF modes and the composite life cycle of 20–100-day bandpass-filtered, daily anomalies of OLR and the wind vectors at 850 and 200 hPa (Fig. 22), where, in contrast to CAM5, UNICON well reproduces the observed
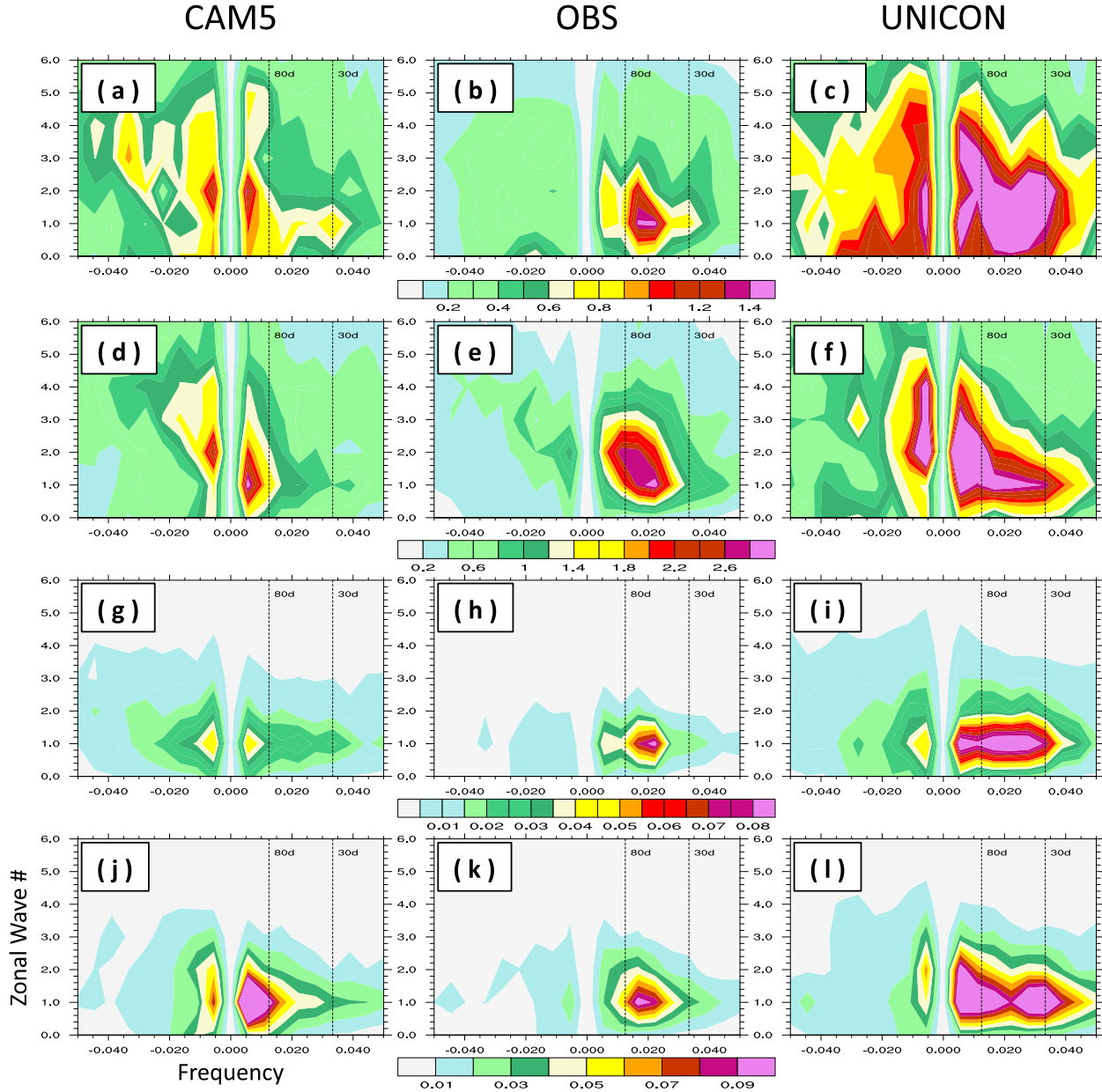
FIG. 21. The wavenumber–frequency spectra of daily anomalies of (a)–(f) OLR and (g)–(l) U850 averaged over the latitude band between 10°S and 10°N during (a)–(c),(g)–(i) May–October and (d)–(f),(j)–(l) November–April for the period of January 1979–December 2005 from (center) the AVHRR satellite observation and the NCEP–NCAR reanalysis, (left) CAM5, and (right) UNICON.

eastward-propagating waves and the spatial EOF patterns with realistic magnitudes of the variance. Some of the differences between the observations and the simulations can be attributed to the lack of coupling with the underlying ocean in the AMIP simulation.

7. Sensitivity to the model parameters

A series of 10-yr stand-alone simulations are performed by perturbing the default values of UNICON

model parameters listed in Table 1. Table 2 summarizes the results, which are grouped into three categories: observations and default simulations (AMIP and 10-yr stand-alone), parameter sensitivity simulations with perturbation of individual parameter values within a plausible range (S.1–S.29), and process sensitivity simulations (S.30–S.44). The process sensitivity simulations consist of extreme parameter values (S.30–S.34, where $k_{e,R,\text{dn}}$ and $k_{e,S,\text{dn}}$ denote the evaporation efficiency of convective rain and snow within convective

CAM5

OBS

UNICON
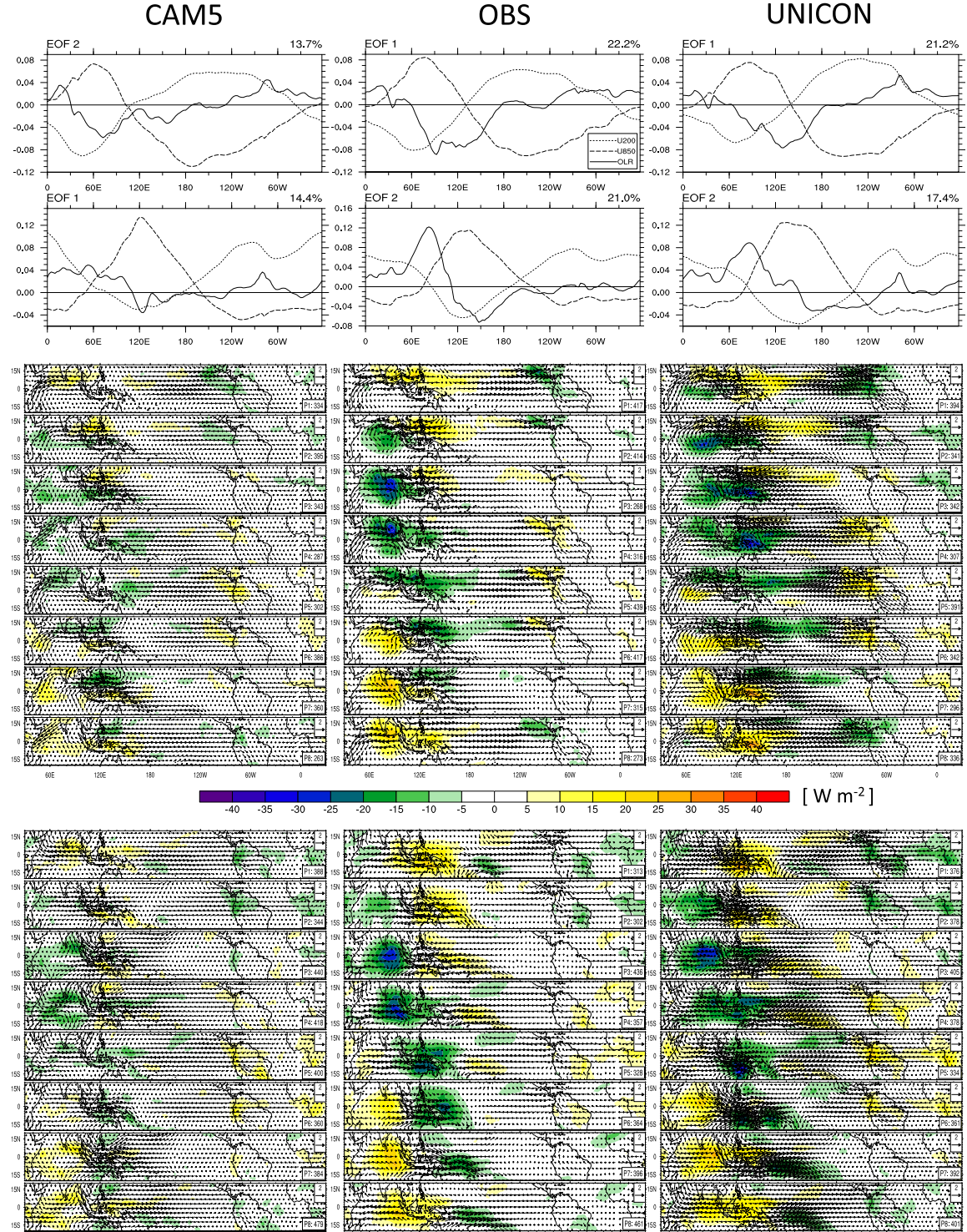
FIG. 22. The composite life cycle of 20–100-day bandpass-filtered, daily anomalies of OLR (color) and wind vectors at 850 hPa during (middle) May–October and (bottom) November–April. The time series corresponding to the first and second EOF modes of the year-round multivariate EOF analysis of (top) OLR, U850, and U200 (with a common legend in the panel of the observed EOF1) are used to derive appropriate categories of the MJO phase for the composite. In each composite plot, the size of the reference anomaly wind vector (m s^{-1}) is in the upper right, and the phase (e.g., P1 means ''Phase 1'') and number of days used to create the composite are at the lower right. The observations are from the AVHRR satellite products for OLR and the NCEP–NCAR reanalysis for wind vectors.

downdrafts, respectively), redefined $\check{M}_D$ without the constraint of nonzero precipitation flux at the PBL top (S.35; see section 2d and appendix C in Part I), neglecting the horizontal advection of Ω and $\Delta\phi_\Omega$ within the PBL [S.36; Eqs. (61)–(64)], neglecting the cold pool–induced perturbation of the vertical velocity and thermodynamic scalars of convective updraft plumes at the surface [S.37; Eqs. (18), (73), and (74)], neglecting the cold pool–induced perturbation of the updraft plume radius at the surface [S.38; Eqs. (23) and (76) and note $\sigma_R|_{\Omega=1} = \sigma_R|_{\Omega=0}$ is already the default], neglecting the cold pool–induced perturbation of the mixing environmental air both within and above the PBL [S.39; Eq. (78)], neglecting the entire feedback of subgrid mesoscale organized flow onto convective updrafts [S.40 = S.36 + S.37 + S.38 + S.39 + $'\Omega = 0'$ in Eq. (75)], neglecting the mixing between the cold pool and the ambient air [S.41; Eqs. (61)–(64)], neglecting the wet deposition of aerosols by convective precipitation within convective updraft [S.42; Eq. (39)], completely turning off UNICON (S.43), and the reduction of stratus fraction by increasing critical RH for the low-level stratus (S.44).

Both CAM5 and UNICON simulate larger WVP and PRECT than the observations. Some parameters have the potential to reduce both WVP and PRECT (e.g., S.18 and 28); however, in order to reduce them to the observed ranges with a reasonable RESTOA, the refinement of the other physics parameterizations and dynamics scheme is also likely to be necessary. Several notable aspects in the sensitivity simulations are, as convection becomes stronger (as $\Lambda \equiv$ PRECC/PRECT increases), LWCF/CLDHGH/IWP and WVP/RESTOA tend to increase but SWCF/CLDLOW/LWP and PRECT/PRECL/LHF tend to decrease (see Fig. 23, where UNICON shows a stronger dependency on Λ than CAM5), implying that strong convection suppresses the formation of stratus and stratiform precipitation by stabilizing the atmospheric column and dries (moistens) the lower (upper) troposphere; the Taylor RMSE score can be improved by increasing k_* (S.17) or $\hat{A}_s^{ocn}|_{\Omega=0}$ (S.18) or by decreasing R_a (S.6) or $R_o|_{\Omega=1}$ (S.21), all of which except S.21, however, further warm the earth; stronger penetrative entrainment at the cumulus top results in more dissipation of marine stratocumulus clouds (S.30), similar to CAM5 (Park et al. 2014); the evaporation of convective precipitation within the environment and the cold pool has a large impact on the global radiation balance and the hydrological cycle (S.32 and 33); the horizontal advection of Ω and $\Delta\phi_\Omega$ does not have much impact on the global statistics at this horizontal resolution of 1.9° latitude × 2.5° longitude (S.36); the mixing between the cold pool and the

ambient air has a large impact on the global climate (S.41); the wet removal of aerosols within convective updraft by convective precipitation substantially decreases the global AOD (S.42); without convection, the simulated Earth becomes rainier and very cold, mainly owing to the huge increase of CLDLOW/LWP/SWCF with the opposite decrease of CLDHGH/IWP (S.43); and the Earth without organized (or deep) convection experiences similar rainy and cooling effects as the Earth without convection, but with a smaller magnitude (S.40).

Figure 24 shows PRECT during JJA (Figs. 24a,f), the biases of annual-mean SWCF against observation (Figs. 24b,g), the diurnal cycle of PRECT during JJA (Figs. 24c,h), and the MJO diagnostics (Figs. 24d,e,i,j; coherence squared between OLR and U850 and the wavenumber–frequency power spectra of OLR during May–October) from S.37 (left) and S.38 (right) sensitivity simulations. These are designed to understand how the feedback of mesoscale organized flow on convective updrafts influence global climate, both in terms of climatology and variability. Although strengthened in magnitude and slightly degraded in terms of RMSE and the global pattern correlation with observation, the regional patterns of PRECT in both simulations are surprisingly similar to the default simulation shown in Fig. 8f. However, substantial tradeoff occurs between PRECC and PRECL: Λ decreases from 0.65 in the default simulation to 0.56 (S.37) and 0.46 (S.38). Weaker convective activity results in stronger SWCF cooling, particularly over the trade-cumulus regime (Figs. 24b,g), implying that the positive biases of SWCF over the trade cumulus in the default simulation (Fig. 10e) can be fixed by adjusting the feedback strength of mesoscale organized flow on convective updrafts.

The most surprising result is the sensitivity of the diurnal cycle of precipitation and the MJO to the mesoscale feedback. Without any mesoscale perturbations of the vertical velocity, thermodynamic scalars, or the radius of convective updraft plumes at the surface, UNICON fails to reproduce the observed diurnal cycle of precipitation (Figs. 24c,h). Interestingly, however, UNICON manages to reproduce the observed MJO even without the mesoscale perturbations of updraft vertical velocity and thermodynamic scalars at the surface (Figs. 24d,e), although the coherence squared is noisier and OLR power is weaker than the default. Without the mesoscale perturbation of the updraft plume radius, however, UNICON fails to simulate the MJO (Figs. 24i,j). This indicates that the key ingredient for simulating the MJO is to correctly parameterize the gradual change of the dilution rate of convective updraft plumes as convection evolves from shallow to deep
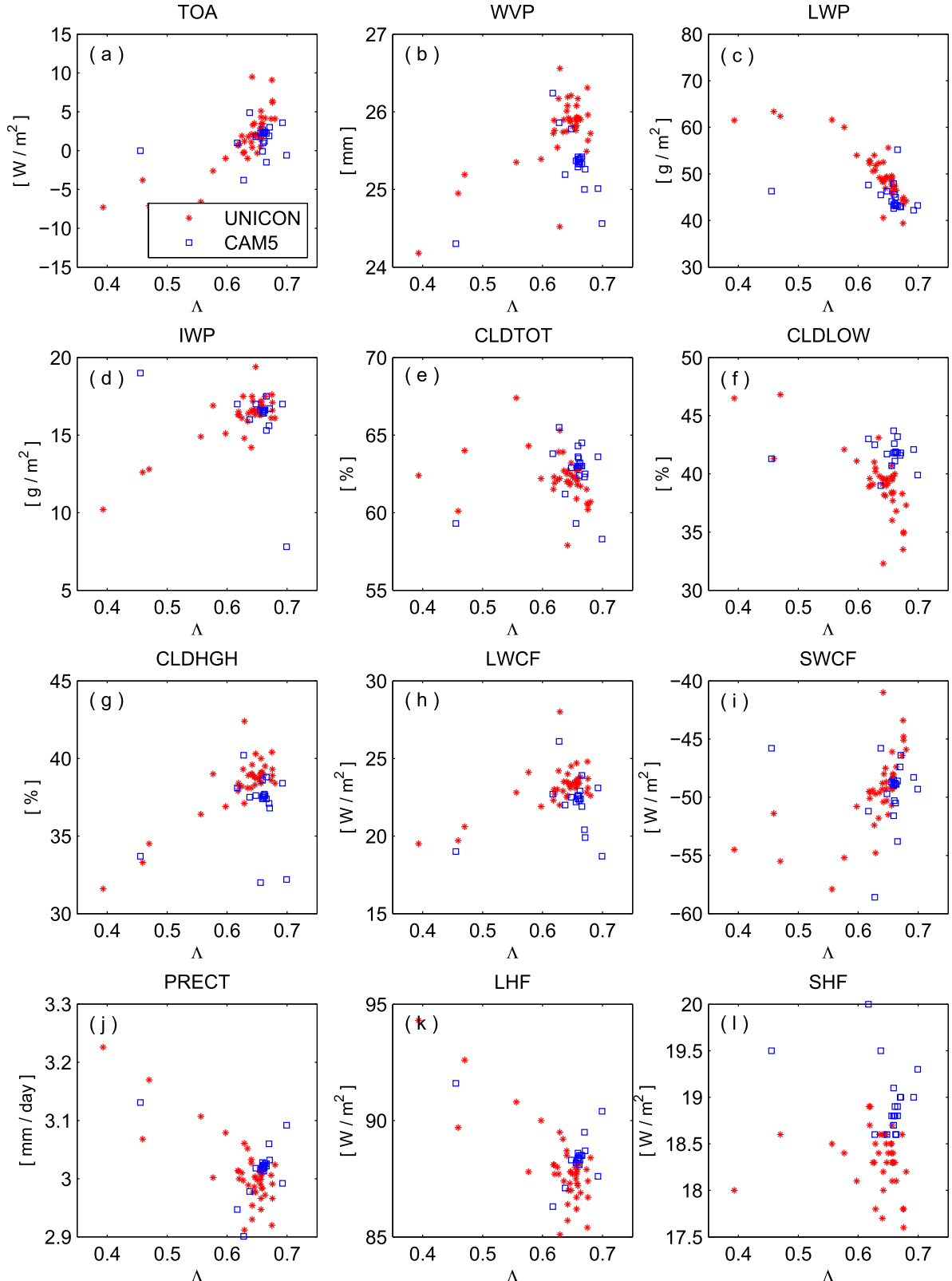
FIG. 23. Scatterplots of various global annual-mean moist variables as a function of Λ = PRECC/PRECT from the sensitivity simulations of UNICON (red; from Table 2) and CAM5 (blue; from Park et al. 2014).
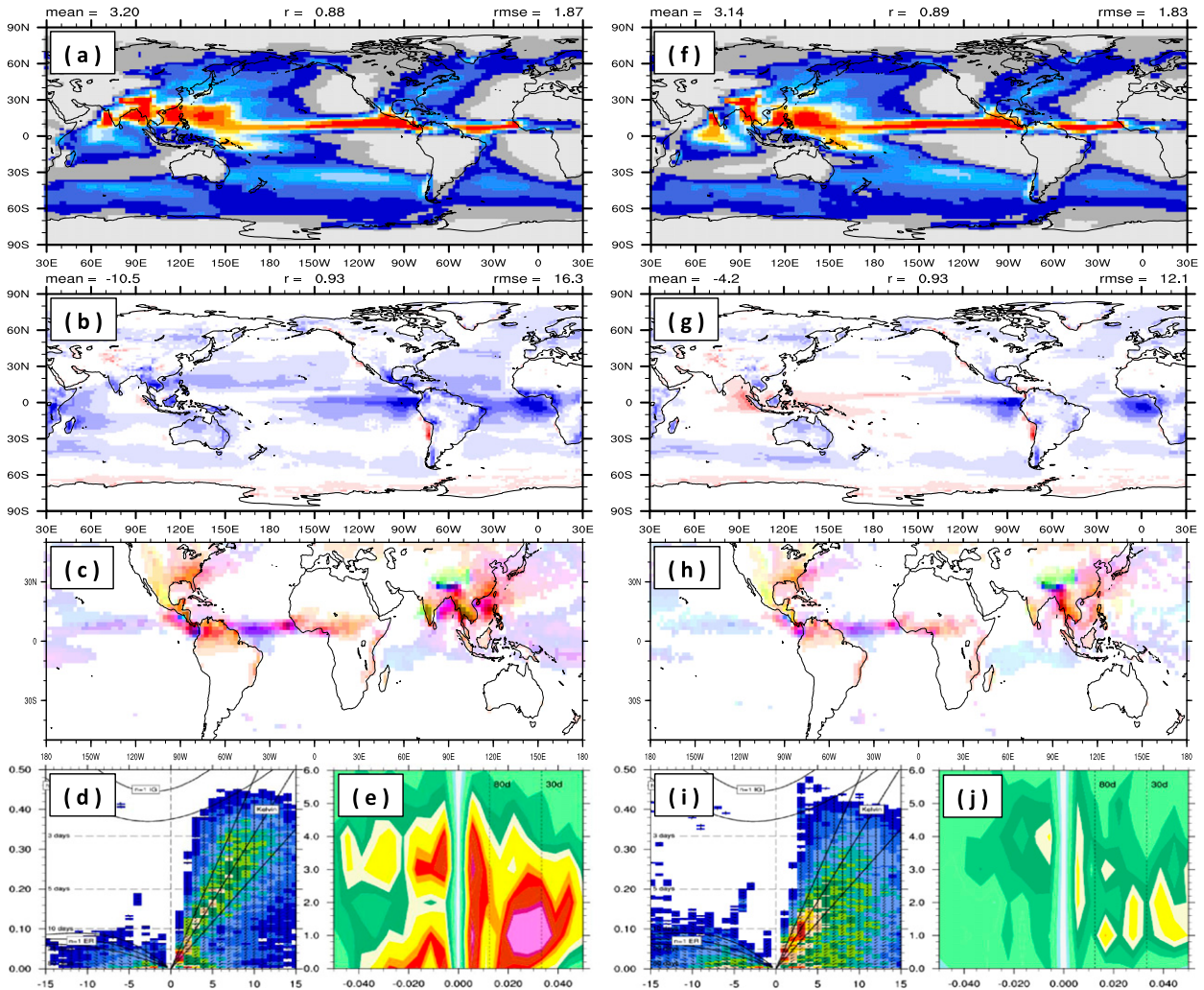
FIG. 24. (a),(f) PRECT during JJA, (b),(g) the biases of annual-mean SWCF against observations, (c),(h) the diurnal cycle of PRECT during JJA, and (bottom) the MJO diagnostics [(d),(i) coherence squared between daily anomalies of OLR and U850 and (e),(j) the wavenumber–frequency spectra of daily anomalies of OLR during May–October] from (left) S.37 and (right) S.38 AMIP sensitivity simulations. The color scales are identical to those shown in the previous figures.

convection and, additionally, mesoscale perturbations of updraft vertical velocity and thermodynamic scalars for the diurnal cycle of precipitation. We note that the mesoscale perturbation of the mixing environmental air (S.39) does not have much impact on the simulated diurnal cycle of precipitation and the MJO, and the amplitude of the diurnal cycle of precipitation increases as the mesoscale organized flow becomes strong (e.g., S.17 in Table 2) (not shown).

Our sensitivity simulations provide a hypothesis on the physical mechanism responsible for the diurnal cycle of precipitation in nature. Over the continents during summer, the surface sensible heat flux reaches its maximum at noon, and convective plumes rise with positive buoyancy. Capped by an inversion barrier at the PBL

top, however, convective plumes with weak vertical velocities and small radii (and so large entrainment dilution) cannot grow deeply but are detrained (i.e., forced convection; Fig. 25a), which moistens the environmental air near the PBL top and fosters subsequent convection to grow deeper into the shallow convection (Fig. 25b) and then into the precipitating moderate convection. In turn, convective precipitation generated by moderate convection forces convective downdraft (which is generated from the mixing between convective updraft and the environmental air) to penetrate into the PBL by evaporative cooling of convective precipitation, leading to the onset of a cold pool and mesoscale organized flow within the PBL (Fig. 25c). This organized flow enhances the cross-sectional size, vertical velocity, and
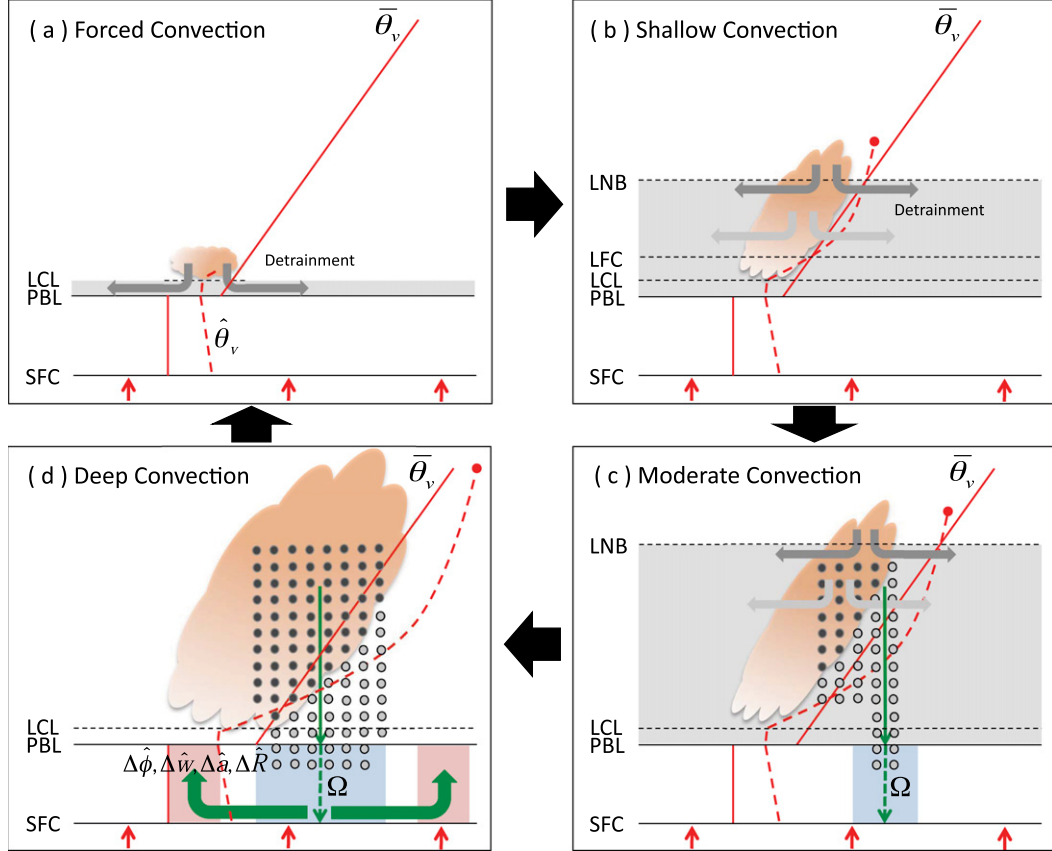
FIG. 25. Schematic diagrams illustrating the life cycle of convection. In each panel, the red arrow at the surface denotes the upward buoyancy flux; the red solid and dashed lines are the grid-mean θ_v and the updraft θ_v, respectively; the gray shading indicates the moistening of the environmental air by convective detrainment denoted by the thick gray arrows; the thin and thick green arrows are the convective downdraft and the mesoscale organized flow, respectively; the blue shading marked by Ω within the PBL is the cold pool and the red shading is the upflow branch of the mesoscale organized flow within the PBL; and $\Delta\hat{\phi}$, $\Delta\hat{w}$, $\Delta\hat{a}$, $\Delta\hat{R}$ denote the mesoscale perturbations of convective updraft properties. SFC: surface, PBL: PBL top, LCL: lifting condensation level, LFC: level of free convection, LNB: level of neutral buoyancy. (a) Forced convection that reaches the LCL but not the LFC, so that it is detrained and moistens environmental air near the PBL top; (b) shallow convection that grows above the LFC but its LNB is not deep, so that no convective precipitation is generated; (c) moderate convection that generates convective precipitation, forces some convective downdrafts to penetrate into the PBL by the evaporation of convective precipitation, and generates the cold pool within the PBL; and (d) deep convection that is forced by the cold pool within the PBL through the feedback of the mesoscale organized flow onto the convective updrafts. Eventually, deep convection decays owing to the stabilization of the atmospheric column by compensating subsidence and radiative cooling and the weakening of the cold pool by surface flux and entrainment at the PBL top.

positive buoyancy of convective updraft plumes at the surface, leading to the gradual development of deep convection to its maximum strength in the late afternoon (Fig. 25d). When mature, however, deep convection strongly stabilizes the atmospheric column by compensating subsidence and radiative cooling, preventing further development of deep convection (i.e., self-regulating convection). Meanwhile, mesoscale organized flow within the PBL is decayed by surface flux and entrainment at the PBL top, which eventually leads to the cessation of deep convection. It is likely that

through these feedback processes among convective updrafts, convective downdrafts and mesoscale organized flows, and the self-regulating impact of subgrid convection on grid-scale stability, UNICON successfully simulates maximum surface precipitation in the late afternoon over the continents during summer. A single-column simulation of the diurnal cycle of convection over land showed a close association between convective precipitation rate at the surface and the mesoscale convective organization (and so the updraft plume radius at the surface) (not shown).

8. Summary and conclusions

The unified convection scheme (UNICON) developed in Part I is implemented into CAM5 and tested in various single-column and global simulations forced by observed SST with interactive land and simplified ice models. UNICON is designed to simulate relative subgrid vertical transport by nonlocal asymmetric turbulent eddies and is well compatible with the CAM5 moist turbulence scheme (which simulates relative subgrid vertical transport by local symmetric turbulent eddies) without double counting. UNICON is a process-based dynamic plume model diagnosing the vertical profiles of the fractional area, plume radius, and number density, as well as the production and evaporation rates of convective precipitation, mass flux, and vertical velocity of multiple convective updraft and downdraft plumes, constructed on the prognosed subgrid cold pool and associated mesoscale organized flow within the PBL. UNICON simulates all dry–moist, forced–free, and shallow–deep convection within a single framework in a seamless, consistent, and unified way, replacing the CAM5 shallow and deep convection schemes. Being designed to simulate subgrid turbulent eddies, not the observed convection, without relying on any equilibrium assumptions (e.g., CAPE closure), UNICON in principle can be applied to any size of GCM horizontal grid (i.e., UNICON is a scale-adaptive convection scheme). As well as for temperature, moisture, and horizontal momentum, UNICON also performs subgrid vertical transport of various aerosol and chemical species with an explicit parameterization of the impact of production (evaporation) of convective precipitation on the tracer concentration within convective updrafts (convective downdrafts and environment).

A set of single-column test simulations showed that UNICON produced similar (for dry convective and stratocumulus-topped PBLs with skill scores of 0.95 and 1.09, respectively) or substantially improved results (for stratocumulus-to-cumulus transition and shallow and deep convection cases with skill scores of 0.36, 0.63, and 0.54, respectively) than CAM5. In the dry convection case, CAM5 simulates unrealistic unstable stratification in the upper PBL, which is corrected by UNICON, due to the countergradient transport by nonlocal asymmetric turbulent eddies. In contrast to the CAM5 shallow and deep convection schemes, UNICON operates in the well-mixed stratocumulus-topped PBL capped by a strong inversion and transports moisture from the lower PBL to the upper PBL. As SST increases, the well-mixed stratocumulus-topped PBL is decoupled, and shallow cumulus develops within the conditionally unstable decoupled layer and helps to sustain the overlying

stratocumulus by detraining convective condensate. The PBL decoupling and stratocumulus-to-cumulus transition simulated by LES are much better reproduced by UNICON than by CAM5. In the shallow convection case, UNICON improves the simulations of updraft plume properties as well as the grid-mean temperature and moisture. Even without convective precipitation, UNICON generates nonnegligible downdraft mass flux through the evaporative cooling during the mixing process. In the deep convection case, convective downdraft forced by the evaporation of convective precipitation generates the cold pool and the mesoscale organized flow within the PBL, which plays a key role in producing strong convective precipitation in the UNICON simulation. The cold pool–induced temperature perturbation of the convective updraft within the PBL is almost always positive, but moisture perturbation can be either positive or negative.

In the global annual mean, UNICON simulates weaker SWCF/LWCF than CAM5 in association with smaller low-level cloud fraction and LWP/IWP but simulates stronger PRECT/LHF. Both CAM5 and UNICON simulate larger WVP and PRECT than the observations. The overall performance of UNICON measured by the mean RMSE of 10 semi-independent thermodynamic variables against the observations is similar to CAM5. The largest improvement is in SWCF; however, the spatial–temporal variability of ocean rainfall and equatorial Pacific surface stress are amplified. Some notable improvements in the UNICON-simulated climatology over CAM5 are seasonal precipitation pattern (e.g., monsoon) over the western equatorial Pacific and South Asia, especially during JJA; a weaker double ITCZ along the eastern equatorial Pacific; reduction of negative SWCF and positive LWCF biases in the tropical deep convection regions; spatial distribution of annual-mean AOD in the tropical and subtropical regions; smaller cumulus fraction and larger in-cumulus LWC/IWC, which contribute to the improved simulation of SWCF/LWCF and the AOD pattern; and stratocumulus-to-cumulus transition along the southeastern Pacific transect during SON. Conversely, some degradations in the UNICON simulations are more global-mean WVP and surface precipitation than CAM5 and observations and warmer near-surface (and tropospheric) air temperature, larger tropospheric moist static energy, and water vapor specific humidity over the central United States during JJA, which are somewhat insensitive to the changes of model parameters.

Along with the climatology, UNICON showed clear improvement in simulating the variability, particularly the diurnal cycle of precipitation and the MJO, both of which have been notoriously difficult to simulate in

GCMs, although some recent models showed improvement in simulating the MJO, at least qualitatively (Kim et al. 2009; Chikira and Sugiyama 2013; Hirons et al. 2013). Similar to the observations, UNICON simulates maximum surface precipitation in the late afternoon (early afternoon in CAM5) over the continents during summer and in the early morning (predawn in CAM5) over the oceans, with a realistic amplitude of the diurnal cycle. The MJO simulated by UNICON was also realistic with less sensitivity to the simulation configuration and the perturbations of model parameters within a plausible range. This implies that UNICON correctly captures a certain set of key physical processes controlling the diurnal cycle of precipitation and the MJO in nature.

To understand the source of the biases in the simulated climatology and also to obtain insights into the characteristics of UNICON, a set of sensitivity simulations were performed. As convection becomes stronger (as diagnosed by the larger Λ), UNICON tends to increase LWCF/CLDHGH/IWP and WVP/RESTOA but decrease SWCF/CLDLOW/LWP and PRECT/PRECL/LHF, implying that strong convection moistens (dries) the upper (lower) troposphere, suppresses stratiform precipitation, and weakens the global hydrological cycle by stabilizing the atmosphere. This dependency on Λ is stronger in UNICON than in CAM5. It was also shown that the evaporation of convective precipitation within the environment and the cold pool has a large impact on the global radiation balance and the hydrological cycle and the wet removal of aerosols within convective updraft by convective precipitation substantially decreases the global AOD. Without the mesoscale perturbation of updraft plume radius, UNICON fails to reproduce the observed diurnal cycle of precipitation and the MJO. Without the mesoscale perturbations of the vertical velocity and thermodynamic scalars of convective updraft, however, UNICON still manages to simulate the MJO. This implies that any convection scheme aiming to simulate the MJO should be able to simulate the gradual changes of updraft plume dilution rate as convection evolves from shallow to deep convection and, additionally, mesoscale perturbations of the updraft vertical velocity and the thermodynamic scalars for the diurnal cycle of precipitation. The amplitude of the simulated diurnal cycle of precipitation increases as the mesoscale organized flow becomes strong.

The main goal of this work was to develop a research tool constructed on sound physical foundations that has the capability to reproduce various aspects of the observed climate as well as to serve as a tool to provide physical insights into convection observed in nature. UNICON, a state-of-the-art physically based convection scheme with minimum amount of empirical or ad hoc closures, is unprecedentedly successful in simulating the observed variability (e.g., diurnal cycle of precipitation and the MJO) as well as the observed climatology in the history of CAMs. The key physical processes responsible for this success could be identified through parameter sensitivity simulations. Not shown, UNICON also simulates better ENSO than CAM5 with a significant power peak of the Niño-3.4 SST anomalies at the observed period of 3–7 years, and with a more realistic amplitude (about half of the amplitude simulated by CAM5) and spatial composite patterns of SST and SLP, better tropical cyclone, and smaller spatiotemporal RMSE than CAM5 as the model horizontal grid becomes finer, indicating UNICON is more scale adaptive than CAM5. Results using coupled mode simulations with various resolutions will be reported in the future.

To be used as a successful parameterization for GCMs, additional research is necessary, both for improving UNICON itself and for imposing interprocess consistency between UNICON and the other components of GCMs. The author is continuously working on constraining various model parameter values using observations or LES, refining model physics, developing more sophisticated cloud microphysics interacting with aerosols, and improving computational efficiency (currently, CAM5 with UNICON takes about 50% more computation time than the default CAM5).

REFERENCES

Adler, R. F., and Coauthors, 2003: The Version-2 Global Precipitation Climatology Project (GPCP) monthly precipitation analysis (1979–present). *J. Hydrometeor.,* **4,** 1147–1167, doi:10.1175/1525-7541(2003)004<1147:TVGPCP>2.0.CO;2.

Arakawa, A., and W. H. Schubert, 1974: Interaction of a cumulus cloud ensemble with the large-scale environment, Part I. *J. Atmos. Sci.,* **31,** 674–701, doi:10.1175/1520-0469(1974)031<0674:IOACCE>2.0.CO;2.

Bentamy, A., P. Queffeulou, Y. Quilfen, and K. Katsaros, 1999: Ocean surface wind fields estimated from satellite active and passive microwave instruments. *IEEE Trans. Geosci. Remote Sens.,* **37,** 2469–2486, doi:10.1109/36.789643.

Bretherton, C. S., and S. Park, 2009: A new moist turbulence parameterization in the Community Atmosphere Model. *J. Climate,* **22,** 3422–3448, doi:10.1175/2008JCLI2556.1.

Chikira, M., and M. Sugiyama, 2013: Eastward-propagating intraseasonal oscillation represented by Chikira–Sugiyama cumulus parameterization. Part I: Comparison with observation and reanalysis. *J. Atmos. Sci.,* **70,** doi:10.1175/JAS-D-13-034.1.

Hahn, C. J., and S. G. Warren, 1999: Extended edited synoptic cloud reports from ships and land stations over the globe, 1952–1996. U.S. Department of Energy, Office of Biological and Environmental Research, Environmental Sciences Division Publ. 4913, ORNL/CDIAC-123, NDP-026C, 76 pp, doi:10.3334/CDIAC/cli.ndp026c.

Harrison, E., P. Minnis, B. Barkstrom, V. Ramanathan, R. Cess, and G. Gibson, 1990: Seasonal variation of cloud radiative forcing derived from the Earth Radiation Budget Experiment. *J. Geophys. Res.,* **95** (D11), 18 687–18 703, doi:10.1029/JD095iD11p18687.

Hirons, L., P. Inness, F. Vitart, and P. Bechtold, 2013: Understanding advances in the simulation of intraseasonal variability in the ECMWF model. Part II: The application of process-based diagnostics. *Quart. J. Roy. Meteor. Soc.,* **139,** 1427–1444, doi:10.1002/qj.2059.

Holland, J. Z., and E. M. Rasmusson, 1973: Measurements of the atmospheric mass, energy, and momentum budgets over a 500-kilometer square of tropical ocean. *Mon. Wea. Rev.,* **101,** 44–55, doi:10.1175/1520-0493(1973)101<0044:MOTAME>2.3.CO;2.

Huffman, G., and Coauthors, 2007: The TRMM Multisatellite Precipitation Analysis (TMPA): Quasi-global, multiyear, combined-sensor precipitation estimates at fine scales. *J. Hydrometeor.,* **8,** 38–55, doi:10.1175/JHM560.1.

Kain, J. S., and J. M. Fritsch, 1990: A one-dimensional entraining/detraining plume model and its application in convective parameterization. *J. Atmos. Sci.,* **47,** 2784–2802, doi:10.1175/1520-0469(1990)047<2784:AODEPM>2.0.CO;2.

Kalnay, E., and Coauthors, 1996: The NCEP/NCAR 40-Year Reanalysis Project. *Bull. Amer. Meteor. Soc.,* **77,** 437–471, doi:10.1175/1520-0477(1996)077<0437:TNYRP>2.0.CO;2.

Khairoutdinov, M. F., and D. A. Randall, 2003: Cloud resolving modeling of the ARM summer 1997 IOP: Model formulation, results, uncertainties, and sensitivities. *J. Atmos. Sci.,* **60,** 607–625, doi:10.1175/1520-0469(2003)060<0607:CRMOTA>2.0.CO;2.

Kim, D., and Coauthors, 2009: Application of MJO simulation diagnostics to climate models. *J. Climate,* **22,** 6413–6436, doi:10.1175/2009JCLI3063.1.

Kinne, S., and Coauthors, 2006: An AeroCom initial assessment—Optical properties in aerosol component modules of global models. *Atmos. Chem. Phys.,* **6,** 1815–1834, doi:10.5194/acp-6-1815-2006.

Liebmann, B., 1996: Description of a complete (interpolated) outgoing longwave radiation dataset. *Bull. Amer. Meteor. Soc.,* **77,** 1275–1277.

Loeb, N. G., B. A. Wielicki, D. R. Doelling, G. L. Smith, D. F. Keyes, S. Kato, N. Manalo-Smith, and T. Wong, 2009: Toward optimal closure of the earth's top-of-atmosphere radiation budget. *J. Climate,* **22,** 748–766, doi:10.1175/2008JCLI2637.1.

Madden, R. A., and P. R. Julian, 1971: Detection of a 40–50 day oscillation in the zonal wind in the tropical Pacific. *J. Atmos. Sci.,* **28,** 702–708, doi:10.1175/1520-0469(1971)028<0702:DOADOI>2.0.CO;2.

Neale, R. B., J. H. Richter, and M. Jochum, 2008: The impact of convection on ENSO: From a delayed oscillator to a series of events. *J. Climate,* **21,** 5904–5924, doi:10.1175/2008JCLI2244.1.

Neggers, R., H. Jonker, and A. Siebesma, 2003: Size statistics of cumulus cloud populations in large-eddy simulations. *J. Atmos. Sci.,* **60,** 1060–1074, doi:10.1175/1520-0469(2003)60<1060:SSOCCP>2.0.CO;2.

O'Dell, C. W., F. J. Wentz, and R. Bennartz, 2008: Cloud liquid water path from satellite-based passive microwave observations: A new climatology over the global oceans. *J. Climate,* **21,** 1721–1739, doi:10.1175/2007JCLI1958.1.

Onogi, K., and Coauthors, 2007: The JRA-25 Reanalysis. *J. Meteor. Soc. Japan,* **85,** 369–432.

Park, S., 2014: A unified convection scheme (UNICON). Part I: Formulation. *J. Atmos. Sci.,* **71,** 3902–3930, doi:10.1175/JAS-D-13-0233.1.

——, and C. B. Leovy, 2004: Marine low-cloud anomalies associated with ENSO. *J. Climate,* **17,** 3448–3469, doi:10.1175/1520-0442(2004)017<3448:MLAAWE>2.0.CO;2.

——, and C. S. Bretherton, 2009: The University of Washington shallow convection and moist turbulence schemes and their impact on climate simulations with the Community Atmosphere Model. *J. Climate,* **22,** 3449–3469, doi:10.1175/2008JCLI2557.1.

——, C. B. Leovy, and M. A. Rozendaal, 2004: A new heuristic Lagrangian marine boundary layer cloud model. *J. Atmos. Sci.,* **61,** 3002–3024, doi:10.1175/JAS-3344.1.

——, C. Deser, and M. A. Alexander, 2005: Estimation of the surface heat flux response to sea surface temperature anomalies over the global oceans. *J. Climate,* **18,** 4582–4599, doi:10.1175/JCLI3521.1.

——, M. A. Alexander, and C. Deser, 2006: The impact of cloud radiative feedback, remote ENSO forcing, and entrainment on the persistence of North Pacific sea surface temperature anomalies. *J. Climate,* **19,** 6243–6261, doi:10.1175/JCLI3957.1.

——, C. Bretherton, and P. Rasch, 2014: Integrating cloud processes in the Community Atmosphere Model, version 5. *J. Climate,* **27,** 6821–6856, doi:10.1175/JCLI-D-14-00087.1.

Plank, V. G., 1969: The size distribution of cumulus clouds in representative Florida populations. *J. Appl. Meteor.,* **8,** 46–67, doi:10.1175/1520-0450(1969)008<0046:TSDOCC>2.0.CO;2.

Prabha, T. V., A. Khain, R. Maheshkumar, G. Pandithurai, J. Kulkarni, M. Konwar, and B. Goswami, 2011: Microphysics of premonsoon and monsoon clouds as seen from in situ measurements during the Cloud Aerosol Interaction and Precipitation Enhancement Experiment (CAIPEEX). *J. Atmos. Sci.,* **68,** 1882–1901, doi:10.1175/2011JAS3707.1.

Randel, D. L., T. J. Greenwald, T. H. Vonder Haar, G. L. Stephens, M. A. Ringerud, and C. L. Combs, 1996: A new global water vapor dataset. *Bull. Amer. Meteor. Soc.,* **77,** 1233–1246, doi:10.1175/1520-0477(1996)077<1233:ANGWVD>2.0.CO;2.

Richter, J., and P. Rasch, 2008: Effects of convective momentum transport on the atmospheric circulation in the Community Atmosphere Model, version 3. *J. Climate,* **21,** 1487–1499, doi:10.1175/2007JCLI1789.1.

Rossow, W. B., and R. A. Schiffer, 1991: ISCCP cloud data products. *Bull. Amer. Meteor. Soc.,* **72,** 2–20, doi:10.1175/1520-0477(1991)072<0002:ICDP>2.0.CO;2.

Sandu, I., and B. Stevens, 2011: On the factors modulating the stratocumulus to cumulus transitions. *J. Atmos. Sci.,* **68,** 1865–1881, doi:10.1175/2011JAS3614.1.

Siebesma, A., and Coauthors, 2003: A large eddy simulation intercomparison study of shallow cumulus convection. *J. Atmos.*

Sci., **60,** 1201–1219, doi:10.1175/1520-0469(2003)60<1201: ALESIS>2.0.CO;2.

Simmons, A., S. Uppala, D. Dee, and S. Kobayashi, 2007: ERA-Interim: New ECMWF reanalysis products from 1989 onwards. *ECMWF Newsletter,* No. 110, ECMWF, Reading, United Kingdom, 25–35.

Stephens, G. L., and Coauthors, 2002: The CloudSat mission and the A-train: A new dimension of space-based observations of clouds and precipitation. *Bull. Amer. Meteor. Soc.,* **83,** 1771–1790, doi:10.1175/BAMS-83-12-1771.

——, and Coauthors, 2012: An update on Earth's energy balance in light of the latest global observations. *Nat. Geosci.,* **5,** 691–696, doi:10.1038/ngeo1580.

Stevens, B., and Coauthors, 2005: Evaluation of large-eddy simulations via observations of nocturnal marine stratocumulus. *Mon. Wea. Rev.,* **133,** 1443–1462, doi:10.1175/MWR2930.1.

Stokes, G. M., and S. E. Schwartz, 1994: The Atmospheric Radiation Measurement (ARM) Program: Programmatic background and design of the cloud and radiation test bed. *Bull. Amer. Meteor. Soc.,* **75,** 1201–1221, doi:10.1175/1520-0477(1994)075<1201:TARMPP>2.0.CO;2.

Taylor, K. E., 2001: Summarizing multiple aspects of model performance in a single diagram. *J. Geophys. Res.,* **106** (D7), 7183–7192, doi:10.1029/2000JD900719.

Tiedtke, M., 1989: A comprehensive mass flux scheme for cumulus parameterization in large-scale models. *Mon. Wea. Rev.,* **117,** 1779–1800, doi:10.1175/1520-0493(1989)117<1779: ACMFSF>2.0.CO;2.

Uppala, S. M., and Coauthors, 2005: The ERA-40 Re-Analysis. *Quart. J. Roy. Meteor. Soc.,* **131,** 2961–3012, doi:10.1256/qj.04.176.

Willmott, C. J., and K. Matsuura, 1995: Smart interpolation of annually averaged air temperature in the United States. *J. Appl. Meteor.,* **34,** 2577–2586, doi:10.1175/1520-0450(1995)034<2577:SIOAAA>2.0.CO;2.

Xiao, H., and Coauthors, 2014: Diagnosis of the marine low cloud simulation in the NCAR community earth system model (CESM) and the NCEP global forecast system (GFS)-modular ocean model v4 (MOM4) coupled model. *Climate Dyn.,* **43,** 737–752, doi:10.1007/s00382-014-2067-y.

Xie, P., and P. A. Arkin, 1996: Analyses of global monthly precipitation using gauge observations, satellite estimates, and numerical model predictions. *J. Climate,* **9,** 840–858, doi:10.1175/1520-0442(1996)009<0840:AOGMPU>2.0.CO;2.

Zhang, G., and N. McFarlane, 1995: Sensitivity of climate simulations to the parameterization of cumulus convection in the Canadian Climate Centre general circulation model. *Atmos.–Ocean,* **33,** 407–407, doi:10.1080/07055900.1995.9649539.

Zhang, M., J. Lin, R. Cederwall, J. Yio, and S. Xie, 2001: Objective analysis of ARM IOP data: Method and sensitivity. *Mon. Wea. Rev.,* **129,** 295–311, doi:10.1175/1520-0493(2001)129<0295: OAOAID>2.0.CO;2.